Impact of Climate Change on the Rossby Wave Activity over the Northern Hemisphere

Master's Thesis in
Meteorology and Climate Physics
by

Christian Daniel Schröder

May 2024

INSTITUTE OF METEOROLOGY AND CLIMATE RESEARCH
KARLSRUHE INSTITUTE OF TECHNOLOGY (KIT)

Supervisor:	Prof. Dr. Joaquim G. Pinto
Co-supervisor:	Prof. Dr. Andreas H. Fink

Abstract

In the mid-latitudes, extreme temperature events such as heatwaves, floods, and cold spells pose significant risks to human life, ecosystems, and the economy. These events are often driven by persistent atmospheric blockings, influenced by both the thermodynamical effects and changes in large-scale atmospheric dynamics, particularly Rossby waves, driven by global warming. This thesis investigates possible changes in Rossby wave activity and their implications for atmospheric blocking and temperature extremes over Europe.

This study uses high-resolution climate models and reanalysis data to analyze transient Rossby wave patterns through zonal wavenumber decomposition and high-pass filtering. Reanalysis data from 1940 to 2019 shows an increasing trend in Rossby wave activity, particularly in winter and spring, with a shift towards higher latitudes in spring. These trends are linked to an overall increase and, in spring, a northward shift in blocking events. The analysis of phase speeds yields mostly insignificant results with a slight tendency to increase speeds in winter and spring.

Model simulations with the AWI-CM model reproduce Rossby wave characteristics well. They show similar trends to the reanalysis data, with shifts of wave activity towards higher latitudes and smaller wavenumbers under the SSP370 and SSP585 scenarios. However, these scenarios also reveal a significant decrease in summer activity at the mid-latitudes—and for SSP370 as well for winter activity—different from the reanalysis data. While phase speed trends are only partly significant, they hint towards a general increase in phase velocity for the most active wavenumbers, strongest in winter and autumn. The trends in wave activity indicate a general shift in blocking frequency towards higher latitudes and an overall decrease in summer. In contrast, the trends in phase velocity indicate a general reduction in blocking frequency, but this is less clear for spring. Custom ICON timeslice experiments faced limitations in capturing real-world Rossby wave characteristics, though some tendencies observed with AWI-CM were reproduced.

Studies focusing on blocking events in reanalysis data, including some case studies on past heatwaves, show distinct signatures in the Rossby wave spectrum. These signatures are characterized by enhanced wave activity at the most dominant wavenumbers and reduced phase speed. This highlights the importance of Rossby waves in the context of blockings and extreme temperature events and supports our interpretation of the blocking frequency trends.

This research enhances our understanding of Rossby wave dynamics and their role in atmospheric blocking. These insights are valuable for improving climate projections and enabling actions to mitigate the effects of global warming. Future research should further investigate model discrepancies and focus on the signatures for different kinds and locations of blockings.

Keywords: Rossby waves, atmospheric blocking, global warming, zonal wavenumber decomposition, climate models, extreme weather events, heatwaves, cold spells, Europe.

Zusammenfassung

Extremwetterereignisse wie Hitzewellen, Überschwemmungen und Kälteeinbrüche stellen in den mittleren Breiten eine besondere Gefahr für Menschen, die Umwelt und die Wirtschaft dar. Diese Eregnisse werden häufig durch anhaltende blockierende Wetterlagen ausgelöst, die sowohl durch direkte thermodynamische Effekte als auch durch Veränderungen der atmosphärischne Dynamiken, insbesondere der Rossbywellen, durch die globale Erderwärmung beeinflusst werden. Diese Masterarbeit untersucht mögliche Änderungen in der Rossbywellenaktivität und deren Auswirkungen auf blockierende Wetterlagen sowie Extremtemperatureregnisse in Europa.

Mit Hilfe von hochaufgelösten Klimamodelle und Reanalysedaten werden in dieser Arbeit die Muster in transienten Rossbywellen mittels zonaler Wellenzahlzerlegung und Hochpassfilterung untersucht. Reanalysedaten von 1940 bis 2019 zeigen einen zunehmenden Trend in der Rossbywellenaktivität, besonders im Winter und Frühling, mit einer zusätzlichen Verschiebung zu höheren Breiten hin im Frühling. Diese Trends weisen auf eine Zunahme und, für den Frühling, nördliche Verlagerung von blockierenden Wetterlagen hin. Bei der Analyse der Phasengeschwindigkeiten ließen sich keine signifikanten Trends erkennen, allerdings war eine leichte Tendenz hin zu zunehmenden Geschwindigkeiten im Winter in Frühling erkennbar.

Modellläufe mit dem AWI-CM können die Charakteristika der Rossbywellen gut nachbilden und lassen unter dem SSP370- und SSP585-Szenario eine zukünftige Verlagerung der Rossbywellen hinzu höheren Breitengeraden und kleineren Wellenzahlen, mit einer Abnahme der Aktivität im Sommer (und für das SSP370-Szenario auch im Winter), erkennen. Auch wenn die Trends der Phasengeschwindigkeiten nur teilweise signifikant sind, zeigen sie insgesamt eine Zunahme, am stärksten für den Winter und Herbst, für die aktivsten Wellenzahlen an. Die Amplitudentrends deutet auf eine generelle Verschiebung zu höheren Breiten hin, mit einer Abnahme der Häufigkeit im Sommer, während die Phasentrends, abgesehen von dem Frühling, auf eine generelle Verringerung der Häufigkeit von blockierenden Wetterlagen hindeuten.
Die angepassten Timeslice-Experimente mit dem ICON-Modell konnten die wesentlichen Eigenschaften von echten Rossbywellen nicht zufriedenstellend simulieren, allerdings spiegelten einige Trends dennoch die Ergebnisse mit dem AWI-CM wieder.

Blockierende Wetterlagen in der Vergangenheit zeigen einige besondere Merkmale im Rossbywellenspektrum auf, insbesondere eine Amplitudenzunahme bei den aktivsten Wellenzahlen sowie eine Abnahme der Phasengeschwindigkeit. Dies betont die Bedeutung von Rossbywellen im Hinblick auf diese Ereignisse und stützt unsere Interpretation der oben genannten Trends.

Diese Forschungsarbeit verbessert unser Verständnis von Rossbywellendynamik und ihrer Rolle für blockierende Wetterlagen. Die Ergebnisse helfen es Klimaprojektionen zu verbessern und erlauben die Wahl von besseren Handlungsoptionen, um die Auswirkungen der globalen Erderwärmung abzumildern. Zukünftige Arbeiten sollten die Abweichungen von Klimamodellen und die spezi-

fischen Merkmale der verschiedenen Arten von blockierender Wetterlagen an unterschiedlichen Orten genauer untersuchen.

Schlüsselworte: Rossbywellen, blockierende Wetterlagen, globale Erderwärmung, zonale Wellenzahlzerlegung, Klimamodelle, Extremwetterereignisse, Hitzewellen, Kälteeinbrüche, Europa.

Contents

1 Introduction

Global warming imposes ever-growing risks and dangers to human life (Kovats and Kristie (2006), Forzieri et al. (2017)), the ecosystem (Walther et al., 2002) and the economy (Mohleji and Pielke, 2014). This is not only caused by the direct thermodynamic effect of global warming, i.e., increasing surface air temperatures, but global warming also impacts the large-scale dynamics of the atmosphere, with huge implications on the regional level (Shepherd, 2014). These changes in dynamics influence how frequent and how prolonged blockings, and, consequently, weather extremes occur, but also impact their preferred locations (Horton et al. (2015), Woollings et al. (2018)). Hence, understanding the changes in the atmosphere dynamics is one key ingredient for predicting the effects of climate change.

High-impact events like heatwaves are the natural hazards with the highest death tolls (Forzieri et al., 2017), while flooding and storms cause the greatest economic damage (Mohleji and Pielke, 2014). However, all these high-impact events are driven by the large-scale dynamics of the atmosphere. In most cases, they result from atmospheric blockings, which, as the name implies, block the mean flow and lead to persistent, large-scale deviations from the mean zonal flow. (Woollings et al. (2018), Kautz et al. (2022))

Rossby waves are atmospheric waves that travel along the jet streams, which are upper-level high-speed wind bands, and cause them to meander. This also impacts the pattern of troughs and ridges along the jet stream and, therefore, the weather in the mid-latitudes. But these waves also strongly affect blocking, i.e., its onset and maintenance. Often, blockings are initiated by Rossby wave-breaking events, where the amplitude of a Rossby wave becomes so high, and the phase speed is so low that wave-breaking occurs, similar to ocean waves approaching a beach. Also, after the onset of atmospheric blockings, Rossby waves play a key role in sustaining them. Therefore, possible changes in Rossby wave patterns due to climate change are of major interest concerning blockings and extreme weather events. (Woollings et al. (2018), Kautz et al. (2022))

There is also a strong connection between the strength of the jet stream and Rossby wave activity. A weakening of the mid-latitude jet would also cause the jet stream to meander more. This would imply increased Rossby wave activity with more frequent high-amplitude wavy configurations. This could lead to more frequent atmospheric blocking patterns, increasing the likelihood of extreme weather events. It would also increase the probability of subsequent blocking events, which could intensify extreme events. A good example here is subsequent heatwaves, where the first blocking event can lead to a depletion in soil moisture that can strongly enhance the impact of the following heatwave. But in general (or for singular events), the intensity of the extreme events depends on the duration and persistence of the blocking, which is more related to the phase speed of the Rossby

waves and wave-breaking events that sustain long blockings. On the other hand, strengthening the jet stream would imply less waviness and could lessen the likelihood of blocking events. (Woollings et al., 2018)

A long-running debate exists about whether climate change is weakening or strengthening the jet streams, which has implications for Rossby waves and blockings. The problem is so complex because of many different and partly opposing mechanisms. Ultimately, the jet stream's strength depends on the meridional temperature gradient in the troposphere. For climate change, different effects impact this temperature gradient; the most important ones are Arctic Amplification, the warming of the tropical upper troposphere, and the cooling of the polar tropopause.

On the one hand, the Arctic amplification leads to highly over-proportional warming of the near-surface atmosphere in Arctic regions and, hence, to a reduction of the (near-surface) meridional temperature gradient, which is expected to result in a weaker jet stream that is stronger meandering, with an increase in blockings. On the other hand, the upper-level tropical warming leads to a decrease in the (upper-level) meridional temperature gradient. It is, therefore, expected to result in a stronger but weaker meandering jet stream, which, in turn, reduces the likelihood of blockings. This is the so-called tug-of-war between the Arctic Amplification and the upper-level tropical warming. (Butler et al. (2010), Barnes and Screen (2015), Shaw et al. (2016), Woollings et al. (2018))

To complicate things, the increase of upper-level and decrease of lower-level meridional temperature gradient may also increase the vertical shear of the jet stream, changing its internal structure with further implications (Lee et al., 2019).

However, most recent studies on reanalysis data favor tropical warming as the dominant process, which results in a stronger jet stream that is also more concentrated (Shaw and Miyawaki, 2024). Woollings et al. (2023) revising reanalysis data during the last 40 years also find evidence for an overall pole-ward shift of the jet stream, supporting tropical warming as the more relevant process. This would additionally imply a shift in the Rossby wave activity and blockings along with the jet stream position to higher latitudes.

This jet stream strengthening, which implies a reduction in blockings, is also supported by papers that specifically study the blocking frequency with climate models. For the models of the most recent generation (CMIP6), an overall decrease in the persistence of European blockings is found with some regional-specific differences (Dorrington et al., 2022). Other papers (Trevisiol et al., 2022) also see a general reduction of blocking events in winter. At the same time, for Europe, this might also be connected with a south-east shift of blockings towards central Europe, but for summer, a clear tendency could not be identified for Europe.

On the other hand, Riboldi et al. (2020) were explicitly looking for a signal of Arctic Amplification in the Rossby phase speed climatology but could not find this. However, they could confirm the link between extreme temperature events and low phase speeds. Fragkoulidis and Wirth (2020) also confirmed the relationship between above-normal Rossby wave activity and below-normal phase speeds with persistent temperature extremes using a slightly different metric of Rossby wave packets. This relationship was already found in Fragkoulidis et al. (2018), and this paper also

highlighted the importance of non-circumglobal Rossby waves and the case-to-case differences in linking Rossby waves to temperature extremes.

Due to the complex structure of the atmosphere dynamic and the many interactions of different effects on different scales, dividing and separating the problem into simpler, distinct subsystems that can be studied apart (or even purely theoretically) is often not feasible. Opposing effects in different subsystems, like the tug-of-war between the Arctic Amplification and the upper-level tropical warming, further complicate things.

Therefore, the way to study these complex effects is by using sophisticated climate models in the hope that they catch all relevant features, which have to be verified. However, climate models have to be limited in terms of computing resources, and this also implies limitations in horizontal and vertical (and temporal) resolution. This is why they have difficulties simulating eddies on different spatial scales and their interaction with each other, among different scales, and with convection and orography. But at the same time, these eddies and interactions are the foundation for effects and impacts on large-scale atmospheric dynamics. The models struggle especially with simulating the onset and persistence of blocking, which makes predictions and projections hard. Except for the resolution, other limitations in current climate models make the simulation of blockings difficult, e.g., biases in Sea Surface Temperature (SST), simplified orography, improvable physical parameterizations, and limited numerical accuracy in the dynamical core. (Woollings et al., 2018)

Even though climate models have improved a lot and evolved, in the most recent model intercomparison (CMIP6), they still struggle with simulating blockings. There is often a negative bias in simulated blocking frequency, especially over Europe and most strongly in winter, i.e., they systematically underestimate blocking frequencies. In general, these models tend to predict a reduction in blocking frequency over Europe (winter and summer) with climate change, except for an increase over the Ural mountains in summer, but there are still large model-to-model variations. (Davini and D'Andrea (2020), Woollings et al. (2018))

Because of the strong connection between Rossby wave activity and blockings, it can be a good approach to study Rossby wave activity and its possible changes separately to overcome some of the limitations of current climate models concerning blockings. Using specifically the method of zonal wavenumber decomposition, which transfers the complicated spatial structures of Rossby waves into basically (time and latitude dependent) amplitudes and phase speeds, makes this problem more approachable. These more general features of the large-scale atmospheric flows are also expected to be more robust and, hence, more accessible via current climate models. So far, there are only a couple of studies done with this focus, but most of them only look at circumglobal Rossby waves and wavenumbers (e.g., Kornhuber et al. (2020)) or use slightly different and more complicated metrics.

This thesis tries to fill the gap and investigates possible changes in large-scale dynamics at the jet stream level. It focuses on Rossby wave activity and its potential impacts on blockings and temperature extremes over Europe. In pursuit of these objectives, the research seeks answers to the following questions:

1. What are the characteristics in the Rossby wave spectrum that are important for the climate in Europe, and what are their trends in reanalysis data?

2. To what extent do current climate models capture essential Rossby wave characteristics, and what are their projected trends?

3. How do atmospheric blockings influence temperature extremes, and what is their relationship with Rossby wave activity?

By addressing these objectives, this thesis seeks to contribute to the broader understanding of large-scale atmospheric dynamics, possible changes in a warming climate, and their impacts on weather and climate extremes in Europe.

The thesis is structured as follows:

Chapter 2 provides a brief overview of the different effects and drivers that impact atmospheric dynamics on a large scale. This chapter aims to supply the necessary background information to fully understand the research questions and discussions in the subsequent chapters.

Chapter 3 introduces the data and variables used in this thesis. It also explains the various techniques employed for data analysis.

Chapter 4 will address the first research question. To answer this question, it first investigates suitable methodologies for dissecting Rossby wave activity, namely zonal wavenumber decomposition and high-pass filtering methods. It examines the application of these methods to specific sectors of the hemisphere and compares them to circumglobal wave activity. Last but not least, it will study the most relevant characteristics in the wave spectra and their trends based on reanalysis data to conclude their implications for blockings over Europe.

Chapter 5 focuses on the 2nd research question. It assesses the fidelity of climate models in simulating Rossby wave characteristics and compares this to ECMWF Reanalysis v5 (ERA5) reanalysis data. It then investigates the trends of Rossby wave activity under various global warming scenarios to discuss potential future trends for blockings over Europe.

Chapter 6 discusses the 3rd research question. We study the relationship between atmospheric blockings, extreme temperature events, and the Rossby wave activity spectrum to answer this. Through three case studies of recent heatwaves, we aim to unravel the mechanisms linking these phenomena and their implications for Europe's climate dynamics.

Finally, Chapter 7 provides a summarizing conclusion, contextualizing the results within the broader scope of the research. Chapter 8 collects supporting material, including additional plots and graphs.

2 Background Information

Even though there are some important effects and interactions regarding the stratosphere, the most relevant part of the atmosphere concerning extreme weather events and large-scale dynamics is the lowest layer of Earth's atmosphere, the troposphere. Therefore, in the following, we want to focus primarily on the troposphere, which features a complex circulation system responsible for transporting heat, moisture, and momentum across the globe. I will introduce the concepts here only very briefly. Still, most of them can be studied in extensive detail in one of the famous books about dynamical meteorology, e.g., Holton and Hakim (2013) or Vallis (2017); for the more specific topics, i.e., the sections about blockings, I will provide the references.

2.1 The three-cell model of the troposphere

The radiation from the sun is the driver of the troposphere's circulation system. Due to the increasing inclination towards the equator, there is an average energy surplus at low latitudes, i.e., incoming shortwave radiation from the sun. However, due to its temperature, the Earth emits radiation into space (Stefan Boltzmann's law). This outgoing longwave radiation becomes dominant at higher latitudes due to the decreasing inclination of the sun and causes an energy deficit in the polar regions. This energy surplus in the tropics and the energy deficit at higher latitudes is the fundamental driver for the large-scale circulation system in the troposphere. Earth's spin around its axis introduces a fictitious force, the Coriolis force, which diverts the winds of the circulation on its way to the poles and causes the circulation system to break up into three separate cells: the Hadley cell, the Ferrel cell, and the Polar cell.

Figure 2.1: Schematic illustration of the three-cell model of the Earth's atmosphere. The vertical extent of the troposphere is not to scale. The red arrows indicate the surface winds, while the blue arrows show the circulation in the upper troposphere. (Figure taken from NOAA (2023))

2.1.1 Hadley cell

The Hadley cell is the primary circulation cell that extends from the equator to about 30° both sides of the equator. It is directly driven by solar heating in the Inter-Tropical Convergence Zone (ITCZ), which leads to large and high-reaching convective cells all year round. The air then travels at upper levels towards the poles, and on its way, it cools, loses moisture via precipitation, and also gets diverted towards the east by the Coriolis force. Around 30° latitude, it descends and warms due to adiabatic compression. The descending air leads to high-pressure zones with warm and dry air, causing desert regions. The compensating surface currents towards the ITCZ lead to important features like the trade winds and play a role in the somewhat more complicated monsoonal winds, which are beyond the scope of this thesis.

The Hadley cell features a clear seasonal signature. The ITCZ and the upwelling part of the Hadley cell shift towards the summer hemisphere, while the branch of the summer hemisphere narrows and weakens. At the same time, the other branch of the cell gets wider and stronger so that it extends far into the winter hemisphere and becomes the much stronger part of the circulation.

2.1.2 Ferrel cell

The Ferrel cell is a so-called thermally indirect driven cell because it is driven by the down-welling branch of the Hadley cell on the equator-ward side and the weak up-welling branch of the Polar cell on its pole-ward side. This is also why it is circulating in the opposite direction compared to the other two cells, i.e., the surface air flow is mainly poleward and east. This cell is located between the Hadley and polar cells and extends from about 30° to 60° latitude (with seasonal variations). The Ferrel cell acts as a transitional area where warm and moist air from the tropics meets cold and dry air from the polar region, which leads to distinct weather features with high and low-pressure systems and extratropical cyclones, especially at the pole-ward flank of this cell.

2.1.3 Polar cell

The polar cell is located between about 60° latitude and the pole in both hemispheres. It is much weaker than the other cells and is weakly driven by the cooling due to the energy deficiency at the poles and the resulting temperature gradient. This causes high-pressure zones near the poles and (north/south) easterly surface winds in the (northern/southern) hemisphere, where the subsiding air masses over the poles flow back to higher latitudes.

2.1.4 Connection to the jet stream

The two boundaries between these three cells are where the jet streams are located. The subtropical jet stream is located around 30° latitude at the border of the Hadley cell at around 200 hPa while the mid-latitude jet (also known as the eddy-driven jet or polar jet) is located between the Ferrel

and polar cell at about 40–60° latitude. The mechanisms and details of these two jet streams will be discussed in further detail later in this chapter.

2.2 Jet stream

Jet streams are persistent, fast-flowing air currents in the troposphere, with their core at the top of the troposphere encircling the whole globe.[1] These strong westerly winds significantly impact the climate and weather patterns, particularly in the mid-latitudes. The jet streams are categorized into two types: the subtropical jet stream confined to high altitudes at the edge of the tropical Hadley cell and the eddy-driven jet streams, which reach down to the surface and can be observed in a broader range of latitudes. Still, its core with maximum wind speeds is usually located between the Ferrel and polar cell. They are not always well separated everywhere, as seen in Figure 2.2 for two different longitudes. The two kinds of jet streams will be explained in the following.

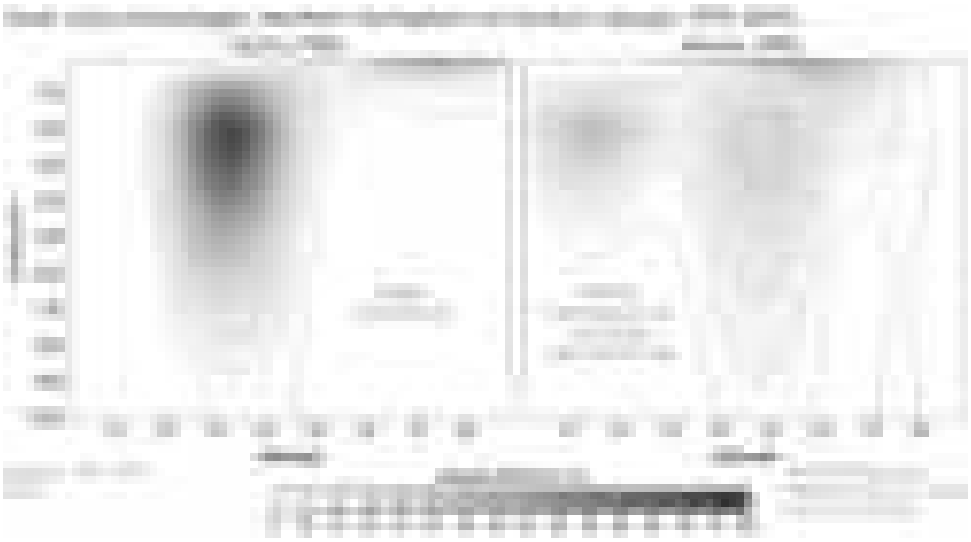

Figure 2.2: The jet streams or average zonal wind (in meters per second) over a cross-section of the Pacific Ocean (left panel) and Atlantic Ocean (right panel). The x-axis shows the latitude in the Northern Hemisphere, with the equator on the left and the North Pole on the right. The y-axis is the pressure level oriented, with the surface on the bottom and the top indicating the top of the atmosphere. Data is based on ERA5 using a 1979-2019 climatology. Image courtesy of Tim Woollings and modified by Climate.gov. (Figure and caption taken from Woollings (2022))

2.2.1 Subtropical jet stream

The subtropical jet stream is typically found around 30° latitude at the edge of the Hadley cell and at an altitude of about 200 hPa. It exhibits a strong meridional temperature gradient with mostly baroclinic characteristics and is mostly confined to the very upper levels of the atmosphere with a strong vertical shear. The driver of the subtropical jet stream is angular momentum conservation,

[1] We will exclude here the Tropical Easterly Jet, despite its name, because it only extends from Southeast Asia to West Africa and therefore is not a circumglobal feature. Besides, it only exists during the phase of the South Asian and African summer monsoon, i.e. boreal summer and early autumn, and is not a permanent feature. Low-level Jet streams, as non-permanent regional features, will also not be considered a jet streams in this context.

i.e., angular momentum gets exported from the ITCZ and fed into the subtropical jet via the upper branch of the Hadley cell. Its seasonality is linked to the seasonal shifts of the Hadley cell, i.e., a stronger and more persistent jet stream in winter at slightly lower latitudes, while in summer, it's slightly shifted to higher latitudes and weaker.

2.2.2 Eddy-driven jet (also sub-polar or mid-latitude jet)

The eddy-driven jet stream, sometimes called sub-polar or mid-latitude jet, is usually positioned between 40° and 50° latitude, displays more barotropic features, and has much less vertical shear, i.e. it extends down close to the surface even though it has its maximum at around 300 hPa due to thermal wind relations. This jet experiences less shear compared to its subtropical counterpart, where the friction gets compensated by momentum convergence. This is mainly driven by transient eddies, and therefore, the mid-latitude jet is also called an eddy-driven jet. While the eddies are caused by baroclinic instability, the flow itself results from barotropic mechanisms. The eddy-driven jet is far less stable and continuous than its subtropical counterpart; it often merges with the subtropical jet, and this real-world appearance will be discussed in the next section.

The detailed explanation for the mid-latitude jet and how this flow is sustained is far more complicated than for the subtropical jet. Hence, there are different perspectives on this mechanism with a complicated mathematical framework, e.g., vorticity budget, Rossby waves and momentum flux, and Eliassen-Palm flux, which can be studied in depth in books about theoretical meteorology (e.g. Vallis, 2017). Here, I will only briefly introduce the momentum flux perspective in a few sentences: Any small disturbances can initiate Rossby waves in the atmospheric flow. These waves then propagate away from the source region and dissipate elsewhere, i.e. they export energy. This has to be compensated by momentum flux conversion, i.e., momentum flux towards the region of disturbance, which leads to an eastward flow in the source region and a westward flow north and south of this region. This is also represented by north-east tilted ridges and south-west tilted troughs, i.e. bow-shaped eddies that feed momentum into the easterly jet stream.

2.2.3 Real world jet stream

In the real world, the subtropical and the mid-latitude jet streams are often not well (or not at all) separated, and there are also significant seasonal and regional differences. The orography significantly impacts the jet streams over the continents (North America and Asia). It increases the friction and slows down the low- to mid-level winds, but also directly and indirectly[2] deflects the air stream. This can be seen clearly downstream of large mountain ranges (Rocky Mountains, Himalayan Mountains), where the two jet streams often merge into one and where there is relatively slight day-to-day variation. To complicate things, the jet stream at the Himalayan is also strongly impacted by the yearly monsoon, which deflects it to the north of the Himalayan mountains during the summer monsoon season. This is due to the strong anti-cyclonic air outflow at the top of the atmosphere above the thermal low at the ground.

[2] The orography changes the atmosphere's height, leading to deflections due to the conservation of potential vorticity.

At the east coasts of the continents, the stark land-sea temperature contrasts[3] introduce a lot of baroclinic instability that fuels the eddies along the storm-tracks and is feeding energy into the jet stream. The highly reduced friction at the surface over the oceans and the absence of orographic obstacles eventually allow the eddy-driven jet stream to separate from the subtropical jet stream over the Atlantic. In the case of the Pacific Ocean, this often happens only over the eastern part of the ocean. The eddy-driven jet is often not well separated from the subtropical jet stream. Usually, two distinct jets are, if at all, only visible over the eastern parts of the oceans and the western parts of the continents adjacent to the oceans.

There are also large seasonal effects. In summer, the meridional temperature gradient is much weaker, which leads to a much weaker jet. Then, the subtropical jet stream is located at higher latitudes because the ITCZ is shifted to the north, and the polar flank of the (northern) Hadley cell moves also, but to a lesser extent, north. This leads to a much less pronounced and less distinct mid-latitude jet stream, which is also more meandering. Also, the heating of the continents leads to stationary thermal lows that further deflect the jet stream.

In the winter, on the other hand, the jet streams in the northern hemisphere are much stronger and less wavy. Then, the subtropical jet is also located at lower latitudes, which helps the mid-latitude jet to separate at some locations (over the Atlantic Ocean and the eastern part of the Pacific Ocean).

2.3 Rossby Waves

While Rossby waves can exist in any rotating fluid system, e.g., Earth's oceans or atmosphere, in this thesis, we will use the term specifically for atmospheric Rossby waves because our research interest is the dynamics of the atmosphere with a focus on the troposphere. (Atmospheric) Rossby waves are also known as planetary waves, and they significantly impact the weather at mid-latitudes. But in general, Rossby waves and their propagation do not have to extend around the whole globe. That is also why it is sometimes distinguished between Rossby waves and Rossby wave packets (or Rossby wave trains), where the latter are wave trains with a spatially limited extent. In this thesis, I will use the term Rossby wave regardless of the spatial extent, and most often, it will denominate spatially limited wave packets. When the spatial extent plays a role, I will make it explicit by using the corresponding adjective, e.g., "circumglobal."

The root cause for these large-scale waves is the Earth's rotation, the resulting Coriolis effect, and the conservation of angular momentum (specifically, the conservation of potential vorticity). Rossby waves propagate westward[4] relative to the flow in which they are embedded. Hence, due to the strong westerly jet stream, their propagation relative to the surface can be eastward or westward. In the mid-latitudes, Rossby waves usually move to the east with respect to the ground, with waves with larger wavelengths typically moving slower and sometimes becoming stationary or even moving westward.

[3] In winter this is further enhanced by the warm Kuroshio and Gulf current along the eastern shore of Asia and North America, respectively

[4] This is due to the Earth's rotation from west to east and the sign of the Coriolis force.

In reality, this picture is a bit more complicated because there can also be propagation to some extent in the vertical, i.e., into (and from) the stratosphere. This causes some interesting effects, especially in the winter, e.g. so-called sudden stratospheric warming events, but it is far beyond the scope of this thesis. Also, their direction of propagation can have a meridional component. However, it is important to know that the jet stream acts as a waveguide for Rossby waves, which will be explained below. That means that Rossby waves, even if they initially propagate to some extent in the meridional direction, they usually get trapped in the jet stream as soon as they hit it. From that moment on, they propagate along the jet stream, usually visible as a meandering jet stream. Rossby waves can be initiated, e.g., by heavy tropical convection, where the resulting Rossby waves travel in a poleward direction until they hit the jet stream. Then, they usually travel alongside the jet stream. In this thesis, I'm mainly interested in the effect of Rossby waves in conjuncture with the meandering of the jet stream, and this is caused by Rossby waves that are trapped by the jet stream and propagate zonally (neglecting the smaller meridional deflections of the jet stream itself). Therefore, our focus here will be on Rossby waves in a zonal direction.

2.3.1 Mathematical Formulation

The key component of understanding Rossby waves is (potential) vorticity conservation[5] in a rotating fluid system. Absolute potential vorticity combines the effects of Earth's rotation (planetary vorticity) and the rotation of air parcels (relative vorticity) in a stratified fluid. When an air parcel in the Northern Hemisphere is deflected to the North (South), the planetary vorticity increases (decreases), and due to the conservation law of absolute potential vorticity, the relative vorticity must change accordingly, i.e., it decreases (increases), which implies a clockwise (counterclockwise) turning of the air. This acts as a restoring force on the initial deflection and enables the propagation of atmospheric waves in the zonal direction (with amplitudes in the meridional direction).

The mathematical formulation of Rossby waves is very complicated, so one usually uses the quasi-geostrophic approximation, which simplifies the full Navier-Stokes equations under the assumption of a nearly horizontal flow in a rotating system with stable stratification. Under these simplifications, one can derive a solution for Rossby waves by using the vorticity equation, which in its simplest form is:

$$\frac{d\zeta}{dt} + v\beta = 0$$

where ζ is the relative vorticity, v is the meridional (north-south) component of the velocity, and β is the Rossby parameter (defined as the variation of the Coriolis parameter with latitude, $\beta = \frac{\partial f}{\partial y}$).

This leads to sinusoidal wave solutions for v of the form $v = v_0 e^{i(kx+ly-\omega t)}$ where k and l are the zonal and meridional wave numbers, respectively, and ω is the frequency.

[5] To simplify things and keep it illustrative, we will not dive into the details of 3-D vorticity conservation, which is linked to potential vorticity, but will use here a simplified 2-D model.

From this, the dispersion relation for Rossby waves can be directly derived as:

$$\omega = \overline{u}k - \frac{\beta k}{k^2 + l^2}$$

assuming a steady background flow $\overline{u}$ in zonal direction. This can then be re-written into an equation which describes how the phase speed of the waves depends on their wavelength:

$$c = \overline{u} - \frac{\beta}{k^2 + l^2}$$

where c is the phase speed of the wave relative to the mean flow and $\overline{u}$ is the mean zonal (west-to-east) wind speed.

The negative sign indicates that Rossby waves generally move westward relative to the mean flow or in the absence of a mean zonal wind ($\overline{u} = 0$). From this relation, we see that the phase speed of Rossby waves depends inversely on the wave number, indicating that shorter waves propagate more slowly westward with respect to the mean flow. But since the mean flow is moving eastward, i.e., in the opposite direction, short waves usually propagate quicker with the mean flow towards the east with respect to the surface. At longer wavelengths (or smaller wavenumbers) the relative propagation with respect to the mean flow can become so fast, that the waves can be stationary or even move westward with respect to the ground.

2.3.2 Modifications and real-world implications

One should also mention that, in reality, we don't have a constant zonal flow $\overline{u}$ without a meridional gradient, but we observe somewhat concentrated jet streams with a strong core. This leads to a gradient in the background flow, and the Rossby parameter β from above has to be modified to $\beta^* = \beta - \partial^2\overline{u}/\partial y^2$. In the case of a westerly jet, this meridional curvature of the zonal wind profile leads to a bending of the propagation path towards the core of the jet stream. This is exactly the mechanism behind it when we talked about the phenomenon that Rossby waves get trapped in the jet stream.

Due to brevity, we were only showing a simplified vorticity equation for 2 dimensions, which is usually enough to understand the basic principles and cover a lot of real-world effects because the vertical extent of the atmosphere is often negligible compared to the horizontal, and the troposphere at large scales can often be considered stratified. One important exception in the real world where we need to extend our view to the vertical, and hence look into the 3-D version of the vorticity equation, is the orography. Higher mountain ranges block part of the atmosphere and lead to an effective reduction of the vertical extent of the troposphere. This results in a decrease in the vorticity at the upstream side of the mountain range and an increase in vorticity at the downstream side. Hence, upstream (downstream) of a mountain range, assuming a westerly flow, it has an additional cyclonic (anti-cyclonic) component, and we can observe a deflection of the flow, i.e., northward

directly above the mountain range and southward downstream of it. This southward deflection is then the origin of stationary Rossby waves that propagate east. This can be observed, e.g., at the Rocky Mountains, and has a large impact on the jet stream.

This all was just a brief and simplified introduction to the basic concepts of the very complicated topic of Rossby waves that can be studied more in-depth by looking at one of the famous books about theoretical/dynamical meteorology, e.g. Vallis (2017), Holton and Hakim (2013) or Etling (2008).

2.4 Mid-latitude atmospheric circulation

The mid-latitude atmospheric circulation takes place only in a subsection of the three-cell model, i.e. mostly the Ferrel cell. However, it has to be noted that the three-cell model is just a simplified conceptual model that covers only the zonal average of the flow without paying too much attention to turbulence, orography, land-sea contrast, etc. Hence, this model doesn't represent the variability of the real-world mid-latitude atmospheric circulation, which is characterized by very complex dynamics. One reason for this is that in the mid-latitudes, the circulation is dominated by eddies, which are the primary mode of atmospheric motion. These eddies manifest at different spatial and time scales, making the flow intrinsically turbulent. This makes understanding mid-latitude weather patterns very difficult.

In this picture, Rossby waves act primarily as weak perturbations within this unstable flow. However, their influence is significant due to the flow's unstable nature, particularly in the interaction with the mean zonal (west-to-east) flow, so they can cause large deviations and meandering of the flow. This interaction is a prime example of non-linear dynamics within the atmosphere, and the modulation of the mean flow by Rossby waves can yield significant climatic effects.

The zonal asymmetry in the mid-latitudes is another crucial aspect. This asymmetry results from various factors, including differences in boundary conditions such as orography (e.g. mountain ranges), land-sea contrasts, and regional variations in heating and cooling, including those influenced by the diurnal cycle. These zonal asymmetries cause hydrodynamic instabilities due to the significant shear between the boundary layer and the free atmosphere. The resulting baroclinic instability is an important driver for the development of asymmetric perturbations in the zonal flow. Basically, the unstable flow causes baroclinic instability, which is the foundation for the growth of eddies and the subsequent development of geostrophic turbulence.

Despite the inherently turbulent nature of the mid-latitude atmosphere, Rossby waves have a significant impact on modulating this flow. They represent the most important non-linear interaction within the mid-latitude climatic system. The interaction between Rossby waves and the zonal mean flow is very complex but, at the same time, crucial for understanding the development of weather patterns and the impact of climate change on the patterns in these regions.

In summary, the atmospheric circulation at mid-latitudes is a dynamic and complex system influenced by eddies, Rossby waves, and zonal asymmetries driven by various boundary conditions.

2.5 Blockings and Rossby waves

There are many different definitions of blockings and what is considered a block. However, the key properties of blockings are that they disrupt the zonally westerly flow in the mid-latitudes, i.e., there is a significant deviation from the zonal mean with a dominant meridional component, often leading to a flow inversion at some point. Mostly, there are three different categories of blocks (or precursors) considered, but their exact definitions can slightly differ between different authors: amplified ridges (also: subtropical ridges)[6], Omega block, and Rex block (also called dipole block). These three categories can also be seen as evolutionary states of blocks, i.e. blocks usually start as an amplified ridge and then–under certain circumstances–can further evolve into an Omega block, which is basically the consequence of a very strong amplification of a ridge (Sousa et al., 2021). If then there also happens to be a Rossby wave-breaking event, the Omega block can further evolve into a Rex block, which is the consequence of a tilting of an Omega block and can happen in a cyclonic or anti-cyclonic way depending on the kind of wave-breaking.

There is a strong connection between Rossby wave breaking and blockings because Rossby waves lead to an amplification of ridges and to a meridional displacement of geopotential contour lines. As known from other waves, like ocean waves, Rossby waves can also break when their amplitude gets amplified while their phase speed becomes low. Such a Rossby wave breaking leads to a strong cyclonic or anti-cyclonic tilt in the geopotential height field and significantly modifies it. Also, Rossby waves have a strong impact on the persistence and stationarity of the blocks themselves because stationary or quasi-stationary Rossby waves can lock the blocking in space and can also "feed" the block and help it sustain itself for a long time.

The following will briefly describe the three categories or stages of blocking development and will mostly follow the nomenclature and definitions in Sousa et al. (2021).

2.5.1 Subtropical ridges (or amplified ridges)

One should note, that a subtropical ridge is most often not considered a blocking, but it is mentioned here as an evolutionary step because it is often a precursor state of a blocking. When becoming stationary, they can still have similar impacts to those of the Omega block. A distinct feature of subtropical ridges that sets them apart from "real" blockings is that there are no closed contour lines in the geopotential height field. However, there is still a significant meridional component in the geopotential field, as shown in Figure 2.3 b). That causes a flow deviation from the mean zonal to a meridional direction along the ridge, which already impacts the weather on larger scales. The amplified ridges mainly occur at lower latitudes (hence the name "subtropical ridge") and mostly

[6] Strictly speaking, ridges are not considered a block, but they usually appear in the context of blocks and are also a precursor state for then developing blockings.

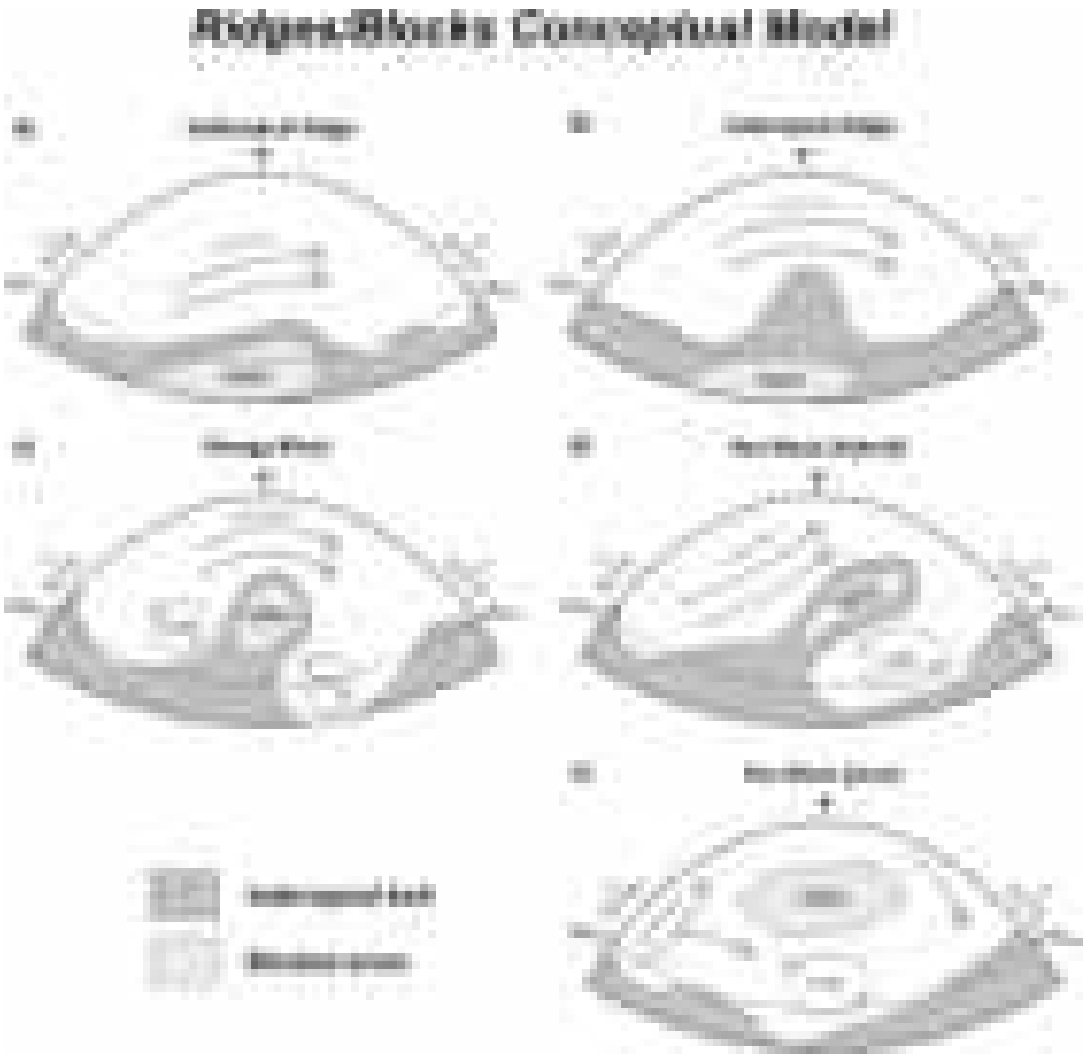

Figure 2.3: Conceptual model of high-pressure patterns describing a typical life cycle of an event in the NH, including the initial stages as a subtropical ridge, the development of flow reversals with omega shapes after a wave breaking, and mature phases as an isolated split-flow Rex block. Pink shading corresponds to air masses with subtropical characteristics, while green areas represent the blocking of the extratropical westerlies by flow reversals in the middle troposphere. ... Gray and blue arrows denote typical synoptic features. (Figure and caption taken from Sousa et al. (2021))

during summer. Therefore these ridges have most of an impact at lower latitudes. Under matching conditions, these ridges can further amplify and evolve into Omega blocks.

2.5.2 Omega Block

Omega blocks are characterized by an anticyclone accompanied by a cyclone on either side, i.e., one upstream and one downstream, as shown in Figure 2.3 c). An often imposed requirement to be considered an Omega block is enclosed geopotential height lines in the ridge area, which sets it apart from the subtropical ridge. Thereby, the flow is diverted in an Omega-like shape from where the name originates, and at least at one side of the blocking, we can find an inversion in the direction of the mean flow at some scale, i.e., in some regions, the flow is westward, which is

another difference to the subtropical ridge. The Omega block can develop further and transition into a Rex block. Omega blocks are usually only slightly tilted, which sets them apart from the so-called hybrid (Rex) block that will be described next.

2.5.3 Rex Block (or dipole Block)

The development from an Omega block to a Rex block that has a significant flow reversal to one side of the blocking is usually initiated by a Rossby wave breaking (depicted in Figure 2.3 d)). This leads to a very strongly tilted ridge with an anticyclone embedded. This state, also called hybrid Rex block, marks the transition from an Omega block to a pure Rex block. For the Rossby wave breaking, cyclonic and anticyclonic wave breaking events are distinguished, which usually determine the direction of the tilt of the ridge. This is not so important for the final Rex block and is rather of interest when looking at where and how frequently the wave breaking evolves because there are some differences depending on which side of the jet stream the breaking occurs.

A (pure) Rex block can be considered as the final state and consists of an anticyclone north of a cyclone which can be seen in Figure 2.3 e). The distinct feature of a (pure) Rex block is that it forces the jet stream to split upstream of the blocking into two separate flows, one flowing north and the other south of the anticyclone.

A block's dissolution usually occurs in the same stages but in opposite directions. For example, the anticyclone of a Rex block may merge with the subtropical belt and then disappear into an amplified ridge.

2.6 Blockings and temperature extremes

There is also a strong relationship between blockings and temperature extremes because the blockings induce a strong meridional flow that can advect warm or cold air masses. Blockings also go together with high and low-pressure systems, which impact the radiation budget and the soil moisture via latent heat fluxes. Further, there is also a huge impact on the precipitation, but this is out of the scope of this thesis. The soil moisture will be only considered here to some extent because it significantly impacts the surface temperatures via latent heat fluxes. Dry soils don't allow for large latent heat fluxes, so there's a shift towards higher sensible heat fluxes to compensate for the reduced latent heat flux. Differently from latent heat, sensible heat fluxes have a direct warming effect on the air above, which leads to increased warming of air close to the surface and also results in dryer air with less precipitation. (Kautz et al., 2022)

This is best understood when looking at two descriptive examples, i.e., an Omega block over Europe, once in winter and once in the summer, according to Kautz et al. (2022).

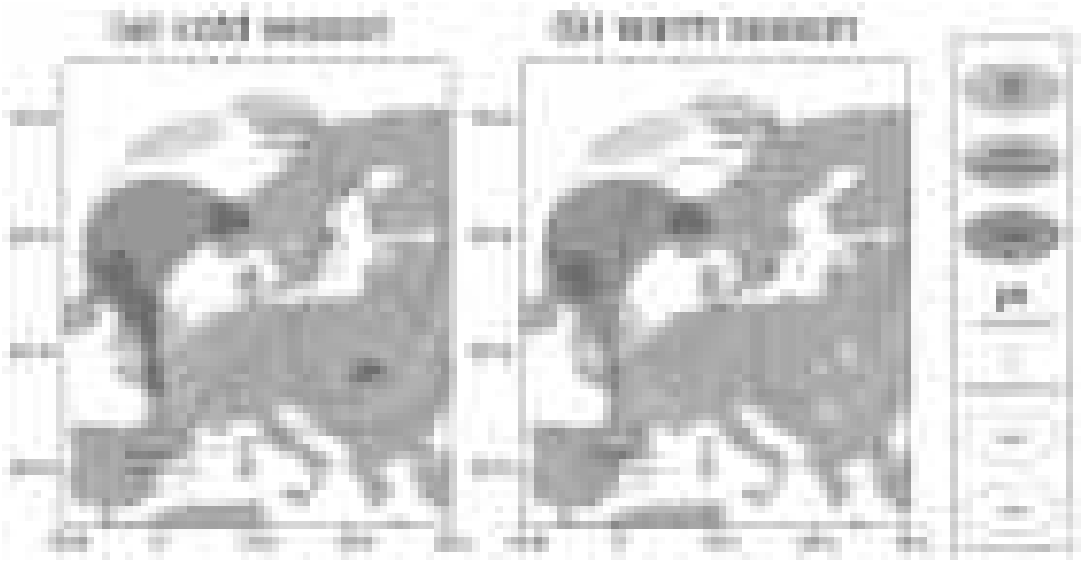

Figure 2.4: Schematic illustration of a blocking system (black line, indicating a geopotential height or PV contour) and some associated surface extremes during (a) the cold season (October–March) and (b) the warm season (April–September). Rossby wave breaking occurs on the flanks of the block, leading to (persistent) cutoff systems in this area. Blue stars show areas where snowstorms are observed (eastern flank of the block). Areas with heavy precipitation are marked in light blue (poleward edge of the ridge and at both flanks). Areas with high integrated water vapor transport (IVT) are illustrated in orange. Thunderstorm activity is marked by yellow lightning bolt symbols. The position of a warm conveyor belt appears in purple. Areas with temperature extremes are marked with dashed lines (red for heat waves and blue for cold spells) (Figure and caption taken from Kautz et al. (2022))

2.6.1 Omega block in summer

Blockings have several impacts on heat extremes in summer. In summer, the temperature advection by the meridional deformed wind field plays a minor role. Much more important is the deformation in the geopotential height field, i.e. the blocking comes together with a high-pressure system (and ridge) as shown in Figure 2.4 (b). This causes air mass subsidence and heating via adiabatic compression, increasing temperature. Besides, with its connected subsidence, the high-pressure system dissolves clouds and prevents convection and condensation. These clear sky conditions lead to strong radiative heating, which, in summer, surpasses the radiative cooling during the night. Adiabatic and radiative heating are the most relevant direct processes in the summertime that may eventually lead to extremely hot temperatures and heatwaves.

Apart from those two effects, there is also the very important effect of the drying of the soil, which strongly depends on the soil conditions at the time of arrival or emergence of the blocking. The drying soil leads to a shift of the surface heat fluxes from latent heat more and more to sensible heat fluxes. This makes radiative heating even more effective because, for very dry soil, nearly all of the energy of the absorbed incoming sunlight is converted into heat, which is then exchanged with the air mass above the surface. This can strongly increase the surface air temperature, especially in combination with the clear sky conditions that prevent precipitation and are caused by the blocking itself. This effect also makes the connection between blockings and droughts obvious.

The strong increase in warming close to the surface due to the drying soil also explains why the maximum temperatures vary greatly from one blocking to another. The atmospheric blocking alone is insufficient to explain the temperatures reached. Instead, the maximum temperatures during a blocking depend a lot on the soil moisture conditions and how they evolve during the blocking. That is also why sometimes several consecutive and intermittent, but individually relatively short-lasting blockings can result in higher temperature maxima (due to the eventual drying of the soil) than a single, long-lasting blocking.

There are also some other impacts of the blocking on strong precipitation and thunderstorms, which can result in floods–but all that is out of the scope of this thesis and will not be discussed further.

2.6.2 Omega block in winter

There is a huge difference in the predominant effects between summer and winter because, in winter, the radiative heating by the sun plays much less of a role due to the shorter days and the lower inclination. So, as in summer, blockings are co-located with high-pressure systems that cause clear sky conditions. But in winter, the radiative cooling during the night is the dominant effect, and now the adiabatic heating caused by the subsidence is counteracted and mostly compensated by the radiative cooling. Therefore, in winter, cold air advection becomes the most important effect. This is shown in Figure 2.4 (a). Hence, the area most affected by temperature extremes is not exactly co-located with the blocking itself but shifted more to the southeast, where the northern wind effectively advects the cold air masses from the north.

3 Data and Methods

The first part of this chapter will introduce the data used in this thesis and explain the basic parameters and fields used. The second part will describe the methods applied to this data and some definitions that will be used.

3.1 Data

For historical data, we will rely on reanalysis data (ERA5) while for studies of the impact of climate change, two different climate models and approaches will be used (AWI-CM and ICON timeslice). The different data and models will be very briefly explained below.

3.1.1 ECMWF Reanalysis v5 (ERA5)

ERA5 is the fifth generation of atmospheric reanalysis provided by European Centre for Medium-Range Weather Forecasts (ECMWF) using the 4D-Var data assimilation technique. Its climate data spans the period from 1940 to the present and covers the full globe. It is produced by the Copernicus Climate Change Service (C3S) at ECMWF, which also provides up-to-date information on ERA5 data (C3S, 2024).

The data are available up to hourly time resolution and provide an exhaustive number of atmospheric, surface, land, and oceanic variables. The horizontal resolution is a 31 km grid, and vertically, it covers a height up to 80 km from the surface, divided into 137 hybrid sigma/pressure levels. The data is also provided on 37 interpolated pressure levels with a typical vertical resolution in the troposphere of about 25 hPa. All the variables come with uncertainty information at coarser resolutions based on a ten-member ensemble. (Hersbach et al., 2020)

For this thesis, we will only look at the daily data at 0 UTC from 1940 to 2019, and for some analysis, we will use the data up to 2022.[1]

[1] For detrending and studies of blockings and heatwaves/cold spells, the data up to 2022 is used, but for the zonal wavenumber decomposition, only the data up to 2019 was used.

3.1.2 AWI Climate Model (AWI-CM)

The AWI Climate Model (AWI-CM) is a global coupled atmospheric and ocean model consisting of an atmospheric model, an ocean model, and a coupler.

The atmospheric model used is the ECMWF model branched by Hamburg (ECHAM) in its sixth generation (ECHAM6), provided by the Max Planck Institute for Meteorology in Hamburg. It is a general circulation model for the atmosphere consisting of a dry dynamical core based on the primitive equations, a transport model, a toolbox of many physical parameterizations for irreversible diabatic processes, and data sets providing external parameters as boundary conditions. It has been improved and refined over 25 years in different versions up to the current version 6, which will be used here. More detailed information can be found in Stevens et al. (2013).

The used ocean model is Finite Element Sea Ice-Ocean Model (FESOM) v.1.4 (FESOM14) in version 1.4, which uses an unstructured mesh with higher resolutions in areas of particular importance and lower in others. The solver for the primitive equations is based on the Finite Element method with an advanced two-step solving algorithm and an adaptive 3D mesh derived by the 2D surface nodes. It not only models the oceans in 3D but also includes sea ice modeling. Further information can be found in Wang et al. (2014).

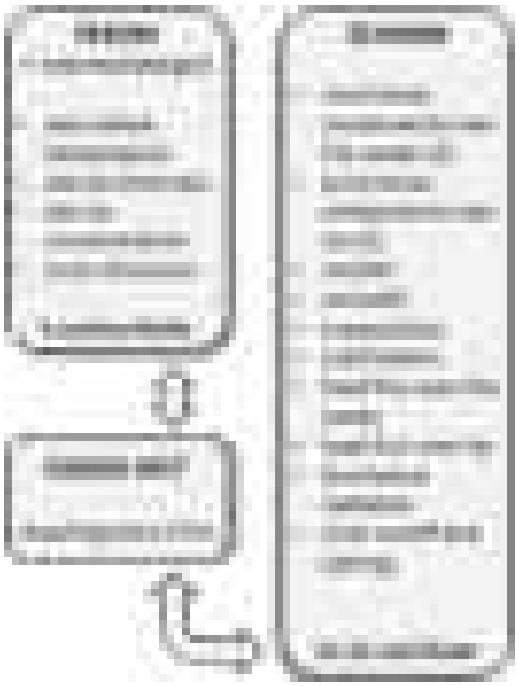

Figure 3.1: The basic coupling procedure used by AWI-CM taken from FESOM team (2020).

The OASIS coupler interfaced with the Model Coupling Toolkit (OASIS3-MCT) is used to exchange information between the atmospheric model ECHAM6 and the sea-ice ocean model FESOM14 where the coupling is performed every 6 hours. An overview of the relevant fluxes between air and sea, as well as the relevant surface fields of the ocean model that are used by OASIS3-MCT for the coupling, is shown in Figure 3.1. Further information can be found on the website FESOM team (2020) and in Craig et al. (2017).

The specific model variant from which the data in this thesis were taken is the Coupled Model Intercomparison Project 6 (CMIP6) AWI-CM-1-1-MR with a horizontal resolution of about 100 km in the atmosphere (Semmler et al., 2020). We use the deterministic run of the AWI-CM with two different emission scenarios, namely the Shared Socioeconomic Pathway 5 with an additional forcing of 8.5 W/m² in the year 2100 (SSP585) and Shared Socioeconomic Pathway 3 with an additional forcing of 7 W/m² in the year 2100 (SSP370) from CMIP6.

3.1.3 ICON timeslice experiments

ICOsahedral Nonhydrostatic (ICON) is a weather and climate modeling system developed jointly by the German Weather Service and the Max Planck Institute for Meteorology. As the name suggests, it uses an icosahedral-triangular grid with sophisticated nesting capabilities. It is a flexible model with many configuration options and additional packages with many use cases, from high-resolution regional short-term predictions to global climate studies with aerosols and reactive trace gases. Its core component is an atmosphere model (ICON-A) with a non-hydrostatic dynamical core usually coupled to the ocean model (ICON-O), including a sea-ice model. But in this case and for this thesis, the data produced with ICON uses prescribed SST and Sea-ice concentration (SIC) as well as prescribed greenhouse gas (GHG) concentration. Further information about the ICON model can be found at DWD (2024), in Prill et al. (2020) and about the atmosphere model, e.g., in Crueger et al. (2018).

For our studies, we run the atmosphere component of the ICON model only without coupling it to the ocean model. Instead, the boundary conditions for SST and SIC are prescribed, which has the advantage of using up fewer computing resources. We use so-called timeslice experiments, which means these boundary conditions are repeated over and over again for each year. I.e. the model is not simulating a continuous progression forward in time, but instead, it is fixed at certain years, which are then simulated over and over again, hence the name timeslice. This is done with the intention of producing relatively high statistics at the discrete baseyears with a feasible amount of computing time, but comes at the cost of lacking the years in between.

For practical reasons (because these model and script files were already available and tested), I used the years 2000, 2040, and 2090 as baseyears for the time slice experiments because it enabled me to run the model experiments on my own despite my limited experience and knowledge of the model. For the year 2000, the boundary conditions were taken from observational data, specifically the monthly mean data from AMIP (see PCMDI, 2023). For the year 2040 and 2090 the SST and SIC were taken from the SSP585 scenario from the Alfred-Wegener-Institut (AWI) CMIP6 simulations (Semmler et al., 2020). Observational data was used for the GHG concentrations for the year 2000, while for the years 2040 and 2090, data from the Representative Concentration Pathway with an additional forcing of 8.5 W/m² in the year 2100 (RCP8.5) scenario was used. Each base year was then simulated for at least 35 years with yearly recurring boundary conditions with a horizontal resolution of about 80 km. The first five years were omitted from the analysis and considered spin-up time, leaving us with usable statistics of 30 years of data for each base year. Further details

about the setup and boundary conditions can be found in the dissertation of Braun (2021) from which the scripts for the timeslice experiments originated.

3.1.4 Variables and fields

In this thesis, we will focus on the horizontal wind (mainly the meridional wind component) at jet stream level, which we will here define as 250 hPa[2], the geopotential height at the middle troposphere (500 hPa), and the temperature in the lower troposphere (850 hPa) as well as the near-surface temperature (2 m).

3.2 Methods

3.2.1 Anomaly calculation and detrending

Anomalies of 2 m temperature (T2m), 850 hPa temperature (T850), and geopotential height (Z500) are calculated by first applying a 30-day rolling average to the corresponding field. This is done for each grid point individually to smooth the data and eliminate daily variations. Then, for each day of the year and grid point, the mean climatology, i.e., the average from 1940 to 2022, is calculated and subtracted from the daily fields. This yields the anomaly that still shows a significant global warming trend (and positive trend in geopotential height, respectively), especially for the years after about 1980 as can be seen in Figure 3.2 (a) and (b) (and Figures 8.1, 8.1).

To not influence our correlation studies by this global warming signal[3], we additionally apply a detrending procedure to the data. This is shown in Figure 3.2 for the 2 m temperature as an example. Since there is not too much of a difference in the trend for the seasons (at least for the anomalies, i.e. after subtracting the mean climatology as explained above) and the four seasons show nearly the same trend as the yearly average, the latter is used to detrend the data (Figure 3.2 (a)). However, the annual average (even when taken as the areal mean) still shows a lot of year-to-year fluctuations, so this value cannot be used directly.

On the other hand, looking at Figure 3.2 (b), the trend is not strictly linear, which prevents us from using simple linear regression. So, I decided to split the data into two time periods: the first part, from about 1940 to 1979, doesn't show any linear trend. Therefore, I just used the average over this period for this part. From 1980 on, there seemed to be a clear linear trend, so I used linear regression to fit a trend line. The combination of both periods is then used as the fitted trend and subtracted from the anomalies to yield the detrended anomalies used in the analysis. The resulting

[2] The subtropical jet stream has its maximum usually rather at 200 hPa while the mid-latitude jet has its rather at 300 hPa. The wind field at 250 hPa proved as a good compromise to cover the features of both jet streams. We have also done some sensitivity analyses using 300 hPa instead of 250 hPa and we couldn't find any significant differences.
[3] Because later years, in general, show a higher positive anomaly that is not representative of the anomaly considering climate change.

(a) Seasonal anomaly (annual means) and fit to the data

(b) Trend of annual mean anomaly and fit to the data

(c) Distribution of daily raw data (offset removed), anomaly, and detrended anomaly

(d) Mean detrended anomaly data by day of year (and season in color).

Figure 3.2: Detrending of 2m temperature anomaly with ERA5 data from 1940–2022. Shown here is only the areal mean for a region from -10°W to 50°E in latitude and 40°N to 60°N in longitude while the actual detrending is done for each grid point independently.

distribution of the detrended values is shown in Figure 3.2 (c) for the areal average of the 2 m temperature.[4]

However, looking at the mean detrended temperature anomaly by day of the year and by season (Figure 3.2 (d)), the method is not perfect, and the seasonal means show minimal offsets. This is due to the smoothing of the data for the anomaly calculation via applying the rolling average and expected, because of the curvature in the annual temperature cycle.[5] These differences are small compared to the variance and the trend discussed before and should only minimally affect our analyses.

[4] Unfortunately, I forgot to force the initial point at the year 1980 of the linear trend to be equal to the mean value of the period before. That is the reason there is a small discontinuity between the years 1979 and 1980, but this is rather small compared to the overall trend and the fluctuations and is therefore thought to have only a negligible effect on the results.
[5] Looking at the annual temperature cycle this becomes clear: For the hottest days in summer the centered rolling average will always be lower then the maximum, i.e. after subtraction the remaining anomaly will have a positive offset. This is also true for other days in summer (and to a lesser extent in spring) due to the negative curvature of the temperature curve, i.e., the centered rolling average is lower than the midpoint. The same is true for winter (and autumn) but in the opposite direction.

The same method is used to yield detrended anomalies for the 850 hPa temperature (shown in (Figure 8.1) and the 500 hPa geopotential height (Figure 8.2) which will be used later in correlation analysis and to select specific days with extremes, i.e. days that exceed certain thresholds, and for calculation of blocking indices.

3.2.2 Definition of heatwave and cold spell

For the definition of a heatwave used in this thesis, we require the detrended temperature anomaly to be above the seasonal specific 95 % percentile of the temperature anomaly. This is calculated individually for each grid cell. Then, for each grid cell, whether this requirement is fulfilled for at least 5 consecutive days is checked. Only if this is true the event is classified as a heat wave. In some analyses, additional conditions will be placed on the minimal area for which this requirement has to be fulfilled, which will be stated then if applicable.

We use the same procedure to define a cold spell. Still, instead of requiring the detrended temperature anomaly to be above the 95 %-percentile, it must be below the 5 %-percentile for 5 consecutive days. The area requirements, where applicable, are the same.

For simplicity, we omitted to check whether the region above the percentile threshold for at least 5 days is connected. This could be further improved, but it is not expected to have a large impact because such strong heat anomalies are usually caused by general weather situations that affect connected areas.

The terms "heatwave" and "cold spell" will be used rather loosely in this thesis (but according to the above definition) and will not only be used concerning the 2 m temperature but, at times, also for the temperature at 850 hPa. In those cases, it will be explicitly mentioned which temperature it is referring to.

3.2.3 Blocking definition

For the definition of blocking, in terms of our analysis, we refer to the paper Woollings et al. (2018). We are using the absolute method, and for comparison, also the anomaly method. Both methods will be slightly adapted for our purposes.

Absolute method of blocking detection

The absolute method uses the absolute values of the geopotential height field at 500 hPa pressure level, hence the name "absolute". The principal idea behind this method is that a blocking is characterized by an inversion in the meridional gradient of the geopotential height field. In contrast, the mean background field has a negative gradient from the low latitudes, with a maximum close to the ITCZ, towards the poles where it reaches minimal values. During a blocking there is a significant deviation in this field, with a region of higher geopotential heights at the mid-latitudes.

Therefore, the gradient north of the blocking is expected to have a higher negative slope. At the same time, there is an inversion in the gradient south of the blocking, with the meridional gradient becoming positive. This leads to the first two requirements for the absolute method:

1. The gradient to the north, calculated by looking at the geopotential height difference 15° north of the latitude in question, has to be smaller than $-10\,\mathrm{gpm/°}$.

2. The gradient to the south, calculated by looking at the geopotential height difference 15° south of the latitude in question, has to be larger than 0.[6]

To be less sensitive to cut-off lows and subtropical ridges, which can also infer a positive meridional gradient to the north of these features, additionally, the gradient is required to be negative further south of the region with the positive gradient, namely:

3. The gradient further south, calculated by the difference in geopotential height -30° south to -15° south of the region in question, needs to be smaller than $-5\,\mathrm{gpm/°}$.

All these 3 requirements are checked for each grid point in the region of interest but with the additional requirement of the latitude to be within the range of 40°–70°N. Each grid cell that fulfills all three requirements is considered a blocking candidate.

When we talk about blockings, we actually mean persistent blockings; therefore, to be a blocking, the above conditions must be fulfilled for at least five consecutive days. In the final step, we want to filter out small-scale structures or fluctuations and dismiss all persistent blocking candidates where the 5-day overlapping area is smaller than 500 000 km². All the remaining regions are then marked as blocking.

Anomaly method of blocking detection

The anomaly-based method is comparatively simple: First, we calculated the daily detrended geopotential height anomalies (Z500 anomalies), as described earlier in this section, for each grid cell. Then we consider all Z500 anomalies above the 90th percentile of the seasonal anomaly distribution over 40–70°N a candidate cell for a blocking. Then we keep only the days and cells where the total area of the candidate grid cells exceeds at least $2 \cdot 10^6$ km². Then, we check that the 5-day overlapping area of the candidate cells extends at least 500 000 km² to ensure the persistence and stationarity of the blocking.

3.2.4 Zonal wavenumber decomposition

In the method of zonal wavenumber decomposition, the full field is decomposed into the different fields corresponding to different zonal wavenumbers. The full field is then the superposition of the

[6] One should note that the meridional gradient in this context is always defined as the change from south to north.

fields at all the wavenumbers. For each wavenumber k the field, here for the meridional wind v as an example, at a given latitude can be written as a perfect zonal sinusoidal circumglobal wave:

$$v_k(\lambda,t) = A_k(t)\cos\left(k\lambda + \varphi_k(t)\right)$$

where λ is the longitude, t the time, A the amplitude, k the zonal wavenumber with k and φ the phase of the wave. The superposition of all wavenumbers k then yields the full field again, as described earlier:

$$v(\lambda,t) = \sum_{k=0}^{\infty} v_k(\lambda,t) = \sum_{k=0}^{\infty} \left(A_k(t)\cos\left(k\lambda + \varphi_k(t)\right)\right)$$

So, this method is basically a Fourier transformation of the corresponding fields

$$a_k(t) = \frac{1}{\pi}\int_{\lambda=0}^{2\pi} v(\lambda,t)\cos(k\lambda)d\lambda$$
$$b_k(t) = \frac{1}{\pi}\int_{\lambda=0}^{2\pi} v(\lambda,t)\sin(k\lambda)d\lambda$$

with the Fourier coefficients a_k and b_k that yield the total amplitude $A_k = \sqrt{a_k^2 + b_k^2}$ and phase $\varphi_k = \arctan(b_n/a_n)$.

It has the advantage that it's very robust and easily calculated. Also, the interpretation in terms of zonal wavenumbers is relatively intuitive. Illustrative, the zonal wavenumber is the number of wavelengths that fit along the global latitudinal circle. Or, in other words, it gives the number of maxima and minima that can be found along the circumglobal latitudinal circle. E.g., a zonal wavenumber of five means that the corresponding wavelength is one-fifth of the length of the full latitudinal circle. And, following the latitude once around the globe, you'll encounter five minima and maxima for this zonal wavenumber, where the position of the maxima and minima is given by the phase of the zonal wavenumber decomposition.

This method can decompose any scalar field into its zonal wavenumber components. In the case of vector fields (e.g., the wind field), we first have to reduce them to scalar fields by either selecting only one component of the vector field (e.g., only the meridional component) or by projecting it onto a specific plane or by calculating a derived scalar field (e.g., the absolute value/magnitude of the 3D vector). Since we can apply this procedure independently for each latitude or altitude, the method can also be applied to 3D fields.

In our case for the Rossby wave dynamics, we are mostly interested in the meridional wind component at a certain pressure level because the meridional component of the wind reflects the north- and southward meandering of the jet stream, and, hence, the positions of troughs (negative meridional wind to the east and positive to the west of the trough) and ridges (positive meridional

wind to the east and negative to the west of the ridge) along it. If not stated otherwise, we look at the 250 hPa pressure level to be able to detect all the relevant features of the subtropical and polar jet stream.

How this zonal wavenumber decomposition looks in practice is illustrated in Figure 3.3 using the meridional wind at 250 hPa from the ERA5 data for a randomly picked date, here the 28th of January 2008. The left column of the figure shows only the part of the wind field belonging to one specific wavenumber; the wavenumber corresponds to the row of the plot. The right column of the figure shows the superposition of the first n wavenumbers, where n is the column, e.g., the first row shows only the first wavenumber (in this case, this is identical to the left column), and the fifth row shows the superposition of the first five wavenumbers (i.e., adding up the first 5 plots in the left column). It can be seen that the first couple of wavenumbers are enough to reconstruct the large-scale features of the atmosphere, while going towards higher wavenumbers features at smaller scales are subsequently resolved.

Applying to non-circumglobal waves

Usually, this method is applied to circumpolar Rossby waves, but we can also apply this method to a longitudinal sector of the hemisphere only. In our case, we are interested specifically in the region from 90°W to 60°E and the above equations have to be adapted accordingly, i.e. the integral is only calculated over the longitude region of interest (and this has also to be taken into account in the normalization) e.g.

$$a_k^{\mathrm{NAE}}(t) = \frac{2 \cdot 150^\circ}{360^\circ} \int_{\lambda'=-90^\circ}^{60^\circ} v(\lambda', t) \cos(k\lambda') d\lambda'$$

with λ' now the longitude in ° and not radians as λ was before. The calculation for the coefficient b_k^{NAE} has to be adapted accordingly and the amplitude and phase calculation stays the same except now using these modified coefficients, i.e. the amplitude becomes $A_k^{\mathrm{NAE}} = \sqrt{(a_k^{\mathrm{NAE}})^2 + (b_k^{\mathrm{NAE}})^2}$ and the phase $\varphi_k^{\mathrm{NAE}} = \arctan(b_n^{\mathrm{NAE}} / a_n^{\mathrm{NAE}})$.

It should be mentioned that this method is also able to identify Rossby wave packets with a limited spatial extent. Even though they might appear somewhat diluted because of the averaging process along the selected longitude range, they will still be detectable in the wave spectrum as long as their extent covers part of the selected region. This is also the benefit of applying the method only to a limited longitude extent because those wave packets will show up clearly in the spectrum as long as they cover some portion of the selected region.

Phase speed

We use the simple approach of calculating the phase difference of two adjacent days to calculate the phase speed. This yields the phase speed in radians per day (or degrees longitude per day)

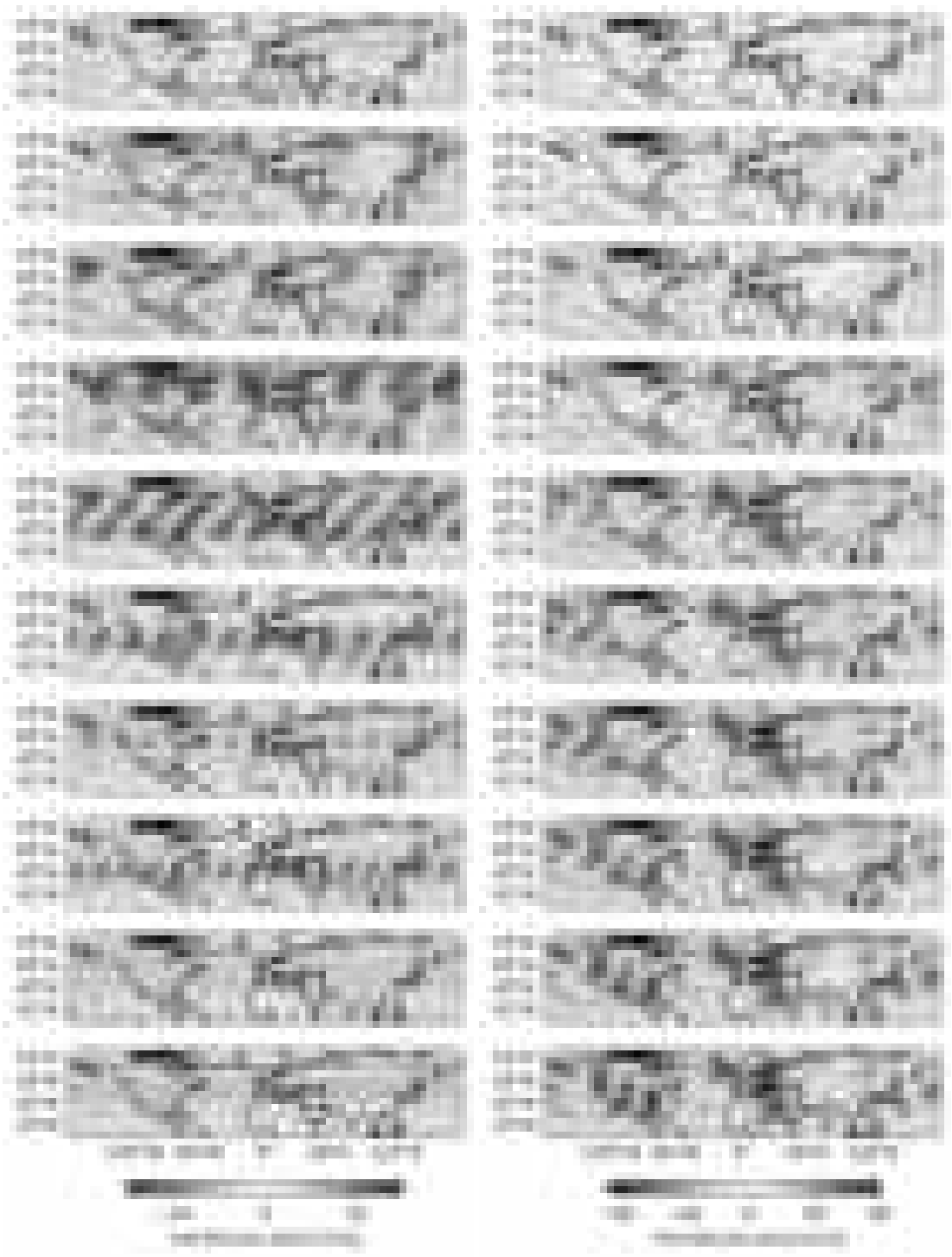

Figure 3.3: This picture illustrates the zonal wavenumber decomposition, from top (wavenumber 1) to bottom (wavenumber 10). In the left column are the contributions of the individual wavenumbers to the total wind field shown. In the right column, the superposition of all zonal wavenumbers up to the zonal wavenumber on the left-hand side is shown, which is the resulting field.

and is assigned to the later day of the two adjacent days. So, actually, this is the average phase speed of the 24-hour period prior to the date it is assigned to. We could have used a more advanced technique like linear or polynomial interpolation, but due to simplicity, we didn't.

One important aspect when calculating phases is their periodicity, so, e.g., +270° and -90° are the same. Therefore, we chose to always use the minimum value of the absolute value, in this example -90°, i.e., the range is always between -180° and +180°.

This has the implication that for higher phase speeds, i.e., if the wave is traveling in the order of half of its wavelength or above per day, we are not able to know by just looking at the calculated phase speed whether the actual wave was moving westward or eastward. Since the periodicity scales with the zonal wavenumber, this becomes problematic at some point for higher wavenumbers, i.e., as soon as the absolute value is in the order of $\frac{180°\text{lon}}{k\ \text{day}}$ or above where k is the wavenumber. So, for wavenumber 5, this can cause issues already at phase speeds around $\pm 18°$lat/day. Typical phase velocities that we will encounter in our analysis are in the order of $\pm 10°$lat/day, but of course, the values in the tails of the distribution can be above this value, i.e. in general, we have to be very careful interpreting the phase speeds (and any derived quantity), especially for wavenumbers around and above 9.

3.2.5 Low-pass and high-pass filtering

To separate the stationary and transient components of the fields, we apply a low and high pass filtering of these fields. Here, we use a rather simple filtering method without any window functions or similar. For low-pass filtering, just a centered rolling window average with a fixed time window (mostly 21 days, but for comparison and cross-validation, a window size of 5 days was also tested, but will not be further covered in this thesis) is applied. The resulting field of this rolling window average will be termed the "stationary part" in the following. The high-pass filtering is done by subtracting the rolling window average (transient part) from the daily fields. This is called the "transient part" because it is the deviation from the low-pass filtered background fields.

Figure 3.4 as an example shows the result of such a filtering process. The 21-day (3 weeks) filtering was chosen, because it is short enough to allow for (and follow) intra-seasonal changes while still being long enough to capture all the relevant transient features like moving highs and lows that are typical on timescales of about a couple of days. Usually, one would use rather shorter time windows (5–10 days) for the transient part. However, because we are specifically interested in studying the behavior of blockings on the same time scale of 5–10 days (sometimes even longer), I decided to use a longer time window to not filter out features that might be relevant regarding the blocking.

In our analysis, we will combine the high-pass (and sometimes low-pass) filtering with the zonal wavenumber decomposition, i.e., we will apply the zonal wavenumber decomposition to the high- or low-pass filtered meridional wind field. The result will then be called "stationary Rossby waves" for the low-pass filtering and "transient Rossby waves" in the case of the high-pass filter, respectively.

(a) No filtering, i.e. all parts

(b) Only stationary part

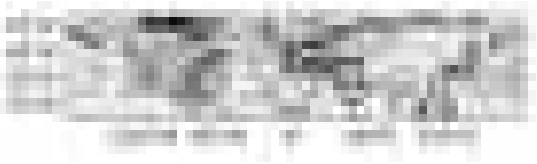

(c) Only transient part

(d) Stationary part 2 days later

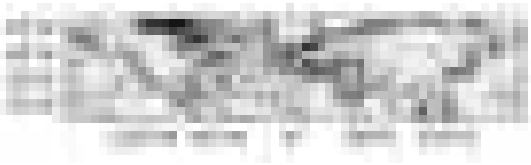

(e) Transient part 2 days later

Figure 3.4: This picture visualizes the high- and low-pass filtering. It uses the meridional wind field at 250 hPa on 2008-01-28 (upper two rows) and 2008-01-30 (bottom row) as an example to show the effect of the filtering. As can be seen in subfigures (b) and (d), the stationary part is nearly constant at short timescales, while the transient part shows the propagating wave patterns.

4 Rossby wave activity in reanalysis data

In this chapter, we are going to apply the method of zonal wavenumber decomposition to reanalysis data (ERA5) to study the wave spectrum at the different seasons and compare the circumglobal wave spectrum to the one for a sector that only extends from the Atlantic Ocean to Europe. Last but not least, we also want to test whether there are already any (significant) trends visible in the 80 years of reanalysis data we are using here.

Of special interest is the wind field at 250 hPa, because this is where we can see the signatures of both jet streams most clearly. Because the waviness and meandering of the jet stream are strongly connected to meridional wind anomalies, we look at the meridional wind field and apply the method of zonal wavenumber decomposition. This wind field consists of stationary and transient components of Rossby waves which are superimposed. Therefore we further apply a 21-day rolling average filtering to separate the stationary from the transient parts. Most of our interest will be in the transient parts because these are the Rossby waves traveling along the jet stream and can cause Rossby wave breaking and have a huge impact on blocking events.

4.1 Climatology

4.1.1 Full northern hemisphere (circumglobal waves)

Looking at the amplitude of the zonal wavenumber decomposition of the meridional wind field at 250 hPa, one can clearly see its seasonality. This is not at all unexpected because, in the boreal winter, the jet stream is blowing much stronger and more consistent than in the boreal summer.

This is reflected in Figure 4.1 where in winter (a) the amplitudes are much higher than in summer (c). Spring and autumn lie somewhere in between, while autumn has, in general, higher amplitudes (at the mid-latitudes partly even higher than in winter). In summer, on average, the maxima tend to be at higher zonal wavenumbers at mid-latitudes, i.e., there are more Rossby wave components with lower wavelengths compared to the higher latitudes. But one has to take into account that at higher latitudes the wavenumbers are in general smaller, because the wavenumber is the length of the latitudinal circle divided by the wavelength. The length of the latitudinal circle decreases with the cosine of the latitude. I.e., the wavenumber at e.g. 70°N is only half that at 45°N for a wave with the same wavelength. That matches quite well with the observation where we can see the maximum at 45°N around wavenumbers 5-7 and at 70°N more around 2-3.

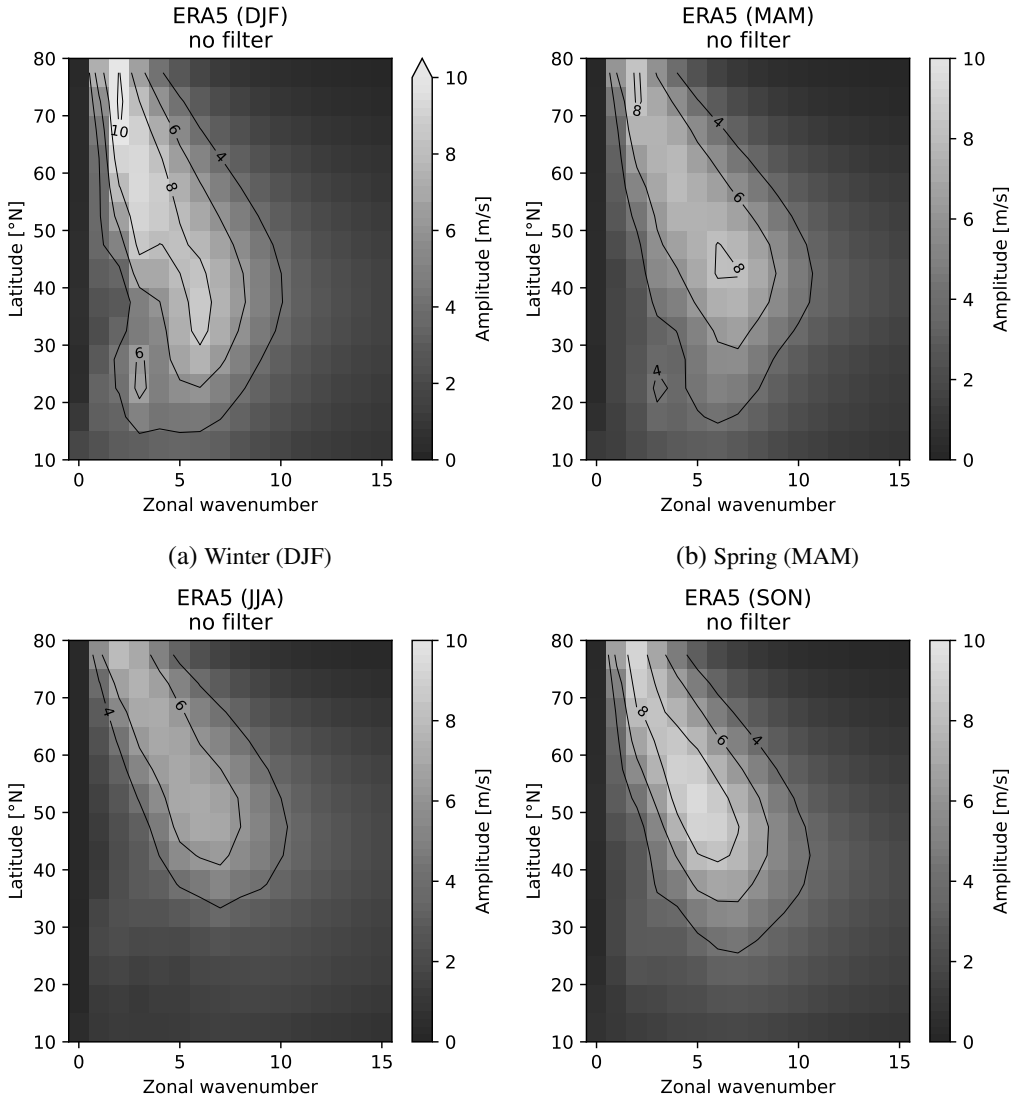

(a) Winter (DJF)

(b) Spring (MAM)

(c) Summer (JJA)

(d) Autumn (SON)

Figure 4.1: Amplitudes of zonal wavenumber decomposition of the meridional wind at 250 hPa (averaged over the years 1940 till 2019) for the full northern hemispheric circle.

It can be seen that for all seasons, there is a local maximum in the mid-latitudes. The location (latitude) of the local maximum also has a seasonal signature: in winter, it's at lower latitudes around 30-40°N and wavenumber 6. In summer, it's located around 45-55°N and wavenumber 6-7, with autumn very similar to summer (but at slightly lower wavenumbers 5-6) and spring around 40-50°N. But here, we are looking at the superposition of stationary and transient waves, so further interpretation is difficult without separating the parts from each other, which will be done now.

First, we will look at the stationary part in Figure 4.2, again, winter shows by far the strongest wave activity. This is due to the much stronger jet stream in this season, while in the summer, it is so weak that there are hardly any stationary waves. The strongest signature in winter is at wavenumber 2-3, a well-known pattern for this season, with stationary troughs mostly fixed in place downstream of large mountain ranges. The signature is much weaker for summer and tends more towards wavenumbers 5. The higher wave number is due to additional stationary features caused

by the heating of the continents and the relatively cold ocean surface, which causes quasi-stationary patterns of highs and lows over the continents (thermal lows) and the oceans (e.g. Azores High and Icelandic low). The overall slower jet stream supports this enhanced meandering of the jet stream.

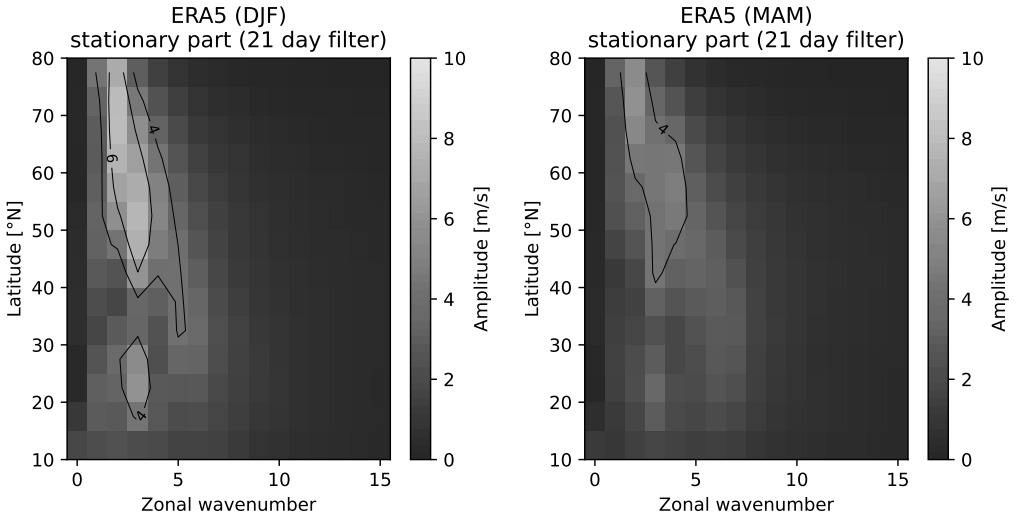

(a) Winter (DJF)

(b) Spring (MAM)

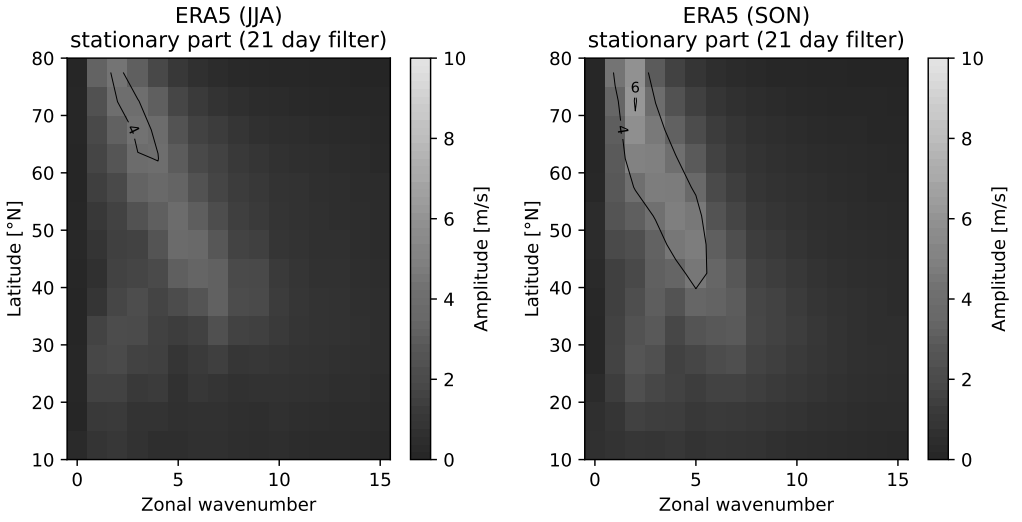

(c) Summer (JJA)

(d) Autumn (SON)

Figure 4.2: Amplitudes of zonal wavenumber decomposition of the stationary part with a 21-day lowpass filter of the meridional wind at 250 hPa (averaged from 1940 to 2019) for the full northern hemispheric circle.

The transient part is shown in Figure 4.3. Here we can see a clear maximum in the mid-latitudes and a correlation between lower latitudes and higher wavenumbers, as explained before. In winter, the maximum extends from around 30-45°N and at wavenumber 6-7. In summer the maximum is at higher latitudes 45-55°N but at similar wavenumbers 6-7. Autumn looks very similar to the summer but with slightly lower wavenumbers 5-6 and significantly larger amplitudes at the maximum. Spring is more between summer and winter, with a maximum of around 40-50°N at wavenumbers 6-7. All in all, the most pronounced transient part can be seen in autumn, and it is interesting to see that in winter, the wave activity extends that far south. The poleward shift in

winter and equatorward shift in summer reflects the shifting of the jet streams with the seasons and, therefore, also, the Rossby wave activity shifts along with the jet.

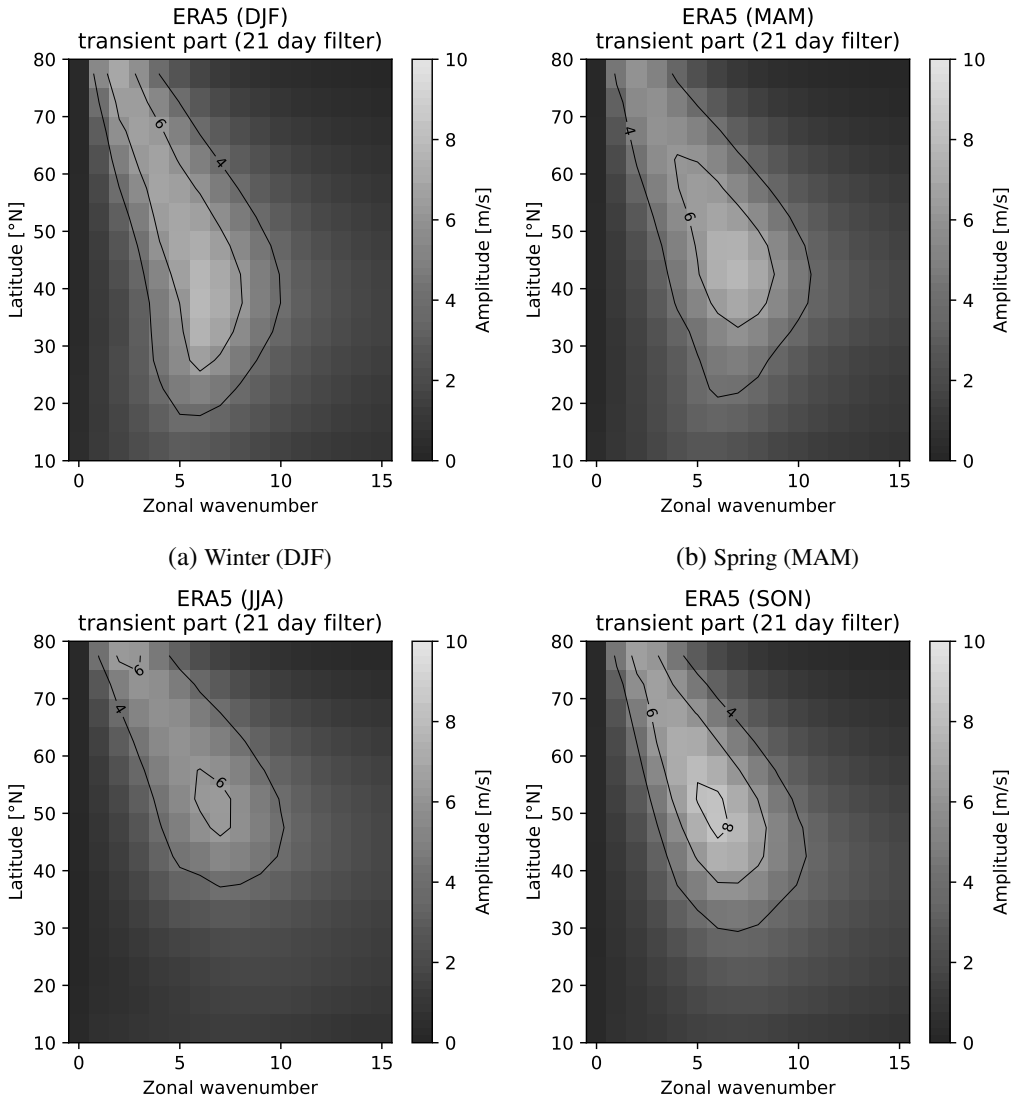

(a) Winter (DJF)

(b) Spring (MAM)

(c) Summer (JJA)

(d) Autumn (SON)

Figure 4.3: Same as Figure 4.2 but here for the transient part only.

4.1.2 North Atlantic and European sector (90°W–60°E)

As already mentioned before, the Rocky Mountains, the North American continent, and the Asian continent with its mountains, most importantly the Himalayan, have a huge impact on the jet stream and Rossby waves. This became already visible when looking at the stationary circumglobal Rossby waves (see Figure 4.2), where we observed stationary troughs and ridges that are kind of enforced by orography and thermal lows or other quasi-stationary features on the mean global circulation.

This also impacts transient Rossby wave packets because they cannot propagate freely past stationary obstacles like, e.g., mountain ranges. So, in a way, the large mountain ranges, in combination with further impacts of the continental masses like surface friction, thermal lows, seasonal monsoon

patterns, etc., divide the hemisphere into different sectors, where the wave propagation inside these sectors is freer than the propagation at the transition of these sectors. Therefore, it makes sense to treat different sectors of the Northern Hemisphere separately when looking at Rossby wave propagation.

We are interested in the impact on the weather in Europe and will therefore focus on the sector over the Northern Atlantic and Europe, which we define here as an extend in longitude from 90°W to 60°E. This is the most relevant region for Rossby waves that impact the weather over Europe because they usually appear east of the coast of North America[1] and then travel further east over the Atlantic Ocean until they reach Europe.

For the North Atlantic and European sector (NAE) sector, we can see the seasonality in the zonal wavenumber decomposition, quite similar to the circumglobal case. Comparing the North Atlantic and European sector (Figure 4.4) to the circumglobal case (Figure 4.1), on average, we find significantly higher amplitudes for NAE, e.g. compare the winter with a maximum of slightly above 8 m/s in the mid-latitudes for the circumglobal waves vs. around 13 m/s for the waves in the NAE region. This supports us in treating the NAE sector separately because it shows that the Rossby waves mostly do not uniformly extend around the globe but are separated into different sectors. So the Rossby waves of the different sectors are not combining in phase and with the same wavenumbers to one common circumglobal wave. Hence the resulting amplitudes of the circumglobal waves are lower than for the individual sectors. Of course, in the end, a circumglobal wave has to close, at least the stationary part.[2] So, at the transitions between these sectors, it cannot be out of phase, but in between, it can eventually become out of phase when the wavelength stays not exactly constant.

There are only minor differences to the full spectrum, apart from the difference in overall amplitude. For the NAE sector, it doesn't make too much sense to look at the stationary part isolated because the relevant signatures are mostly at small wavenumbers, i.e., these features can only be captured at large enough extents. Further, we have deliberately excluded the regions where these features are most pronounced.

We now want to look at the transient part with a 21-day highpass filter (see Figure 4.5). The pattern looks very similar to the circumglobal one (Figure 4.3), but notice the different scale. So, the amplitudes on average are much higher when only looking into the NAE region, which again supports us in treating this sector separate from the rest, as explained before. Besides, we observe the maximum amplitude in the NAE sector to be located at slightly higher latitudes: So, the maximum in winter is around 40–50°N (with tails far to the north) at wavenumber 6–7 with amplitudes of about 11–12 m/s, while in summer, the maximum is around 50–55°N also around the

[1] Actually, often they can also originate from somewhere over the east Pacific and propagate past the Rocky Mountains and the American Continent. But then the part of the wave east of the continent is not necessarily in phase with the part west of it, and it can still make sense to look only at the continuous part east of the continent to get a clearer picture of the wavelength, amplitude, and phase speed. Also, they can originate from the Tropics, but then they travel north until they hit the jet stream, which usually happens over the Atlantic Ocean.

[2] Actually, in reality, the jet stream is often not continuous, i.e., then, also, the waves don't have to be closed.

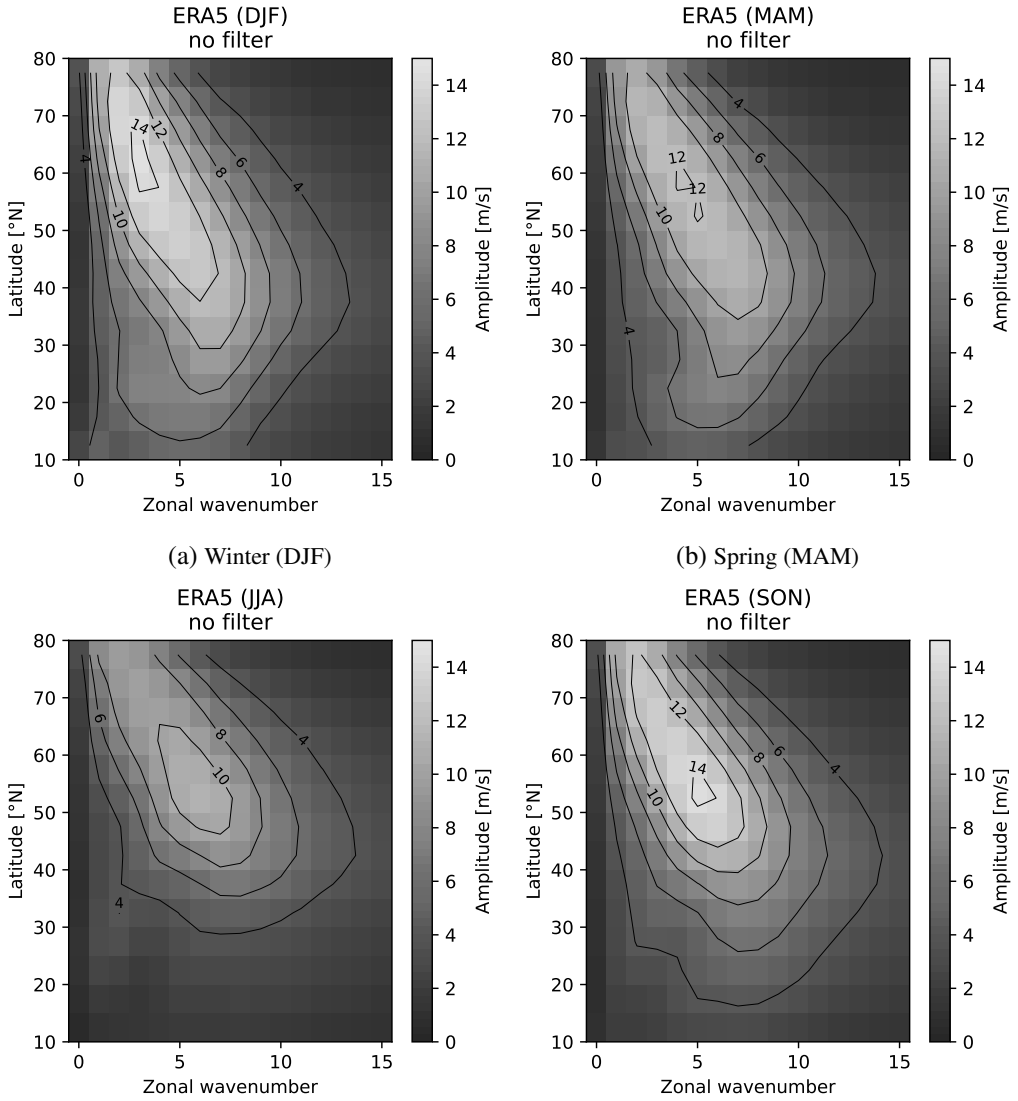

(a) Winter (DJF)

(b) Spring (MAM)

(c) Summer (JJA)

(d) Autumn (SON)

Figure 4.4: Same as Figure 4.1, but here only for the North Atlantic and European sector (90°W–60°E).

same wavenumbers with amplitudes around 8–10 m/s. For spring, it's around 40–55°N up to 10 m/s and in autumn, at 50–55°N with amplitudes up to 13 m/s.

One reason for that shift of the maximum towards higher latitudes compared to the circumglobal spectrum, especially in the winter, is that here we are excluding the parts of the jet stream over the Asian and North American continent, where it is usually located at very low latitudes[3]. Apart from that, the seasonality reflects the same behavior as for the full hemisphere, i.e., the highest amplitudes are in autumn and winter, decreasing towards spring and summer, in agreement with the seasonality of the jet stream's strength.

[3] Outside of the Indian monsoon season the jet stream is located south of the Himalayan, and downstream of the Rocky Mountains the jet stream is also at relatively low latitudes

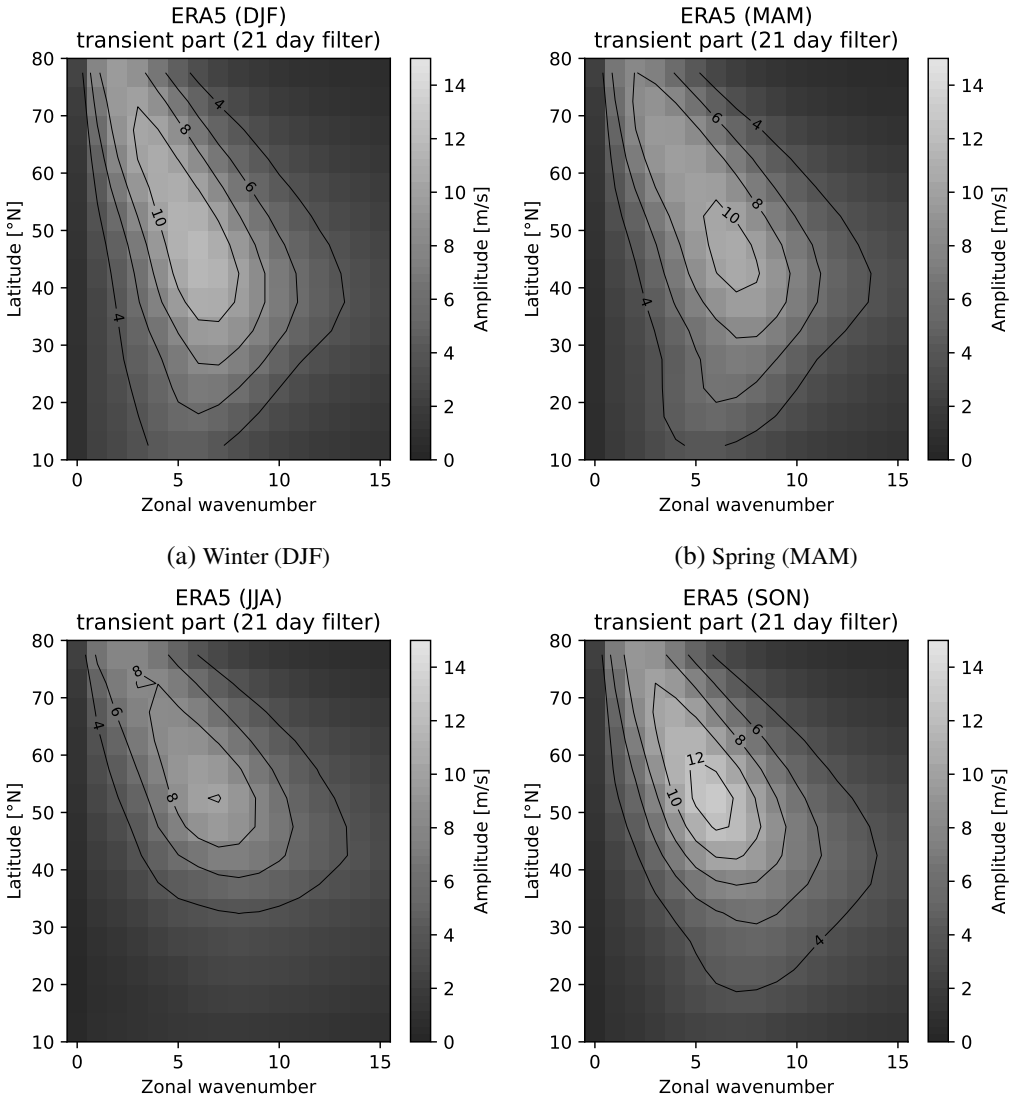

(a) Winter (DJF)

(b) Spring (MAM)

(c) Summer (JJA)

(d) Autumn (SON)

Figure 4.5: Same as Figure 4.3, but here only for the North Atlantic and European sector (90°W–60°E).

4.1.3 Phase speeds

Another interesting feature to study, apart from the amplitudes that reflect the wave activity's magnitude, is the Rossby waves' phase speeds. We do this by calculating the day-to-day difference between the phases as explained in the chapter 3. The result of this is depicted in Figure 4.6, which shows the mean phase velocities for different wavenumbers, latitudes, and seasons. To be able to identify the most relevant regions the plots are overlayed with contour lines that represent the mean amplitudes. We can see a smooth distribution with maximum values near the maxima of the amplitudes, but the whole distribution is slightly shifted about 2 wave numbers towards a higher zonal wave number.

From the theory, we know that Rossby waves at smaller wavelengths, i.e., with higher wavenumber, are carried away by the background flow quicker to the east than the ones with longer wavelengths, so a shift of the maximum speed towards higher wavenumber is expected. For very long wavelengths,

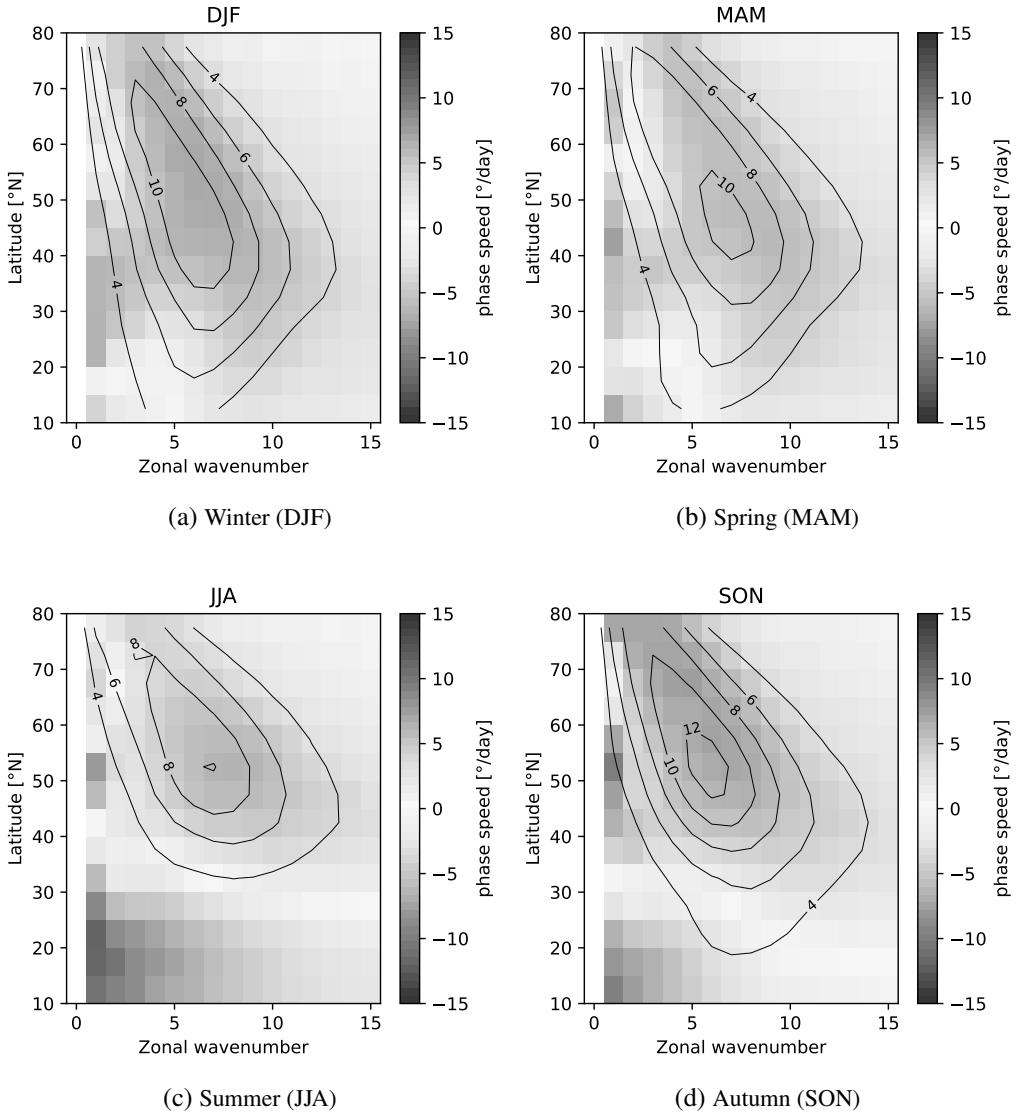

(a) Winter (DJF)

(b) Spring (MAM)

(c) Summer (JJA)

(d) Autumn (SON)

Figure 4.6: Phase speed of zonal wavenumber decomposition of the transient part of the meridional wind at 250 hPa (averaged from 1940 to 2019) for the North Atlantic and European sector (90°W–60°E). The contour lines reflect the magnitude of the mean amplitudes (see Figure 4.5).

at wavenumber 1 and partly for wavenumber 2, we can see that the Rossby waves even move retrograde at higher latitudes with respect to the ground. So, the decrease in speed towards lower wavenumbers is expected. But why the phase speed is at some point also decreasing towards higher wavenumbers (from around 2–3 wavenumbers above the maximum of wave activity) is not clear. It might be that in those regions, the waves are not continuous or disappearing rather quickly, which might lead to averaging effects where parts of different, non-related waves enter into the day-to-day difference calculation of the phase speed. Another effect, that was discussed in the Chapter 3, is that at smaller wavelength and higher phase speeds we are not able to resolve the direction of propagation anymore, due to the periodicity of the phase and because we are only using daily

time resolution.[4] But this cannot explain why this happens for higher latitudes already at lower wavenumbers.

Also, for the values at wavenumber 1, we have to be a bit careful with the interpretation, because we are only looking at 150° of 360° of the globe, i.e. less than one-half, which makes it very hard to detect wavenumber 1 waves with certainty, because in this sector not even a half wavelength can be observed. Luckily, this is not of much importance here because at the very low wavenumber, the amplitudes are negligible, i.e., there is no relevant wave activity, so the phase speed is not relevant.

Looking at the seasonality, the phase speed doesn't change too much with the seasons, even though it is a bit higher in winter and autumn. Also, we can observe westward moving waves even at higher wavenumbers for summer and autumn. This is due to the upper-level easterly winds around the ITCZ that extend far into the northern hemisphere in summer and autumn. However, this does not affect the analysis very much because the amplitudes at these latitudes and zonal wavenumber are negligible compared to the mid-latitudes. Also, this is located south of the subtropical jet and, therefore, is not of too much interest to our analysis.

4.2 Trends in reanalysis data

Finally, we want to check whether we can already observe some trends due to climate change in the reanalysis data. Therefore we use the ERA5 data from 1940–2019 and fit a linear trend to the amplitudes at different latitudes and wavenumbers to check for possible changes in the transient part of the Rossby waves. The p-value of the linear regression is used to evaluate the significance.

4.2.1 Full northern hemisphere

For the full northern hemisphere, the amplitude spectrum is shown in Figure 4.7. The coarse stippling in the figure marks regions where the trend was significant at the 95 % confidence level, and the fine stippling marks significance at the 99 % confidence level.

There seems to be a significant increase for winter, with a maximum increase of around 30-45°N at wavenumbers 6-7. This coincides with the maximum of the amplitude shown in Figure 4.3 (a) and hints towards an increase in wave activity at the mid-latitudes.

The spring result is not significant around the maximum wave activity everywhere, but a generally increasing trend is visible, with a significant maximum around 45-60°N at wavenumber 7. This is very close to the maximum in Figure 4.3 (b), but at higher latitudes, implying a poleward wave activity shift.

[4] We calculated already that for wavenumber 9, we cannot resolve the propagation direction for phase speeds around 10 m/s anymore. This also enters the mean value, i.e., if there are some days with a phase speed above 10 m/s, this will contribute to the average as a negative phase speed, resulting in a too-low average.

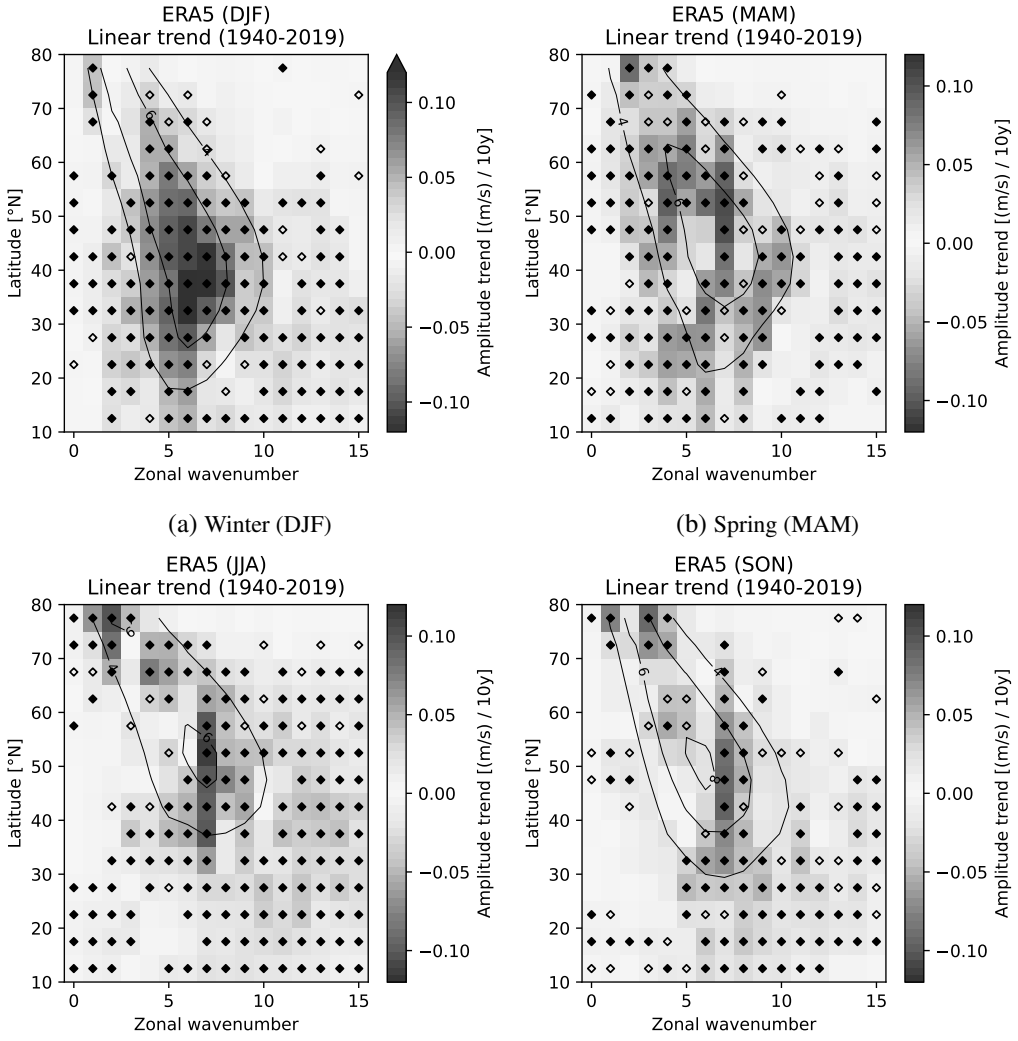

(a) Winter (DJF)

(b) Spring (MAM)

(c) Summer (JJA)

(d) Autumn (SON)

Figure 4.7: Linear trend of the wave amplitudes of the meridional wind at 250 hPa for the transient part. The colored values represent the slope of the linear regression from 1940 to 2019 for the full northern hemisphere. The open/closed diamond symbols mark areas where the linear trend is significant at the 95 %/99 % confidence level. Superimposed are the contour lines of the mean amplitude (see Figure 4.3) as reference.

For summer, it's less consistent because the area of significant changes is far more broken, and also, the region of maximum increase is neighboured by zones of (mostly non-significant) decrease in amplitude. Nevertheless, the highest increase is seen at wavenumber 7 from around 30-60°N, which, in a way, stands out from the rest. That also coincides with the maximum amplitude seen in Figure 4.3 (c) and is slightly shifted to higher wavenumbers.

Autumn looks very similar to summer, with the highest trend of increase around 40-55°N at wavenumber 7 which here also stands out a bit. Comparing this to Figure 4.7 (d), this would also imply a shift of the maximum towards higher wavenumbers.

However, these figures must be interpreted cautiously due to possible multi-annual and multi-decadal variability and oscillations. Also, this only resembles the global picture of the northern

hemisphere, but as argued before, we are mostly interested in the NAE sector, which will be addressed in the next section.

4.2.2 North Atlantic and European sector (90°W–60°E)

For the region 90°W–60°E we, again, fit the linear trend from 1940–2019 for the amplitudes at different latitudes and wavenumbers and check for significant changes in the transient part of the Rossby waves. Figure 4.8 shows this. Again, the open/closed diamond symbols in the figure mark regions where the trend was significant at the 95 %/99 % confidence level.

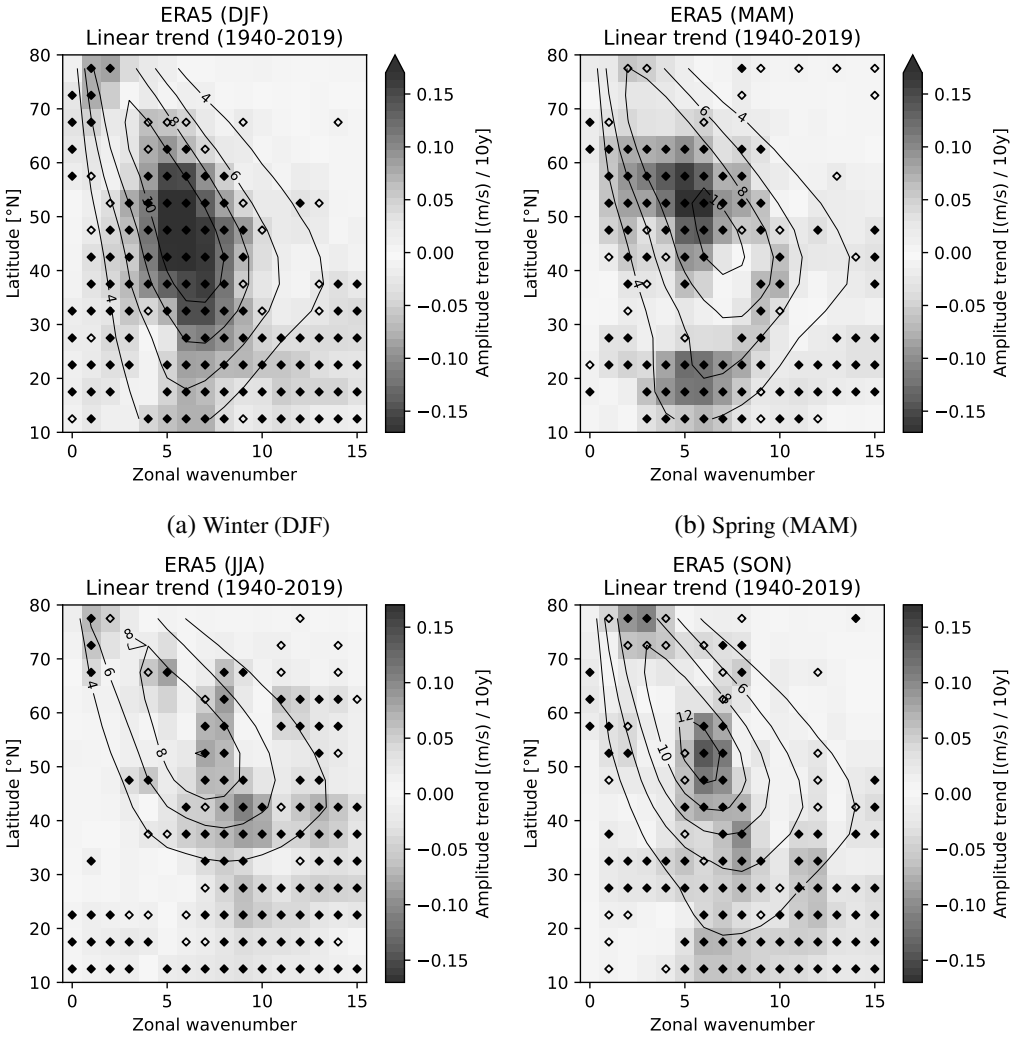

(a) Winter (DJF)

(b) Spring (MAM)

(c) Summer (JJA)

(d) Autumn (SON)

Figure 4.8: Same as Figure 4.7, but here only for the North Atlantic and European sector (90°W–60°E).

For winter there seems to be an area of significant increase, with a maximum increase around 40-55°N at wavenumbers 5-7. This coincides with the maximum of the amplitude shown in Figure 4.5 (a) and hints towards a general increase in wave activity at the mid-latitudes. Comparing this to the observed changes for the full hemisphere, the pattern is quite similar, but the increase is more pronounced and stronger in the NAE sector. Looking into the details of the linear regression,

which is shown in Figure 8.6 for wavenumber 5 and 6 at 40–55°N, there are larger multidecadal variabilities and oscillations. Still, over larger timescales (> 50 years), the trend seems to converge towards a significant positive value around 0.2 (m/s) per decade. This would imply an overall increase in wave activity at the mid-latitudes in winter, i.e., a stronger meandering jet stream.

The highest significant increase for spring occurs around wavenumbers 5–6 at 50-60°N. This implies a shift of the maximum towards higher latitudes and lower wavenumbers. For the circumglobal case, there was not such a clear signature, but instead, we had an increase in wavenumber 7 that cannot be seen here as strong. Looking at the time evolution in Figure 8.7 for wavenumber 5 and 6 at 52.5°N, one can see a quite consistent positive trend over most of the time period even though there are some fluctuations at timescales <45 years. Also, the trend is highly significant most of the time, especially at timescales >55 years. This hints towards a slight shift of the maximum wave activity towards higher latitudes, with generally increasing wave activity, except for a small patch around wavenumber 7–8 at 30–45°N, where there is no significant trend.

For summer, it's less consistent because the area of significant changes is far more broken, and also, the region of maximum increase is neighboured by zones of decrease in amplitude. Nevertheless, there is a region of significant increase at wavenumbers 7–8 extending all the way from 10°N–65°N (with the highest increase around 45-65°N), which suggests a shift of the maximum wave activity from wavenumber 6–7 towards higher wavenumbers. The highest increase is seen around wavenumber 9–10 at 35-45°N, implying an increase of wave activity at lower latitudes and higher wavenumbers. This differs from the circumglobal changes mostly because no such highly pronounced wave number 7 exists, but for wavenumber 7, there is still a significant positive trend. Looking at the time evolution shown for wavenumber 9 at 42.5°N (where the highest trend is seen) in Figure 8.8, it is not that clear whether this trend is converging, because there are huge fluctuations at longer time scales. The result is very sensitive to the chosen starting year of the analysis. However, on longer time scales (>60 years), the trend seems positive, but it's unclear and inconclusive.

Autumn looks very similar to summer, with the highest trend of increasing around 45-60°N at wavenumber 6–7. This would imply a general intensification of wave activity where there is already the highest wave activity. At latitudes >60°N or outside wavenumber 5-7 the trend is not significant anymore. It is different from the circumglobal case, where we had more of a dipole structure indicating a shift towards higher wavenumbers (again, mostly wavenumber 7), while here, it is more of an intensification around the region of maximum wave activity. However, looking at the details of the fit in Figure 8.9 for wavenumber 6 with the highest rate of change, the trend is not very consistent, and there are a lot of fluctuations on multiannual and multi-decadal timescales, and for most of the cases the trend is not significant. For wavenumber 7 it is quite similar, even though it tends a bit more towards a positive trend, but it's not unambiguous. So, we should be very careful with our conclusions in this case because the linear regression trends are highly affected by multi-annual oscillations during this season.

Phase speeds

For the NAE region, we also want to look into the trends of the phase velocity. This is depicted in Figure 4.9, where the values represent the linear regression trend from 1940 to 2019.

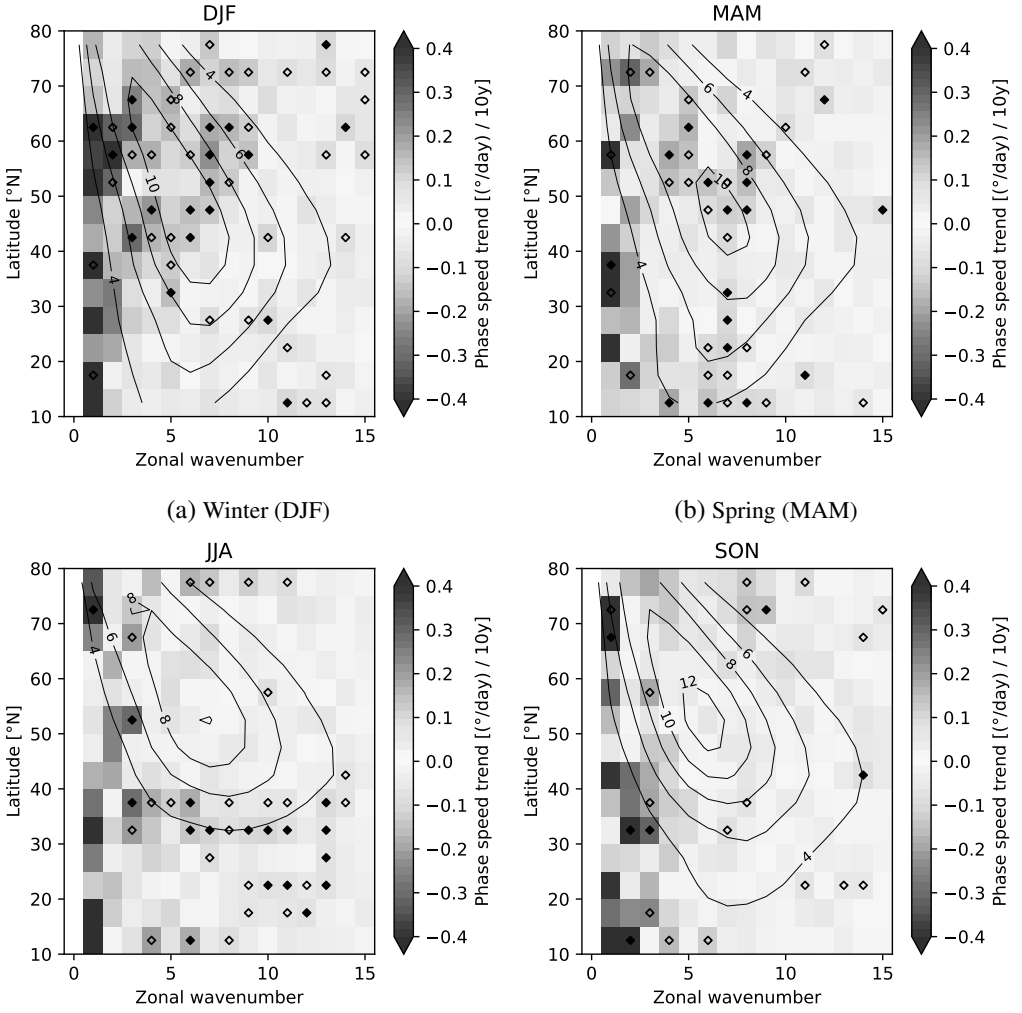

(a) Winter (DJF)

(b) Spring (MAM)

(c) Summer (JJA)

(d) Autumn (SON)

Figure 4.9: Linear trend of the phase velocity of zonal wavenumber decomposition of the meridional wind at 250 hPa (transient part with a 21-day highpass filter) for the ERA5 data and for the North Atlantic and European sector (90°W–60°E). The values represent the slope of the linear regression from 1940 to 2019. The open/closed diamond symbols mark areas where the linear trend is significant at the 95 %/99 % confidence level. Superimposed are the contour lines of the mean amplitude (see Figure 4.5) as reference.

For winter, we can see a clear positive trend in the region with the highest amplitude waves at mid- and higher latitudes, yet this is not significant everywhere. The picture at lower latitudes is less clear, but there seems to be a rather decreasing trend for very low latitudes (<30°N). It is much less uniform for spring, but there seems to be a positive trend at wavenumbers 7 and close to the peak of the maximum wave activity towards higher latitudes and smaller (and also larger) wavenumbers. For summer, there only seem to be significant trends at latitudes lower than the peak wave activity (around <40°N), but this is in a region with only minor wave activity. The trend for the areas with

the highest wave activity is ambiguous, and the trends are insignificant. For autumn, there is no clear picture at all, and there can be no conclusion drawn.

To complement this, we also looked into the trend in the number of days with slow-moving (i.e. <2°lon/day) waves, which reflect the same findings as for the trend in phase speed, and therefore, it is not shown here. The trend for the slow-moving waves is generally less significant (mostly due to fewer statistics). Only for summer, it looked a bit more uniform around the maximum wave amplitudes towards an increase of slow-moving waves, which would imply a reduction in phase speed. But this was not significant.

All in all, the data on phase speed don't allow for a clear conclusion, but there are hints of a slight increase in phase velocity at the maxima of wave activity for the winter and spring seasons.

4.3 Conclusion

Our analysis reveals significantly higher Rossby wave activity in the NAE region compared to the full northern hemisphere, particularly when examining the transient components of the wave spectrum. This finding suggests that Rossby waves do not propagate uniformly around the globe but instead exhibit regional partitioning. This observation validates our decision to focus on the NAE sector rather than the entire hemisphere.

The Rossby wave spectrum, i.e. the zonal wavenumber decomposition of the meridional wind, effectively captures the fundamental signatures and seasonality of the jet streams and the Rossby wave activity. This method proves to be a valuable tool for studying large-scale atmospheric phenomena associated with Rossby waves. By applying an additional high-pass filter, we can isolate transient Rossby waves, simplifying the complex nature of these waves into manageable 2D spectra of the most crucial features, namely the amplitude and the phase speed of transient Rossby waves, that facilitate trend analysis.

Examining the 80-year reanalysis dataset from 1940 to 2019, we observe a general increase in wave activity across all seasons, with the most pronounced increases occurring in winter and spring. While in winter the strongest increase is at the climatological maximum of wave activity, for spring, there is a shift of maximum activity towards higher latitudes. During summer, the maximum wave activity shifts mostly towards higher wavenumbers (7–8). The autumn trends are less clear due to the significant influence of multi-annual oscillations on the linear regression analysis.

Our analysis does not yield definitive conclusions regarding phase speed trends, as most trends are not statistically significant. However, there are indications of an increase in phase speed during winter and, to a lesser extent, in spring, particularly around the region of maximum wave activity.

In summary, our study underscores the importance of regional focus in analyzing Rossby wave activity and demonstrates the utility of the wave spectrum in capturing and understanding the

seasonal and long-term trends of these waves. The insights gained can contribute to a deeper understanding of atmospheric dynamics and the factors influencing extreme weather events.

5 Rossby wave activity in climate models

5.1 Comparison of climate models to reanalysis data

Before using the data from the climate models for further studies, we have to see how well these models perform in terms of the amplitudes and phase speeds in the zonal wavenumber decomposition because these are the relevant measures for us.

The best way to do this would be to compare the reanalysis data and the climate model data at the same time spans with the same boundary conditions. Unfortunately, for AWI-CM the data on servers of the Deutsche Klimarechenzentrum (DKRZ) were only available from the year 2020 on. On the other hand, for the ICON timeslice simulations, we only have the baseyear 2000 available close to the present. Therefore, I decided to use the first 10 years for the AWI-CM, but with the less strong warming scenario SSP370 to keep the bias a bit smaller than it would be for the SSP585 scenario. As a compromise, I chose to look at the seasonal average of the years 2000–2020 for the ERA5 data as a reference, to have overlap with the baseyear 2000 from the ICON timeslice simulations on one hand, and to be not too far away from the first 10 years of AWI-CM data on the other hand.

In the following, we have to consider that there is to be expected a small offset to the reference ERA5 data because, for the AWI-CM, we are comparing data that is, on average, 15 years later than the reference (2025 vs. 2010). For ICON timeslice, we are comparing a scenario that is, on average, 10 years earlier than the reference (2000 vs. 2010). But because we have already looked at the trend in the ERA5 data and know the numbers, we can also account for these differences–or at least we have an estimate on the magnitude of this effect (see Figures 4.8 and 4.9).[1]

Figure 5.1 shows the comparison of the seasonal mean amplitudes and Figure 5.2 shows the differences with respect to the ERA5 data. Be aware of the difference in scale for the difference plots which is for ICON timeslice data about a factor of 5 compared to AWI-CM.

The differences for AMI-CM SSP370 are in the order of $\pm 1\,\mathrm{m/s}$ while for the ICON timeslice the differences are in the order of $\pm 6\,\mathrm{m/s}$. To put this into perspective, the linear trend for the observed changes per decade in reanalysis data were in the order of $\pm 0.15\,\mathrm{m/s}$ (see Figure 4.8), so the effect

[1] In principle it would be possible to correct for this because we will also study the trend for the AWI-CM data as well as for the ICON timeslice data. But, as we will see, this offset due to the different points in time of the comparison is rather small compared to the general deviations of the climate models compared to the ERA5 re-analysis data.

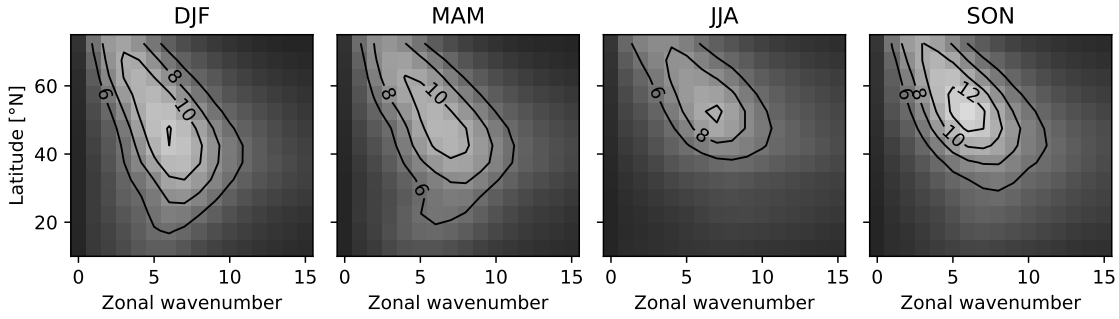

(a) ERA5 (2000–2020)

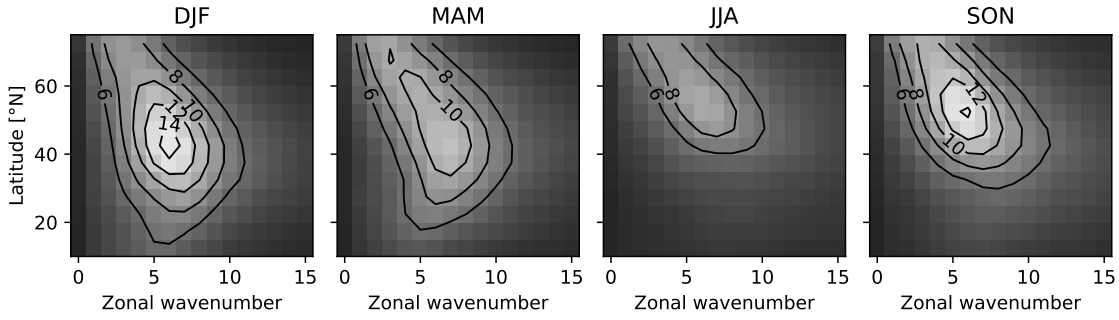

(b) AWI-CM SSP370 (2020–2030)

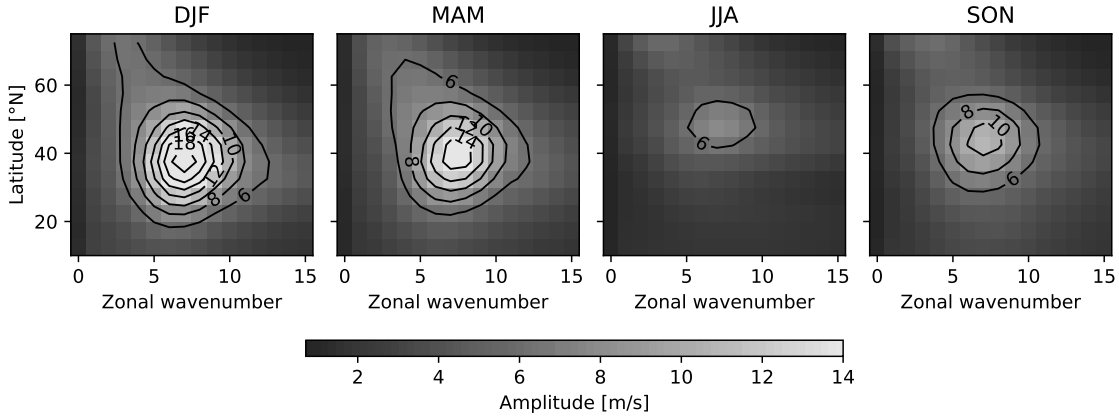

(c) ICON timeslice (baseyear 2000)

Figure 5.1: Amplitudes of zonal wavenumber decomposition of the transient part with a 21-day highpass filter of the meridional wind at 250 hPa for the North Atlantic and European sector (90°W–60°E). Subplot (a) shows the result for the ERA5 data averaged from 2000 to 2020, subplot (b) for AWI-CM with SSP370 scenario averaged from 2020 to 2030, and (c) for ICON timeslice for baseyear 2000.

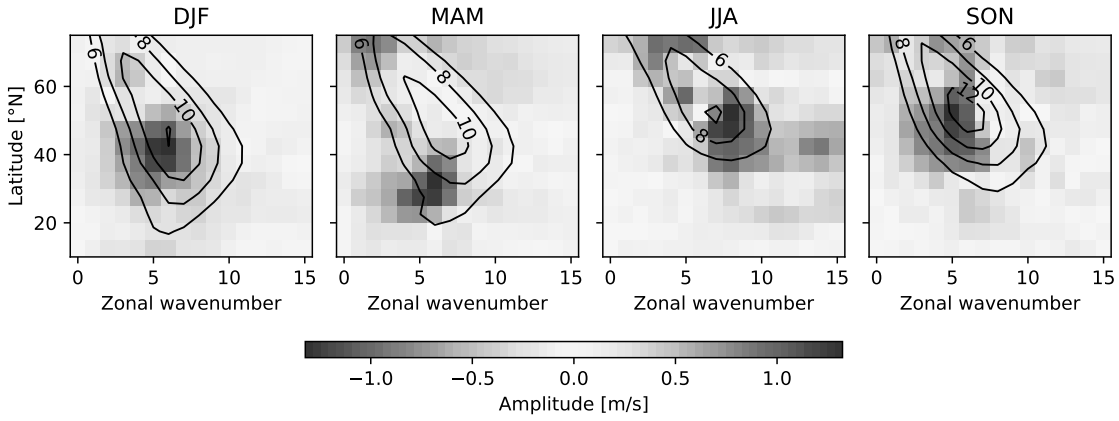

(a) AWI-CM SSP370 (2020–2030) – ERA5 (2000–2020)

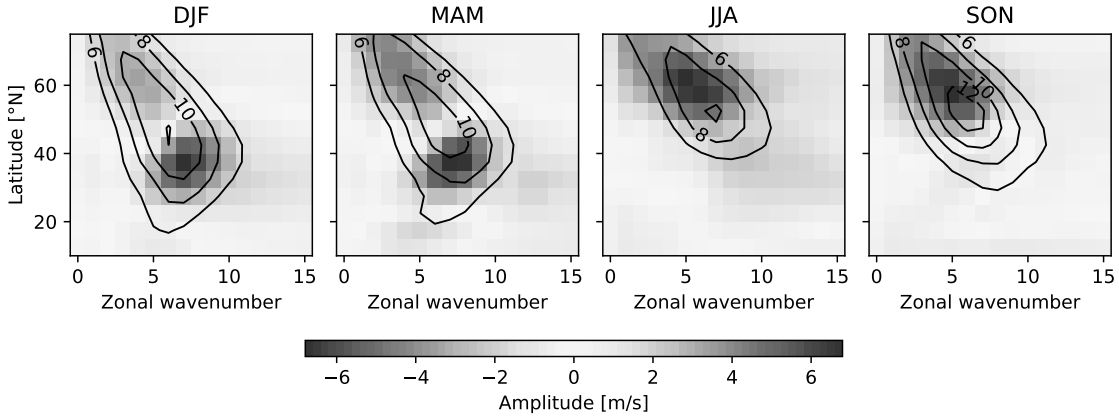

(b) ICON timeslice (2000) – ERA5 (2000–2020)

Figure 5.2: Difference in amplitudes of zonal wavenumber decomposition of the transient part with a 21-day highpass filter of the meridional wind at 250 hPa for the North Atlantic and European sector (90°W–60°E). Subplot (a) shows the delta of AWI-CM (2020–2030) and (b) of ICON timeslice (2000) both with respect to ERA5 (2000-2020).

of the different point in time for the comparison is expected to be small compared to the general deviations.

Looking more into detail, we can see, that, all in all, the AWI-CM is able to reproduce the basic structures reasonably well with a maximum amplitude at the mid-latitudes and a smooth decrease in amplitude towards higher latitudes and smaller wavenumbers. However, there are slight differences: In winter, there is an overestimation of the amplitude in mid-latitudes at the maximum (by about 10%) with a tendency to pronounce the lower wavenumbers a bit more. While at higher latitudes there is a tiny underestimation for the strong wavenumbers. For spring, the most relevant wavenumbers are modeled quite well, but there is an overestimation at lower latitudes and smaller wavenumbers. For winter, we can see a clear dipole structure, i.e. the maximum is shifted towards higher latitudes and smaller wavenumbers compared to the reference. That also leads to a less distinct maximum at mid-latitudes, but more to a smooth decrease towards higher latitudes. In autumn, again, there's a tendency to overestimate the smaller wavenumbers near the maximum.

In the end, we are going to look at the trends, i.e., the possible changes, within the same climate model. So, as long as the important characteristics are modeled reasonably well, these comparably

smaller deviations should not have a too large impact on the overall conclusion, although they should not be forgotten.

Looking at the amplitudes for the ICON timeslice experiments we see larger differences. In general, for all seasons, the maximum seems to be too strongly concentrated at the mid-latitudes, i.e., the amplitudes of the waves at higher latitudes are highly underestimated. This is especially strong for summer and autumn, where we can find differences of up to $-6\,\mathrm{m/s}$ in the latitude region of 50–70°N. This leads to an underestimation of the wave activity of more than 50% in some parts of the spectrum. In winter and spring, this effect is very similar but slightly less strong. But in these seasons, we can find a significant overestimation of the amplitude of the waves at mid-latitudes (25°–50°N) and at mid- to higher wavenumbers (also in the range of up to $6\,\mathrm{m/s}$, i.e., round about 50% overestimation). This means that in the ICON timeslice simulations, stronger waves at higher latitudes are massively underrepresented, while the wave activity at mid-latitudes is overestimated and also slightly shifted to higher latitudes. Therefore, we have to be very careful with interpreting the results from the ICON timeslice experiments because the large-scale circulation cannot be considered independent for different latitudes. A significant underestimation of wave activity at higher latitudes will also impact the mean flow and the wave activity at mid-latitudes.

These findings are also supported when looking at the standard deviations of the amplitudes for the different wavenumbers and latitudes which is shown in the supplementary chapter (see Figure 8.10) where the AWI-CM shows overall very good agreement to ERA5 while the ICON timeslice simulations exhibit larger deviations, again over-representing the mid-latitudes and underestimating the higher latitudes.

Figure 5.3 shows the distribution for the phase speed and compares it to the ERA5 reference. Here, we can see a very similar overall picture: The AWI-CM data seems to be in very good agreement with the reference. The only exception is some small areas at very low wavenumbers 1–2, but that is all at regions where the overall amplitude is very low, so this is not expected to be relevant for our studies.

On the other hand, the ICON timeslice experiments again show a much too strong emphasis on higher phase speeds at mid-latitudes while neglecting the higher latitudes. So, we have to be very cautious when interpreting the results with ICON timeslice data.

I extensively looked at the basic fields in the ICON timeslice experiments to get a better understanding of the cause for these major deviations in the wave spectrum. The zonal and temporal means of the basic fields (temperature, zonal wind, meridional wind, geopotential height) were in good agreement with the reanalysis data. Therefore, this issue must be very specific to the wave activity and the wave propagation on a daily level and was beyond my understanding of the internals of this specific climate model. So, unfortunately, I was not able to find or explain the root cause of the deviations.

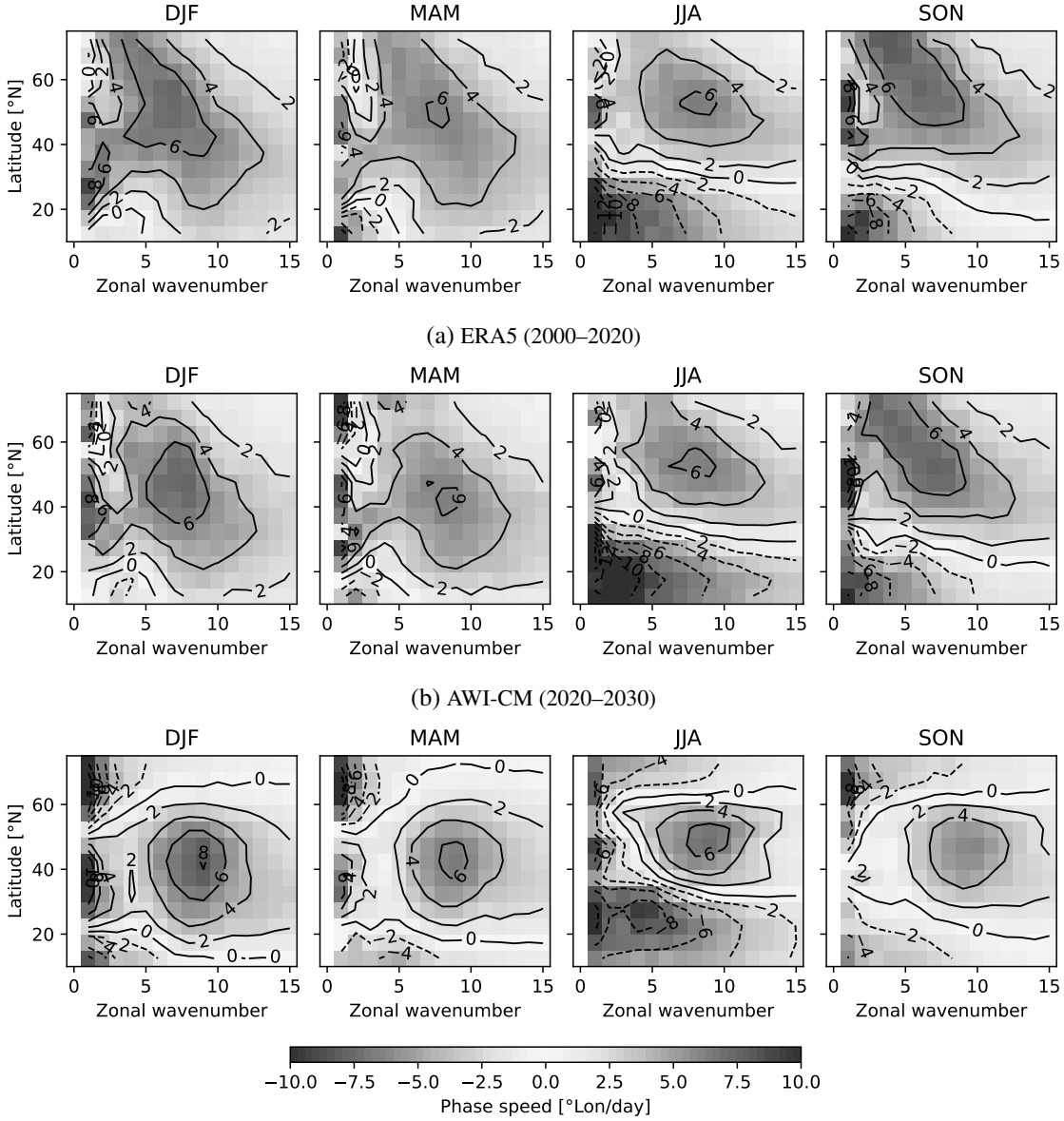

(a) ERA5 (2000–2020)

(b) AWI-CM (2020–2030)

(c) ICON timeslice (baseyear 2000)

Figure 5.3: Phase speeds in zonal wavenumber decomposition of the transient part with a 21-day highpass filter of the meridional wind at 250 hPa. Subplot (a) shows the result for the ERA5 data averaged from 2000 to 2020, subplot (b) for AWI-CM with SSP370 scenario averaged from 2020 to 2030 and (c) for ICON timeslice for baseyear 2000.

5.2 Trends in climate model scenarios

5.2.1 AWI-CM

Using the AWI-CM data, we can fit a linear regression over the whole period, i.e., 2020–2100. The results are shown in Figure 5.4 for SSP585 and in Figure 5.5 for the lower emission scenario SSP370, respectively.

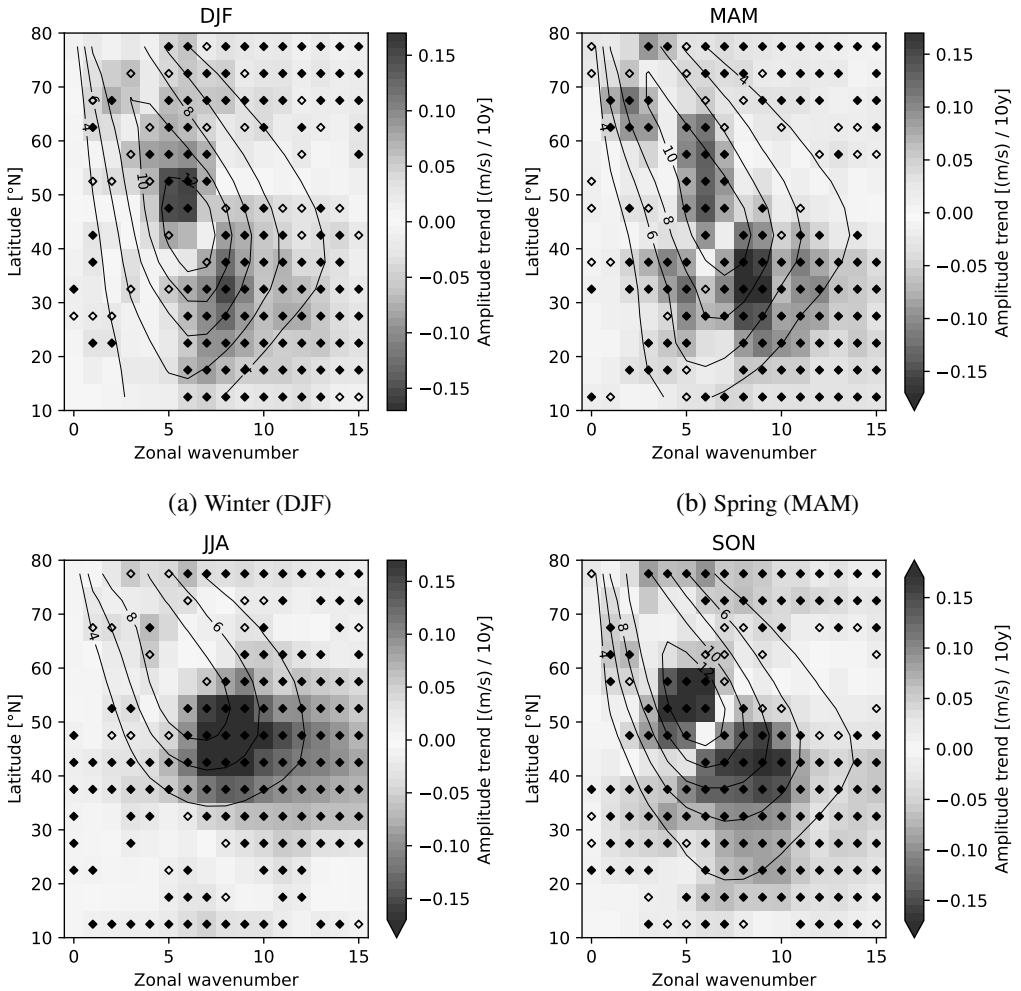

(a) Winter (DJF)

(b) Spring (MAM)

(c) Summer (JJA)

(d) Autumn (SON)

Figure 5.4: Linear trend of the amplitudes of zonal wavenumber decomposition of the meridional wind at 250 hPa (transient part with a 21-day highpass filter) for the SSP585 scenario with the AWI-CM. The values represent the linear regression slope from 2020 to 2100 and for the North Atlantic and European sector (90°W—60°E). The open/closed diamond symbols mark areas where the linear trend is significant at the 95 %/99 % confidence level. Superimposed are the contour lines of the mean amplitude as reference.

What is really interesting here, is that the two emission scenarios partly yield different results, even in the sign of the trends. Even though, looking more at the overall pattern, they show similarities in a shift towards higher latitudes and smaller wavenumbers. The underlying difference between the two scenarios is mostly the strength of global warming, i.e. the rate of warming and the total warming until the year 2100. This implies that the changes in the atmosphere's circulation are

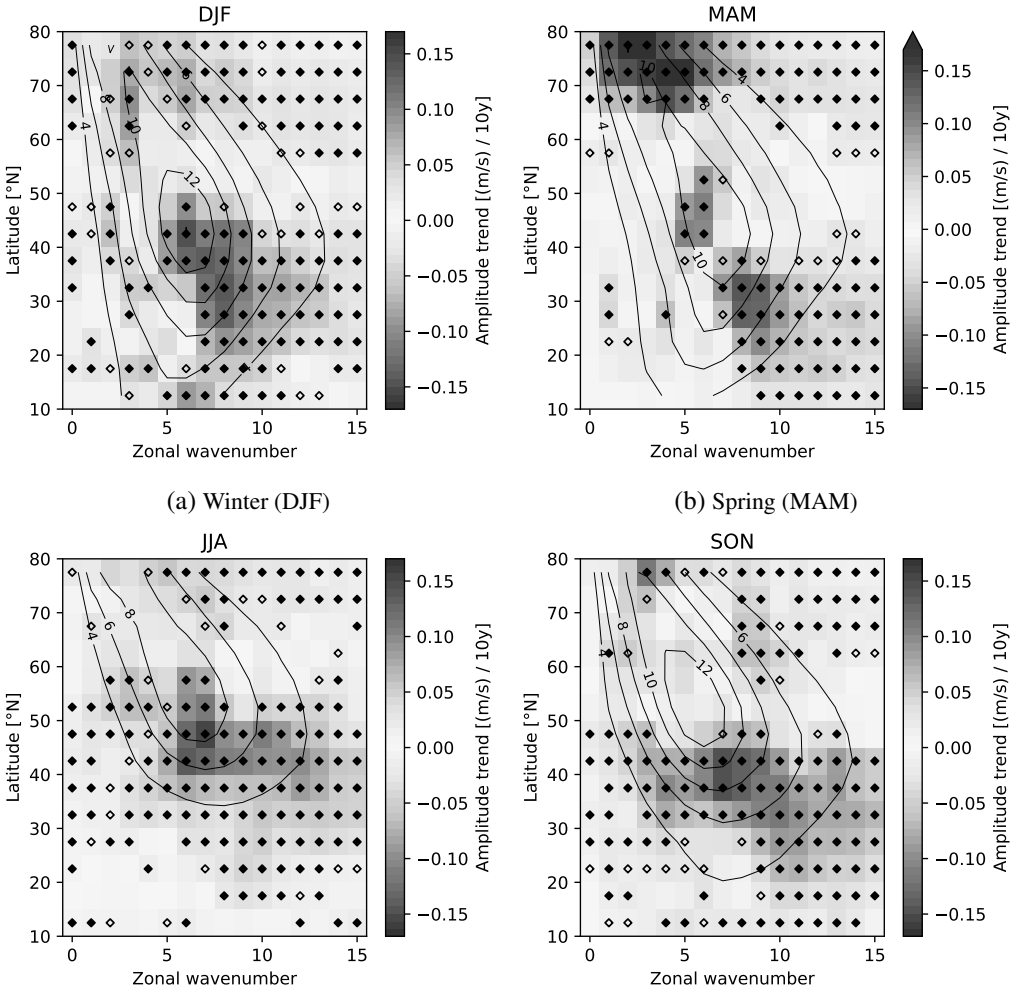

(a) Winter (DJF)

(b) Spring (MAM)

(c) Summer (JJA)

(d) Autumn (SON)

Figure 5.5: Same as in Figure 5.4 but with SSP370 scenario instead of SSP585.

partly sensitive to the rate and total amount of warming, which is an interesting finding that should be considered for further analyses.

The SSP585 scenario sees significant increases in wave activity near the maximum but towards higher latitudes and smaller wavenumbers in winter, spring, and autumn. This can only be observed for spring (and to a smaller amount and in a smaller region) for the SSP370 scenario.

What both scenarios have in common is a significant decrease in wave activity towards lower latitudes and higher wavenumbers (with respect to the seasonal maxima) for all seasons. This is the strongest and most widespread in summer, where this can be observed at nearly all wavenumbers at latitudes <55°N; for SSP585 even at higher latitudes at higher wavenumbers. That implies a general decrease in wave activity at mid- to low latitudes. Also, an increase at very high latitudes and comparatively high wavenumbers can be observed in all seasons and in both scenarios, but this is mostly in a region where the overall wave activity is quite low.

For winter, in addition, there is an increase at higher latitudes and lower wavenumbers for the SSP585 scenario. This dipole structure means a shift of the maximum wave activity towards higher

latitudes and slightly smaller wavenumbers over time, but this is absent in the trend of the SSP370 scenario. There, only at very high latitudes approx. >65°N a small increase can be seen. Hence, the reduction in wave activity at lower latitudes seems to be robust, but the dislocation feature is not among the two emission scenarios. Quite similar is the situation for autumn, where we can see a dipole structure with SSP585, but not (or at least not significant) with SSP370, while the decrease at lower latitudes exists with both scenarios.

Only for spring, can we observe this dipole structure in both scenarios, even though it is much weaker with SSP370. So, there, the shift in wave activity towards higher latitudes and lower wavenumbers seems to be robust. Contrary to the strong increase at very high latitudes (>65°N) that is only visible in SSP370.

We also looked more into the details for the wavenumber-latitude combinations with the most pronounced trends, i.e. into the time-evolution of the trends and into the sensitivity of the trends to variations in start and end years of the linear regression (similarly to what was done for the reanalysis data and is shown in Section 8.3). Due to brevity, it is not shown here. However, the trends appear to be mostly linear within the full period and seem to converge, at least towards longer time windows used for the regression calculation. So, it can be assumed that the results shown here, using the 80-year period from 2020 to 2100, are quite robust, at least where they are marked significant.

Looking at the trend in phase speed (Figure 5.6), for winter and autumn a positive trend in phase speed is visible around the peak of wave activity and towards lower wavenumbers in a broad region of latitudes. This is significant (>99% C.L.) and seems to be systematic.

For spring, only at lower latitudes and at a region towards smaller wavenumbers around the maximum wave activity a significant increase in phase speed can be seen, but the trend for the region with maximum wave activity is not clear.

For summer, it looks like there is an increase in phase speed around the region of maximum wave activity, but this is only partly significant.

We also looked at the trend of the number of days with slow-moving (i.e. <2°lon/day) waves which complements and confirms the findings. It also shows that a reduction in mean phase velocity is directly connected with an increase in days with slow-moving waves. We omitted the plots here because it doesn't help to gain new insights, and in general, the trend there is slightly less significant.

Except for spring, this hints towards a general increase in phase speed for the waves with maximum wave activity and a decrease in slow-moving waves there. This points in the direction of a reduction of blockings in the mid-latitudes, even though the trend in amplitudes is partly contradicting and makes this result vague.

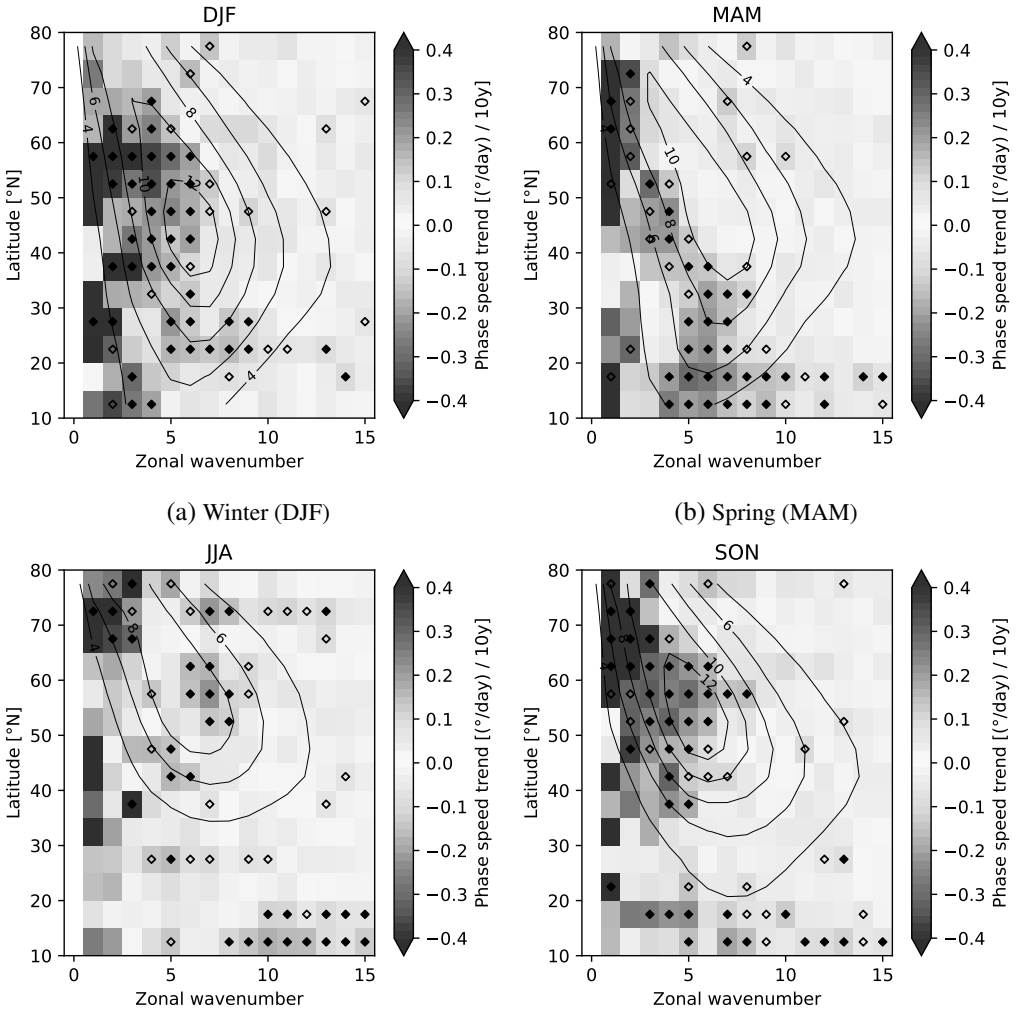

(a) Winter (DJF)

(b) Spring (MAM)

(c) Summer (JJA)

(d) Autumn (SON)

Figure 5.6: Change in phase speed of zonal wavenumber decomposition of the transient part (with a 21-day highpass filter) of the meridional wind at 250 hPa for ERA5 in the SSP585 scenario. The values represent the slope of the linear regression from 2020 to 2100 and for the North Atlantic and European sector (90°W—-60°E). The open/closed diamond symbols mark areas where the linear trend is significant at the 95 %/99 % confidence level. Superimposed are the contour lines of the amplitude as reference.

5.2.2 ICON timeslice

We also looked into the linear regression trend for ICON timeslice data. The significance is also shown in the plots, but the timeslice data has too little variability because the boundary conditions are fixed without any additional year-to-year variability. Therefore, the trend appears to be overconfident and seems to be significant everywhere, but this has to be doubted strongly.

Nevertheless, the trend shows a general shift towards smaller wavenumbers for winter and, less pronounced, also in spring (see Figure 5.7) when the linear regression is calculated over the whole period, i.e. including the baseyears 2000, 2040 and 2090. The strongest changes seem to appear in the first period, i.e., from 2000 to 2040, which is shown in Figure 8.12 in the supplementary chapter.

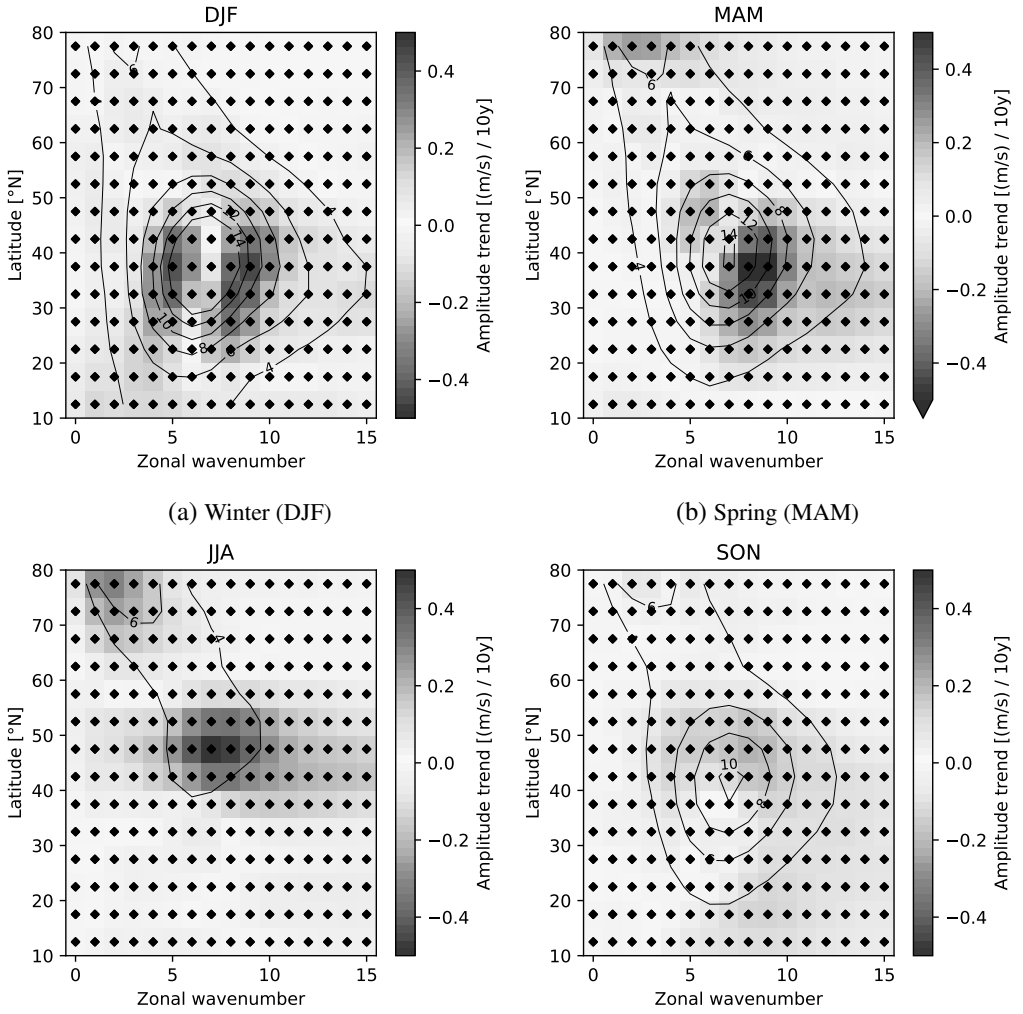

(a) Winter (DJF)

(b) Spring (MAM)

(c) Summer (JJA)

(d) Autumn (SON)

Figure 5.7: Linear trend of the amplitudes of zonal wavenumber decomposition of the meridional wind at 250 hPa (transient part with a 21-day highpass filter) and for the North Atlantic and European sector (90°W—60°E). The values represent the linear regression slope from 2000 to 2090, i.e., including the baseyears 2000, 2040, and 2090. The open/closed diamond symbols mark areas where the linear trend is significant at the 95 %/99 % confidence level. Superimposed are the contour lines of the mean amplitude.

For summer, there is a clear decrease all over the mid-latitudes (35–60°N), also mostly in the first half, i.e., from 2000 to 2040, of the overall period (2000–2090).

For autumn, there is slight overall decrease over the full period up to 2090, while in the beginning (2000 to 2040) there is a clear shift of wave activity towards lower latitudes, but at nearly the same wavenumbers.

But due to the massive underrepresented wave activity at higher latitudes all this has to be interpreted really carefully and doesn't appear to be very robust and clear. On the other hand, considering only the part of the spectrum at latitudes <50°N it shows similar patterns to the AWI-CM, except for autumn. I.e., for winter, we see a shift towards lower wavenumbers, but here, the shift to higher latitudes is missing. For spring we can see a shift towards higher latitudes and lower wavenumbers,

and in summer a general decrease in wave activity. The results for autumn are not conclusive but show signs of a slight overall decrease in wave activity.

For the phase velocity in Figure 5.8 there is no clear overall trend. But for winter it looks mostly like an increase at smaller and a decrease at higher wavenumbers (transition at around wavenumber >8). The picture for Spring is not quite clear, but there could be an increase at higher latitudes from the maximum (especially at lower wavenumbers) and a reduction at lower latitudes, which is broken by areas with opposite signs. In summer, phase speed decreases everywhere north from 35°N regardless of the wavenumber, including a clear decrease for waves with the highest amplitude. Again, the situation for autumn is less clear, but the most active waves seem to exhibit an increase in phase speed in the mid-latitudes and decrease further to the north (around latitudes >55°N). Again, we also looked at the trend from 2000 to 2040 separately (not shown), and we can observe the same behavior as before, i.e., most of the changes happen between 2000 and 2040 and less between 2040 and 2090. The overall pattern looks very similar to the overall trend shown above. Comparing this to AWI-CM it doesn't show any similarities, except maybe for winter with a tendency of increase towards lower wavenumbers and decrease towards higher.

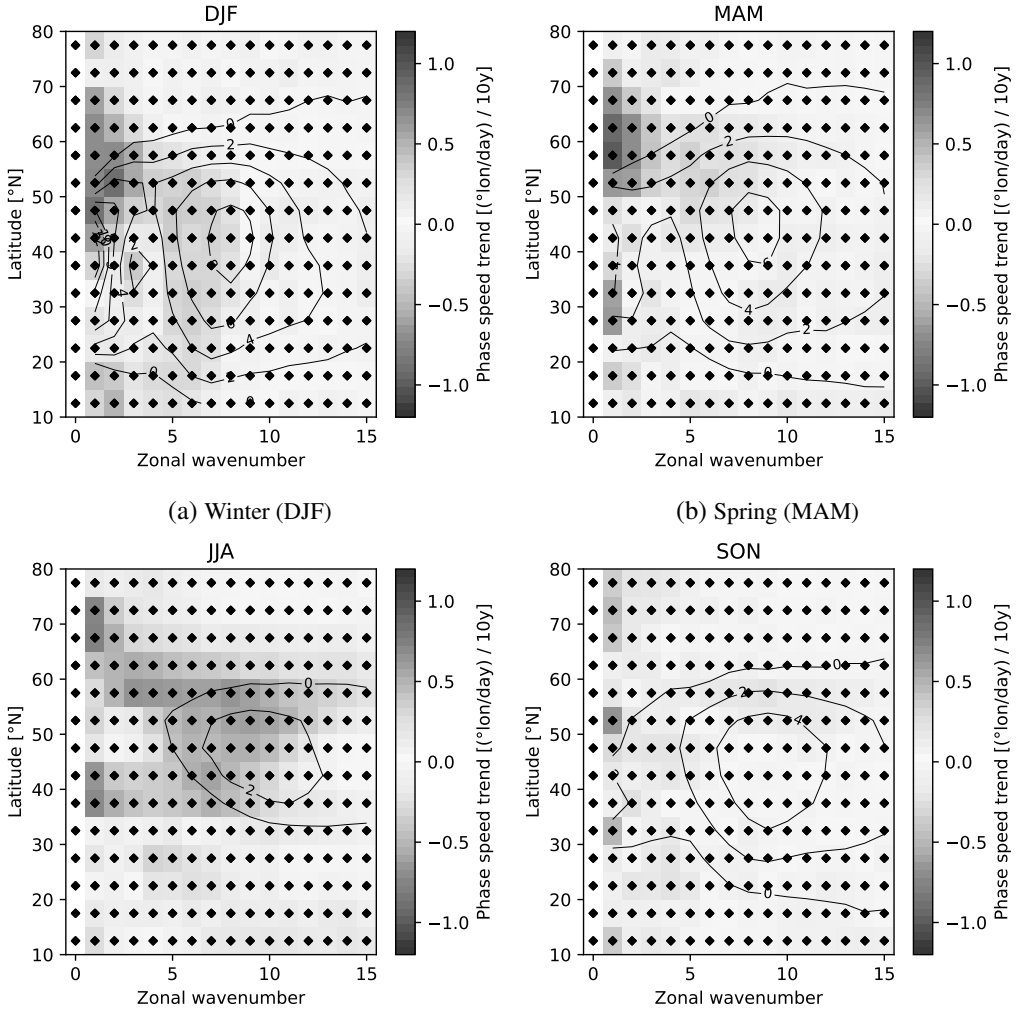

(a) Winter (DJF)

(b) Spring (MAM)

(c) Summer (JJA)

(d) Autumn (SON)

Figure 5.8: Change in phase speed of zonal wavenumber decomposition of the transient part (with a 21-day highpass filter) of the meridional wind at 250 hPa and for the North Atlantic and European sector (90°W—60°E). The change is via a linear regression, including the baseyears 2000, 2040, and 2090. The open/closed diamond symbols mark areas where the linear trend is significant at the 95 %/99 % confidence level. Superimposed are the contour lines of the mean phase speed as reference.

5.3 Conclusion

Overall, the AWI-CM effectively simulates the most relevant characteristics of the Rossby wave spectrum and shows good agreement with reanalysis data, despite some minor biases. This indicates that the AWI-CM is generally suitable for studying signatures in the Rossby wave spectrum, particularly for trend analysis where relative tendencies are more critical than absolute values.

In contrast, the ICON timeslice model exhibits significant discrepancies compared to the reanalysis data. Its Rossby wave activity is overly confined to the mid-latitudes, with substantial underrepresented wave activity north of 50°N. Additionally, wave activity in the mid-latitudes during winter and spring is significantly overestimated, while it is considerably underestimated in summer and autumn. A further limitation of the ICON timeslice experiments is the use of fixed boundary conditions without year-to-year variation, resulting in insufficient variance over the 30-year statistics for each baseyear, which undermines its utility for significance calculations.

Regarding the future trends, simulations with the AWI-CM consistently indicate a decrease in wave activity at lower latitudes and higher wavenumbers. Under the SSP585 scenario, there is a notable shift of maximum wave activity towards higher latitudes and smaller wavenumbers across all seasons, along with a general decrease in maximum wave activity during summer. This is similar in the SSP370 scenario, where we also observe this shift to higher latitudes for all seasons, but here we find an overall decrease in wave activity not only during summer, but also in winter (and to some extent in autumn). The trend in phase speed is less clear, but there is a general tendency towards increased phase speed in the regions of maximum wave activity, except during spring (where most of the increase is shifted towards smaller wavenumbers).

These changes are expected to be connected to a shift of blocking events towards higher latitudes for all seasons. In summer, and to a lesser extent in winter and autumn (here mostly due to changes in phase speeds), this also implies a reduction in blocking frequency. For spring, the implications on the frequency of blockings are less clear—unlike the latitudinal shift.

The results from the ICON timeslice experiments partially align with these findings, but their overall reliability remains uncertain due to the model's limitations.

6 Extreme temperature events, blockings and Rossby wave activity

In this chapter, we will first examine correlations between temperature and geopotential height, then investigate extreme temperature events and their relation to geopotential height anomalies. We conclude this first part with the statistical relationship between blockings and temperature anomalies. The next part aims to identify distinct differences in the Rossby wave spectrum during blockings compared to the mean spectrum. The last part will study some examples of recent historical heatwaves, focusing on the wave spectrum. This all helps to better understand which signatures in the wave spectrum are linked to blockings and extreme events and how they are connected.

6.1 Spatial patterns and correlations in context of extreme events

6.1.1 Correlation of temperature and geopotential height

It is interesting to check how well the theory about blocking and temperature extremes explained in Section 2.6 matches the reality for central Europe. For this, we look at the detrended 850 hPa temperature anomalies[1] and the detrended 500 hPa geopotential height anomalies.

The first question is how strongly the temperature and geopotential height anomalies correlate. The spatial correlation is of special interest and therefore, the areal average of the temperature anomaly for a sector from 45°–55°N in latitude and 5°–15° in longitude was used, which covers roughly the region of Germany. Then, the Pearson's correlation coefficient for each grid cell in NAE sector was calculated by using the detrended geopotential height anomaly of the specific grid cell and the areal average temperature anomaly.

The result is shown in Figure 6.1 (a). The highest positive correlation is over Austria, i.e., close to the southeast corner of the area over which the temperature was averaged, with very high correlation coefficients (Pearson correlation coefficient of over 0.8). The high positive correlation, which is

[1] We are looking at the 850 hPa temperature because this gives a more direct picture of the atmospheric state. The 2 m temperature, in contrast, is strongly affected by the ocean temperature and the soil moisture over the continents, respectively. In addition, it shows a time lag. However, for comparison, we have also done the same analysis with the 2 m temperature that can be found in the supporting material.

(a) All year

(b) Only winter (DJF)

(c) Only summer (JJA)

Figure 6.1: Spatial correlation between geopotential height anomaly and temperature anomaly at 850 hPa (mean over 45–55°N and 5–15°E) for the years 1940 till 2022. All anomalies are detrended before calculating the correlation. Subfigure (b) and (c) are filtered so they only include data from the specific season.

very close to the center of the mean temperature calculation, shows a clear connection between geopotential height anomaly and temperature anomalies, as expected.

When we do the same analysis, but for the seasons separately and for the summer, we only consider positive temperature anomalies, while for winter, we only consider negative temperature anomalies, there is only a slight shift in the location of the maximum correlation. This is shown in Figure 6.1 (b) and (c). This is also expected because the geopotential height anomaly will be co-located with positive temperature anomalies in the summer. Interestingly, there is also a negative correlation both to the east and to the west, which looks like the signature of Omega blockings. So, this already suggests a connection between blockings and positive temperature anomalies.

The situation is a bit more difficult for the winter and negative temperature anomalies because of different effects. For winter, we would also expect both anomalies to be more or less co-located because negative temperature anomalies should correlate with negative geopotential height anomalies (i.e., a trough over the region with colder temperatures).[2] But there should also be some impacts by ridges northwest (i.e., positive geopotential height anomalies) to the region with negative temperature anomalies because of cold air advection into the region of interest. This would imply a negative correlation to the northwest that, indeed, can be seen in the figure. But this, so far,

[2] One should note that this shows up as a *positive* correlation in the plot because the negative geopotential height anomaly and negative temperature anomaly have the same sign.

only shows the daily correlations without the requirement of persistence or extreme values in the temperature or pressure anomalies.

6.1.2 Heatwaves/cold spells and geopotential height anomalies

To study extreme temperature events, and not only the general correlation of temperature, we now only look into persistent extreme events, where for the summer (winter), we require the temperature anomaly to be above 95%-percentile (below the 5%-percentile) for at least 5 consecutive days. We call that a heatwave (cold spell). Now, we select all the days that pass the criterion for the same area as described above, i.e., from 45°–55°N in latitude and 5°–15° in longitude, and look at the mean geopotential height anomaly for these days, once for winter and once for summer.

The result is shown in Figure 6.2 and shows the expected behavior as explained in Section 2.6.

(a) Cold spells in winter (b) Heat waves in summer

Figure 6.2: Mean geopotential anomaly for cold spells (heat waves) in the area over 45–55°N and 5–15°E. Cold spells (heat waves) are defined in the areal mean temperature anomaly at 850 hPa to be below the 5% (95%) level for at least 5 consecutive days. The ERA5 data from 1940 to 2022 was used. All anomalies are detrended.

For the winter, persistent cold extremes are connected to a positive geopotential height anomaly to the northwest of the cold area. In contrast, negative geopotential height anomalies are co-located with the cold area. For summer, we can see there is a positive anomaly directly above the area affected by the heatwaves and the negative anomalies around it, which is compatible with typical blocking situations. This shows that the above-mentioned relationship also holds for persistent temperature extremes and can be seen clearly in the geopotential height field. So, there is a clear relationship between persistent temperature extremes and patterns visible in the geopotential height field that mimic blockings.

We also looked into the same correlation but using the 2 m temperature instead of the temperature at 850 hPa, but apart from effects which are due to the difference in land and sea temperature (i.e., in general, the correlation patterns are much stronger over land, because of the difference in heat capacity), in general, the same patterns are visible. Therefore, we didn't include the plots here.

6.1.3 Blockings and temperature anomalies

To finally look at blocking situations, we use the absolute method for blocking definition as described in Chapter 3.2.3, where we require the blocking to persist at least 5 consecutive days with an areal overlap that is above the threshold of 500 000 km². The fifth day is then defined as the first day of the blocking.

In that way, we select all days with persistent blockings in a region that covers most of Europe (40°–70°N and 20°W–40°E)[3] and then look at the mean temperature anomaly at the 2 m temperature.[4] Since the blocking onset is then 4 days before the first selected day, we're using a centered rolling average for the temperature anomaly, which includes 2 days before and after the selected blocking day, because we expect the 2 m temperature to be somewhat laggy and slowly build up compared to the atmospheric state. The result for the different seasons is shown in Figure 6.3. Overlayed (contour lines) is the total number of days with blockings each season. It can be seen that in the different seasons, the preferred blocking locations as well as the blocking frequency differ.

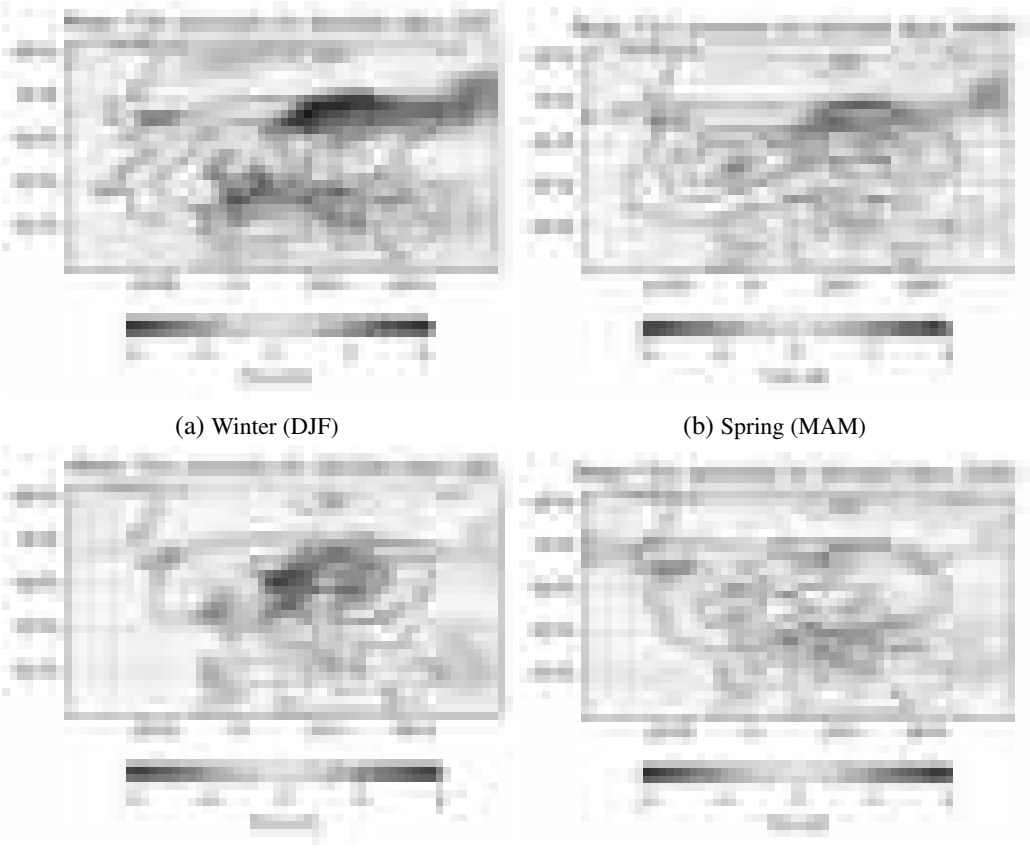

(a) Winter (DJF)

(b) Spring (MAM)

(c) Summer (JJA)

(d) Autumn (SON)

Figure 6.3: Mean 2 m temperature anomaly for days with blockings in the European region (40°–70°N and 20°W–40°E). The blockings are required to persist for at least 5 consecutive days, and the blocked area needs to be at least 500 000 km². All anomalies are detrended before calculating the correlation. The contour lines mark the total number of blocked days in that season over the whole time period.

[3] Due to the used blocking algorithm, it is not possible to identify any blockings at lower latitudes than 40°N.

[4] Now, we use the 2 m temperature instead of the 850 hPa temperature because this is more relevant for the impacts.

While in winter, most of the blockings occur over North Eastern Europe, with a maximum over the British Isles, in summer, there are much fewer blocking days, and the preferred region is more to the East, i.e., in Northern Europe, with a maximum over Norway, Sweden, and Finland. Spring and autumn, as transitional seasons, show both the features of summer and winter and look very similar to an overlay of summer and winter. In contrast, autumn looks more similar to winter but with much less frequent blockings. Looking at the temperature anomaly we can identify the expected patterns, very similar to what was discussed before:

For winter, the region to the southeast of the main blocked regions shows a strong negative temperature anomaly due to the cold air advection from the north(east), while the region north of the blocking shows a clear positive trend due to warm air advection.

For summer, the regions with the highest counts of blocked days show the highest positive temperature anomalies, so right below the blockings. South of the blocked regions a slight negative temperature anomaly is identifiable, which could be due to the impact of the cut-off low often find south of the blocked region for a dipole or Rex block.

Spring looks like a mixture of summer and winter, while autumn looks a bit more similar to the situation in winter but less strongly pronounced. This might be due to, in general, less strong temperature contrasts compared to winter and less strong radiative heating by the sun compared to summer.

6.2 Rossby waves during blockings

We've already seen in the previous sections that there is a clear connection between blockings on one side and temperature extremes on the other. Now, it is also of interest whether there are specific patterns in the large-scale dynamics during periods where there is a blocking situation over the European sector, i.e., we are trying to find an answer to the question of whether situations that led to and sustained blockings can be identified in the wave spectrum. This would ultimately allow us to link Rossby wave activity to extreme temperature events.

Therefore, we first identify all (persistent) blockings in a region extending from 40°–70°N[5] and 20°W–40°E. The blocking algorithms used here, the so-called absolute method and anomaly-based method, have already been described in detail in Chapter 3. Here, a blocking is detected if it persists for at least 5 consecutive days, and the areal overlap during these 5 days is at least 500 000 km². For this analysis, we consider all consecutive blocked days as blocking as long as the 5-day threshold is met, i.e., from the first day on, because we are also interested in the large-scale dynamics that lead

[5] Be reminded that the absolute method cannot be applied for latitudes lower than 40°N, which limits the applicable latitudinal range. But this is not a big issue because nearly all blockings are at higher latitudes. In principle, the anomaly-based method could also be applied at lower latitudes, but due to the shift in ITCZ, especially in the summer and autumn, it wouldn't be very reliable at these low latitudes anyway.

to and sustain the blocking, and not so much in the impacts of the blocks at the surface temperatures which take time to build up over several days.[6]

For the wave spectra, we will limit our analysis to the NAE sector, i.e., extending from 90°W–60°E in longitude, and will apply the exact same methods of zonal wavenumber decomposition as in the previous chapters for this sector, so that it is comparable. The only difference is, that we do this once only for the days where we identified a blocking according to the definition above. Then, we subtract the seasonal mean without any requirements, which yields the difference that will be used here.

The results for the difference in amplitude in the wave spectrum are shown in Figure 6.4 when using the absolute method for blocking detection. For significance calculation, a t-test was performed to mark areas where the difference is significant beyond a certain confidence level (95% and 99%). It can be seen that during blockings, there are significantly lower amplitudes at mid-latitudes, where, in the seasonal mean, the maximum amplitude is found. In addition, there is a significantly increased amplitude towards higher latitudes and lower wavenumber.

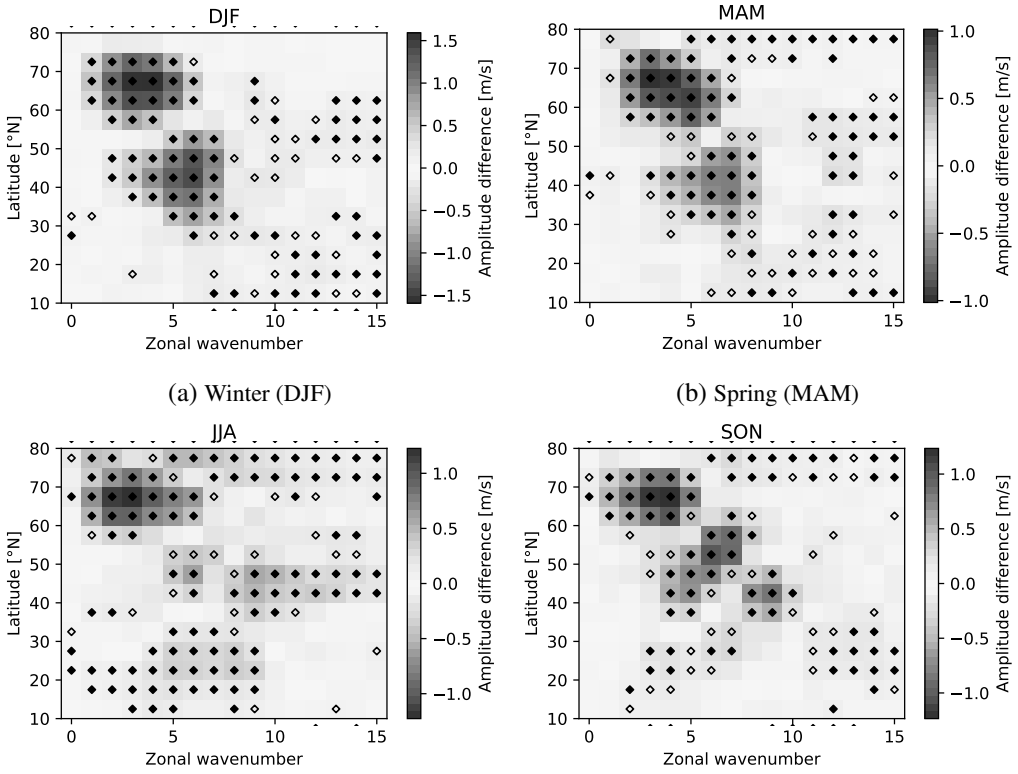

(a) Winter (DJF)

(b) Spring (MAM)

(c) Summer (JJA)

(d) Autumn (SON)

Figure 6.4: These plots show the difference in amplitude when comparing only days with blocking over Europe to the mean in that particular season. The absolute method was used for blocking detection and covered the region 40–70°N and 20°W–40°E. The open/closed diamond symbols mark areas where the difference is significant at the 95 %/99 % confidence level.

For winter, this separation is at about 55°N, where north of it there is an increase in wave activity and south a decrease (at least at the most dominant wavenumbers), which is at the latitude where,

[6] This is why we used a different time selection when we were studying the relationship between blockings and temperature extremes where we excluded the first days of the blocking.

on average, most of the blocking can be observed during winter. This can be seen when looking at the contour lines of Figure 6.3 (a) which marks the counts of blocked days in that season. Also, there is a very slight but significant increase at mid-latitudes and comparable high wavenumbers (around greater equal wavenumber 9-10). The situation with the dipole structure is quite similar for spring. So, for winter and spring, we see a significant increase in wave activity poleward of the most blocked latitudes and a decrease to the south, but no clear difference at the most blocked latitudes, which is compatible with a poleward-shifted jet stream during the blockings.

The picture is a bit more complicated for summer and autumn because there is also an increase in amplitude towards mid- to low latitudes and at higher wavenumbers visible. The blocking also occurs during those seasons, usually a bit further north.

For summer, the most blocked latitudes are around 60-65°N (see Figure 6.3 (c)), and there is a significant increase in wave activity already at the latitudes that are most often blocked and north of it. Only further south (around 55°N), where nearly no blockings occur anymore, there is a decrease in wave activity at wavenumbers 5–7 visible. Interestingly, at 35–50°N, there is an increase in wave activity at higher wavenumbers, i.e., ≥ 8. Also, at low latitudes (<35°N), wave activity increases again. But we have to be careful here, because this is partly already in the upper-level easterly winds where it's not reflecting Rossby waves along the westerly jets.

The situation for autumn is very similar to summer but even more pronounced. Here the most blocked latitudes are located around 55-65°N (see Figure 6.3 (d)), but with two slightly separated hot spots (on over the British Isles and another one over the southern part of Norway and west of it). The increase in wave activity overlaps with the location of the northern hot spot (Norway) for blockings. Further south (and tilted towards higher wavenumbers) there is a significant decrease in wave activity which conincides with the latitudes of the southern hot spot (British Isles). Further south (<50°N) and to higher wavenumbers we see an increase in wave activity again.

One possible explanation for this tripole structure in summer and autumn is a splitting of the jet stream in front of the blocking, which deviates part of the Rossby waves further south. This would hint towards more frequent Rex blockings (compared to pure Omega blocks) in summer and autumn. But it is also possible that these blockings occur mostly when the eddy-driven jet stream is more separated from the subtropical jet stream, resulting in a slower and more wavy subtropical jet stream alongside the northern, partly blocked, eddy-driven jet stream.

The same analysis has also been done using the anomaly method for blocking detection and the results are shown in the supporting material (Chapter 8) in Figure 8.3. The results are quite similar, with some smaller deviations due to different selected blockings. The biggest difference there seems to be in spring, where with the anomaly-based method, the situation is much less clear for mid- and low-latitudes (but in this region, most of the grid points are also not significant). Also, for summer, the tripole structure is not that pronounced, but here, we also see a significant increase at the most blocked latitudes. Still, the overall picture for all the seasons is the same: a significant amplitude increase towards higher latitudes and smaller wavenumbers, while at mid-latitudes and intermediate wavenumbers (approx. below 8), there is a significant decrease.

Doing the same analysis for the phase velocities instead of the amplitudes yields Figure 6.5 for the absolute method (and Figure 8.4 for the anomaly method, respectively). Here, a quite similar pattern emerges: at higher latitudes and lower wavenumbers, the phase speed increases, while in the mid-latitudes, the phase speed is in a wide range of wavenumbers significantly decreased, here even at higher wavenumbers. But there are subtle but noteworthy differences: in this case, the latitudes of reduced phase speed are mostly in agreement with the blocked areas, except for at the very high latitudes, but also extend further to the equator. The decrease in phase speed there is what one would expect because, during a stationary blocking, the Rossby waves have to be stationary as well, at least around the blocked area—and to some extent south of it because of flow reversal (dipole block) or deflection (Omega block).

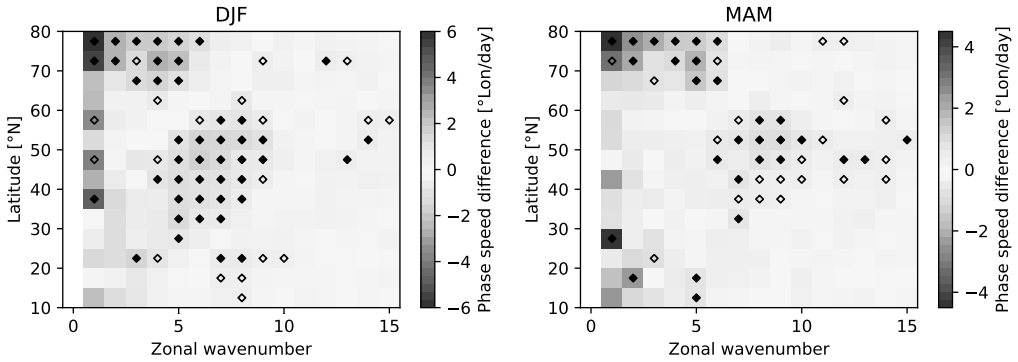

(a) Winter (DJF)

(b) Spring (MAM)

(c) Summer (JJA)

(d) Autumn (SON)

Figure 6.5: Same as Figure 6.4 but here for the differences in phase velocity instead of the amplitudes.

However, a lower average phase velocity does not necessarily imply an increase in quasi-stationary, i.e., slow-moving transient waves, even though a decrease in phase velocity and amplitudes of transient waves hints in that direction.

To check for that, we now look at the fraction days of slow-moving waves, i.e., transient waves where the magnitude of the phase velocity is below 2°lon/day. We calculate the fraction of days that fulfill this criterion for the whole season and, again, only for days with a detected blocking. Then we build the difference that is shown in Figure 6.6 for the absolute method (and in Figure 8.5 for the anomaly method).

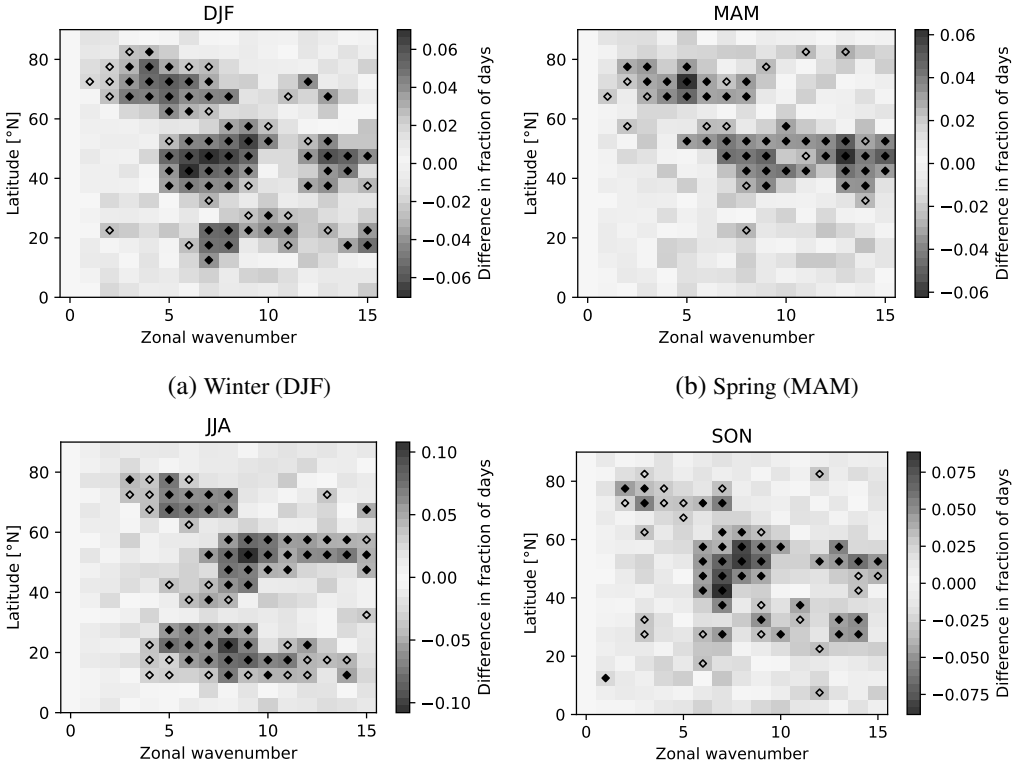

(a) Winter (DJF)

(b) Spring (MAM)

(c) Summer (JJA)

(d) Autumn (SON)

Figure 6.6: These plots show the difference in the fraction of days with slow-moving waves (i.e. < 2°lon/day) when comparing days with blocking present over Europe to all days in that particular season. The absolute method was used for blocking detection and covered the region 40–70°N and 20°W–40°E. The open/closed diamond symbols mark areas where the difference is significant at the 95 %/99 % confidence level.

Here, we can see a significant increase in the number of days with slow-moving waves compared to the seasonal average between around 35–60°N. This is expected because many of the blockings are located at those latitudes. On the other hand, there is again an increase towards the higher latitudes, i.e., from around 65°N on (for winter, even from 60°N on), even though a lot of blockings occur between 60–70°N. However, there might be some bias in the method because the absolute method of blocking detection tends to identify rather the northward edge of the blocking, which leads to the fact that the blocking statistics might be slightly offset to the north. On the other hand, we can see a similar situation when using the anomaly-based method (see Figure 8.4) which does not have such a bias. But there is another possible explanation for this: blockings need to be sustained, and that often happens by feeding energy into them via Rossby waves. So, it could make sense to see a decrease in slow-moving waves near the northern edge of the blockings that might help them to be sustained (but this explanation would have to be verified with data before making definite conclusions, which is not covered in this thesis).

We can also observe a decrease in days with slow-moving waves at very low latitudes in winter. This could be due to flow diversion towards the south for Rex-like blockings. In summer, in contrast, we can see an increase. However, in summer, this is in a region of upper-level easterly winds and south of the subtropical jet and, therefore, not of much interest in the scope of this thesis.

This picture supports what was theorized earlier and is very similar to the plots with the difference in phase speed, but one should carefully note the difference in the meaning of the sign of the value here. Here, a positive value means an increase in number of days with slow-moving waves, which corresponds to negative values, i.e. on average slower moving waves, in the plots of the phase speed difference (Figures 6.5 and 8.4).

6.3 Historical heatwaves

We will now examine some recent historical heatwaves over Europe using ERA5 reanalysis data, beginning with the most recent event: Late July 2019, late June 2019, and early August 2003. We want to specifically examine the time evolution of these events with a focus on the Rossby wave activity to see whether there are some commonalities and also compare it to the results in the previous section, which so far only showed aggregated statistics.

6.3.1 Late July heatwave 2019

As an example, we will now take a look at the evolution of the heatwave in late July 2019. This heatwave was characterized by an amplified ridge over southwestern Europe that then developed into a strong Omega block, first over central Europe and then further increasing in amplitude and covering northern Europe.

This evolution can partly be seen when looking in Figure 6.7 where the meridional wind at 250 hPa is shown at the relevant days. On the 20th of July, only weak Rossby wave activity is visible, which then increases on the following days. Up to the 23rd of July there is some eastward propagation is visible. On the 23rd, this movement becomes rather slow, and there is a stationary region of high northward meridional wind close to the British Isles and an adjacent region of high negative meridional wind over eastern Europe. In between this pattern is where the Omega block develops.

The same situation is depicted in Figure 6.8 (a) as a Hovmöller plot, where the meridional wind is averaged over a region of 45–55°N. Overlayed as a contour line is the region where the, over the same latitudinal range averaged, 850 hPa temperature anomaly is above 6 K, which marks the strongest period of the heatwave in this region.

Figure 6.8 (b) shows how this development looks like in the wave spectrum (also for the same latitudinal region, 45–55°N), i.e., looking at the amplitudes of the zonal wavenumber components. There you can see a strongly pronounced wave activity around wavenumber 7 at the time where the blocked region strongly grows and becomes stationary. At the same time, the phase velocity of these strong waves becomes slow, i.e., they are quasi-stationary, which is shown as hashed areas (i.e., areas with slow phase speed) in the figure.

So, in this case, the blocking development has a clear signature in the wave spectrum, with highly enhanced amplitudes around wavenumber 7 and slow phase velocities.

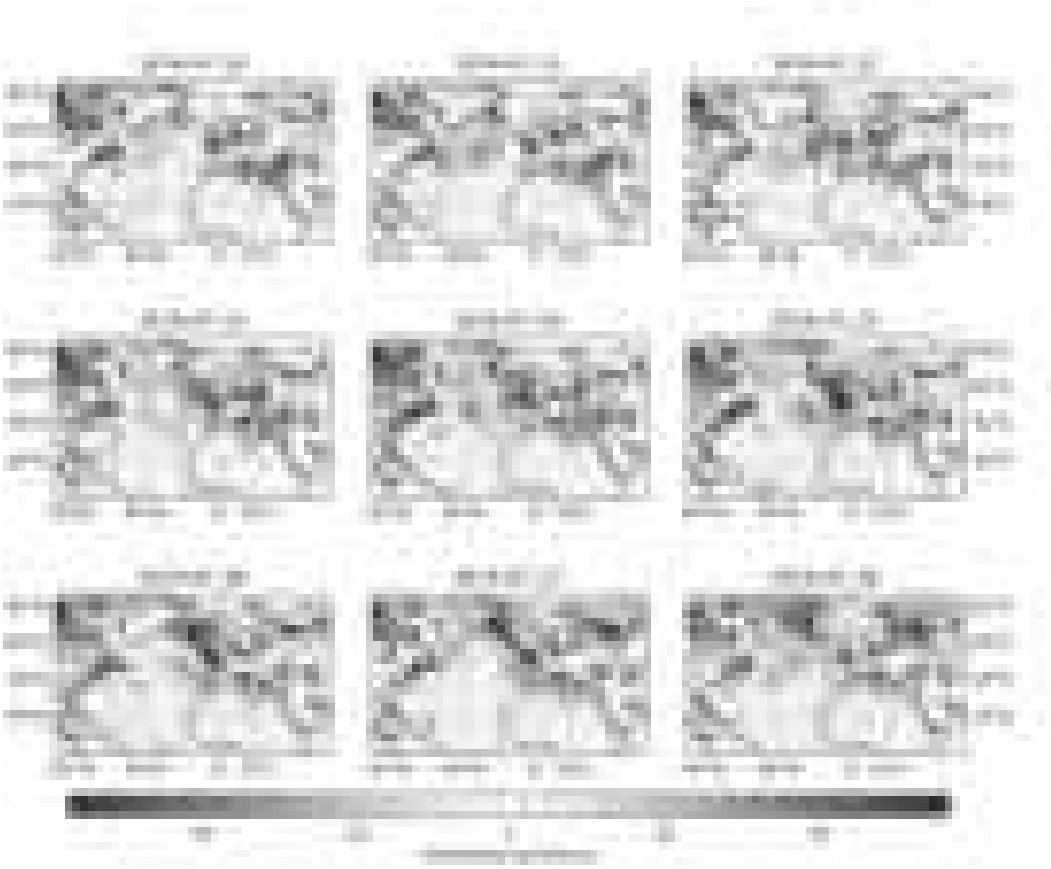

Figure 6.7: Daily evolution of the meridional wind at 250 hPa which shows the eastward propagating Rossby waves for the heatwave in late July 2019.

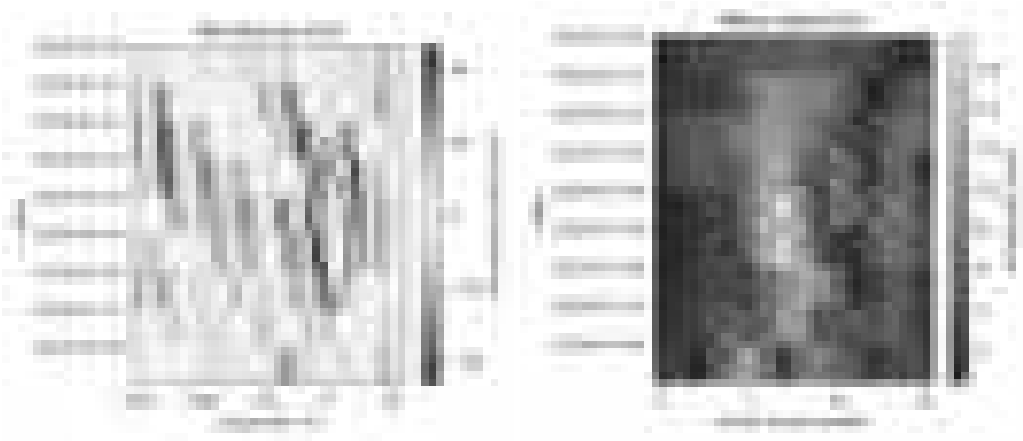

(a) Meridional wind (b) Wave spectrum

Figure 6.8: Hovmöller diagram of meridional wind at 250 hPa (a) and the corresponding amplitude spectrum (b) for the heatwave in late July 2019. The contour lines in (a) mark the region in time and longitude where the temperature anomaly at 850 hPa is above +6 K. The hashed ('x') areas in (b) show where the phase velocities are below 5°lon/day. All shown values in the diagrams are a latitudinal average over 45°N–55°N.

6.3.2 Late June heatwave 2019

Our second example is the heatwave about one month earlier, in late June 2019. There, an amplified ridge intensified via an anti-cyclonal Rossby wave-breaking event over the Atlantic Ocean, causing a cut-off low west of the Iberian peninsula. At the same time, the ridge further east, over central Europe, intensified and was locked for a while, which caused a heat wave in France and adjacent countries.

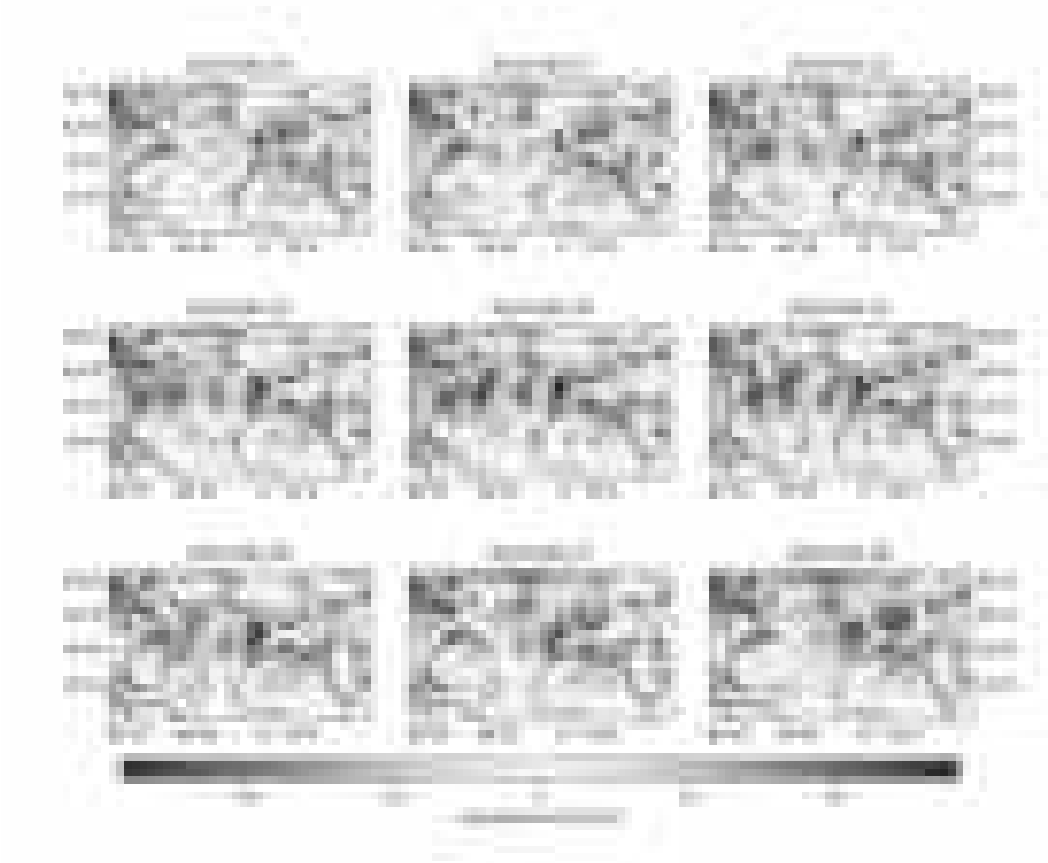

Figure 6.9: Daily evolution of the meridional wind at 250 hPa which shows the eastward propagating Rossby waves for the heatwave in late June 2019.

In Figure 6.9 this development can be followed by looking at the meridional wind maxima. In the beginning, on the 20th of June, there is only a slight wave activity. But this changes during the following days, and an intensifying Rossby wave pattern, which peaks around the 24th to 25th of June, is clearly visible. This highly amplified Rossby wave breaks, and as a result, the pattern weakens the following days. The cyclonal wave breaking is hard to see in this presentation, but on the 26th it can be recognized as a strongly tilted patch of southward wind in between Iceland and the British Isles. The cut-off can be seen on the 27th as the curved patch of high northward wind, which extends from southern Greenland to the Iberian peninsula.

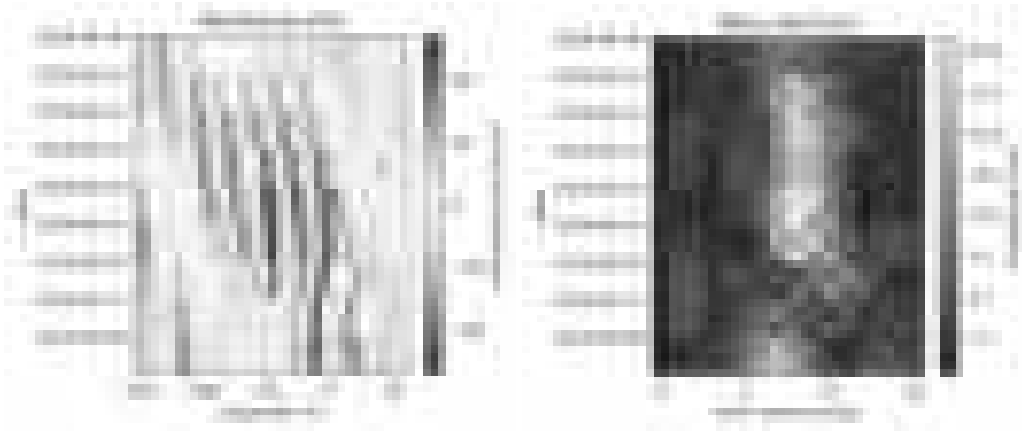

(a) Meridional wind (b) Wave spectrum

Figure 6.10: Hovmöller diagram of meridional wind at 250 hPa (a) and the corresponding amplitude spectrum (b) for the heatwave in late June 2019. The contour lines in (a) mark the region in time and longitude where the temperature anomaly at 850 hPa is above +6 K. The hashed ('x') areas in (b) show the phase velocities below 5°lon/day. All shown values in the diagrams are a latitudinal average over 45°N–55°N.

Again, the strong intensification of Rossby waves can also be clearly seen when looking at the 45–55°N average meridional wind in Figure 6.10 and at the wave spectrum, respectively. Here, the onset of the heatwave and the wave breaking coincides with highly amplified waves at wavenumber 7–9. The heatwave itself is then sustained by a period of very slow phase speeds of the most relevant waves. Even though there was already a period of relatively strong wave activity the days before the wave breaking, i.e., from the 21st on, the heatwave only started with the wave breaking and the following days of slow phase speed.

6.3.3 Early August heatwave 2003

Another noteworthy heatwave occurred in early August 2003. It was mainly characterized by an amplified ridge above France that became stationary for many days. For brevity and because it doesn't bring new insights here, we skip the plots for the individual days.

A look at the Hovmöller plot (Figure 6.11) shows waves that are hardly moving, only the envelope is moving, i.e. the group velocity is larger zero and moving eastwards while the phase velocity is nearly zero and the ridges and troughs stay in place. This slow phase speed nearly all of the time at all relevant wavelengths is clearly visible in the wave spectrum where the hatched area fills nearly all of the area.

Compared to the earlier two examples of heatwaves, the amplitudes in the wave spectrum are much lower, and, in the beginning, there is a superposition of waves of many different wavelengths, which then, later on, concentrate more and more towards wavenumber 6 and 7 while the amplitude increases. But in this case, we can observe very low phase velocities at all relevant wavelengths, which lead to a quasi-stationary high-pressure system over Europe early on. So, on this occasion, it

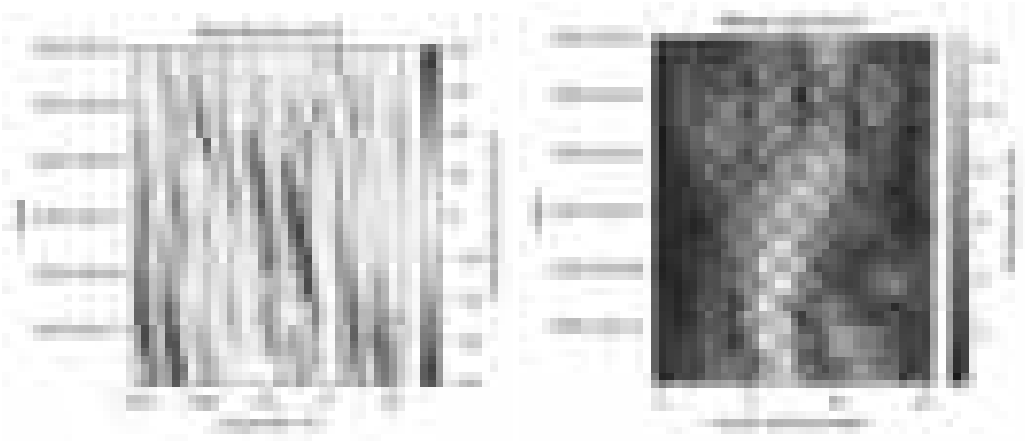

(a) Meridional wind (b) Wave spectrum

Figure 6.11: Hovmöller diagram of meridional wind at 250 hPa (a) and the corresponding amplitude spectrum (b) for the heatwave in early August. The contour lines in (a) mark the region in time and longitude where the temperature anomaly at 850 hPa is above +6 K. The hashed ('x') areas in (b) show where the phase velocities are below 5°lon/day. All shown values in the diagrams are a latitudinal average over 40°N–55°N.

looks like the heatwave was helped to develop not by the amplitude of the Rossby waves but rather by the small phase velocity over an extended period.

6.3.4 Summary of the events

We can conclude that, at least for the examples considered here, there seems to be a relationship between heatwaves and highly amplified Rossby wave activity around the wavenumbers 6–9 together with slow phase velocities. In one example we have also seen that an extended period of slow phase velocity with about average wave activity can also be connected to a massive heatwave.

Comparing this to the previous section with the aggregated results for blockings in summer, we should take into account that the heatwaves we looked at (except for the late phase of the July 2019 heatwave) were located at considerably lower latitudes (around 40-60°N) compared to where most of the blockings in this season occur (around 55-70°N) (compare Figure 6.3 (c)).

For the amplitude spectrum, there we also find some differences. Even though in the seasonal statistics we could also observe an increase of wave activity in the blocked region, there it was mostly at lower wavenumbers, i.e. ≤ 7, while in the three events, we observed an increase mostly in the range 6–9, where especially the heatwave in late June 2019 with the highest wave activity at wavenumber 8 stands out (while the other events were mostly in the 6–7 range). But that event, in particular, was at comparatively low latitudes (and also more an amplified, stationary ridge than a blocking). And in general, as we already learned from looking at the climatology of the wave spectrum (see Figure 4.5), the wavenumbers increase towards higher latitudes. In summer, the tilt corresponds to a shift of about 1.5–2 wavenumbers per 10°latitude, and taking this into account it matches quite well with the aggregated statistics for blockings shown in Figure 6.3 (c). Also, the reduction in phase speed agrees with the findings in the previous section.

6.4 Conclusion

First, we conclude that there is a clear relationship between extreme temperature events and the atmospheric state at synoptic scales. Specifically, blocking events can be linked to temperature anomalies relative to the blocking position in certain areas. Persistent blockings or successive blockings can result in significant temperature extremes. In winter, these events are associated with cold spells primarily occurring southeast of the blocking region, whereas in summer, heatwaves typically develop directly beneath the blocking area. This is in agreement with what was found by Kautz et al. (2022).

These blocking events exhibit a distinct signature in the Rossby wave spectrum. Wave amplitudes are amplified north of and within parts of the blocked region, coupled with reduced wave activity to the south. In summer and autumn, the pattern also exhibits an eventual increase in wave activity much further south. The phase speed of Rossby waves is significantly reduced in the latitudes affected by blockings, while it increases to the north of the blocking region.

The historical events that were investigated have highlighted a slightly different appearance in the wave spectrum. The amplification of wave activity in these cases is primarily observed at higher wavenumbers, specifically in the range of 6-9, compared to the seasonal statistics. But it has to be noted that the cases studied here were associated with blockings or stationary ridges over central Europe which is at lower latitudes compared to the most blocked latitudes in the seasonal statistics. Taking this into account, the wave activity is shifted towards higher wavenumbers, and this backs up the signature we observed earlier when using the aggregated statistics. Thus, a change in the wave spectrum towards amplified Rossby waves, along with reduced phase velocity, is a strong indicator of an increased likelihood of blocking situations.

Overall, the study demonstrates that there is a complex interplay between Rossby waves, blocking events, and extreme temperature events. Recognizing the specific signatures in the Rossby wave spectrum can enhance our ability to predict and understand these extreme weather phenomena.

7 Conclusions

In this study, we tried to answer three specific research questions focusing on Rossby wave activity in the context of climate change and its relationship to extreme temperature events in Europe.

Chapter 4 addressed the question, "What are the characteristics in the Rossby wave spectrum that are important for the climate in Europe, and what are their trends in reanalysis data?"

It investigated Rossby wave activity and its trends over time, mainly focusing on the benefits of partitioning the hemisphere into smaller sectors to specifically study waves relevant to European weather. This method enhanced the signal, allowing for a more precise analysis of Rossby waves. Our findings also indicate that zonal wavenumber analysis, when combined with high-pass filtering, effectively captures the most important characteristics of Rossby waves: the amplitude and phase speed of the transient part of the Rossby waves at intermediate wavenumbers, i.e., around 4–8, in the mid-latitudes.
The analysis of reanalysis data from 1940 to 2019 revealed an increasing trend in Rossby wave activity across all seasons, with the most significant increases observed in winter and spring. For spring, there is also a notable shift towards higher latitudes. This is likely linked to an increase in blocking events and, for spring, a corresponding northward shift in blocking activity.

Chapter 5 investigated the question, "To what extent do current climate models capture essential Rossby wave characteristics, and what are their projected trends?"

It was shown that the performance of the AWI-CM model in simulating wave activity was satisfactory. In contrast, the ICON timeslice experiments showed substantial deviations from reanalysis data, limiting their reliability.
Projections using AWI-CM under the SSP585 scenario suggest a shift of Rossby wave activity towards higher latitudes and smaller wavenumbers, with a notable decrease in wave activity during summer. Under the SSP370 scenario, a similar latitudinal shift was observed, along with a general reduction in wave activity except during spring, where only a shift was noted. The trend in phase speed was less significant, but suggested an increase in phase speed near the maximum wave activity, except for spring. These trends imply a shift in blockings towards higher latitudes and, except for spring, a decrease in blocking frequency due to the increased phase speed.

Chapter 6 answered the question, "How do atmospheric blockings influence temperature extremes, and what is their relationship with Rossby wave activity?"

We learned that there is a strong relationship between temperature extremes and the atmospheric state, and we could, specifically for blockings, show how this impacts the spatial patterns of

temperature anomaly relative to the blockings.
Past heatwaves and aggregated blocking statistics, studied with ERA5 reanalysis data, exhibited a distinct signature in the Rossby wave spectrum: enhanced wave activity at dominant wavenumbers for the blocked latitude, coupled with reduced phase speed. This characteristic highlights the relationship between enhanced Rossby wave activity (with slow phase speeds) and blocking events. This signature helps to identify blockings in wave spectra and aids in interpreting blocking likelihood. These findings support the observed trends in reanalysis data, namely an increase and shift in blockings, and the projections indicating a shift to higher latitudes with a reduced likelihood of blocking events under the SSP585 scenario due to increased phase speed.

Looking at other publications, our findings based on reanalysis data are partly in agreement, e.g., the poleward shift is compatible with the shift in the jet stream found in Woollings et al. (2023). On the other hand, Shaw and Miyawaki (2024) described a strengthening in the jet stream that contrasts with our findings of an increasing trend in wave activity. But it is in agreement with the signs of increasing phase speed that we also found.

Our findings with the climate models, specifically the reduction in blockings, agree with other studies, e.g., Davini and D'Andrea (2020) and Woollings et al. (2018). However, the review by Woollings et al. (2018) reported a shift towards higher latitudes only during summer, while we found it for all seasons. Nevertheless, the strong relationship between blockings and wave activity in our analysis mirrors what was described, e.g., by Riboldi et al. (2020) and Fragkoulidis and Wirth (2020).

All in all, our research contributes to a deeper understanding of Rossby wave dynamics and their seasonal and latitudinal trends. By improving the methodologies for analyzing these waves, we provide tools to enhance the interpretation of climate models. The identified trends and shifts in wave activity have significant implications for understanding future climate scenarios and their potential impacts on weather patterns and extreme events.

This study's strength lies in its comprehensive analysis of Rossby wave activity using reanalysis data and model projections. However, limitations include potential biases in the AWI-CM and the limitations of the ICON timeslice experiments. These factors should be considered when interpreting the results. Besides, many methods used were comparable simple approaches that can be refined and improved.

But there is also a lot of room for future studies that can build up on the results of this thesis and further enhance the understanding of the atmosphere's dynamic:

- Examine the general state of the atmosphere during years with numerous blockings compared to years with few blockings. That could possibly also be linked to different kinds of multi-annual oscillations.

- Study specifically the onset phase of blockings to better understand what boundary conditions concerning Rossby wave activity are relevant for blockings to develop. For that, e.g., time-lag

correlations between enhanced wave amplitudes and temperature extremes/blockings could be used.

- Investigate variations in the wave spectrum between different types of blocks and different blocking latitudes. This could also be complemented by conducting more case studies that could be grouped by blocking type and location. This could be further extended to case studies of cold spells in winter.

- Execute sensitivity analyses regarding different warming scenarios, i.e., the differences in the trends when using different warming scenarios in the climate models.

- Study where the discrepancies in the ICON timeslice model simulations originate from and how other climate models perform.

In conclusion, this thesis has provided significant insights into the trends and characteristics of Rossby wave activity and their implications for future climate scenarios. The methodologies developed, and the findings obtained have the potential to advance both academic research and practical applications in meteorology and climate science. Further research, as recommended, will continue to build on these findings, contributing to our evolving understanding of atmospheric dynamics.

8 Supporting material

8.1 Detrending of the 850 hPa temperature anomaly and the 500 hPa geopotential height anomaly in ERA5 data

The Figure 8.1 shows the detrending of the temperature anomaly at 850 hPa (T850) along the lines of the anomaly calculation and detrending method described in Section 3.2.1 where it was only shown for the 2 m temperature (Figure 3.2).

(a) Seasonal anomaly (annual means) and fit to the data

(b) Trend of annual mean anomaly and fit to the data

(c) Distribution of daily raw data (offset removed), anomaly, and detrended anomaly

(d) Mean detrended anomaly data by day of year (and season in color).

Figure 8.1: Same as Figure 3.2, but for the temperature at 850 hPa (T850) instead of the 2 m temperature (T2m).

Similarly, Figure 8.2 shows the detrending of the geopotential height anomaly at 500 hPa (Z500) applying precisely the same method of detrending as before, but to a different variable.

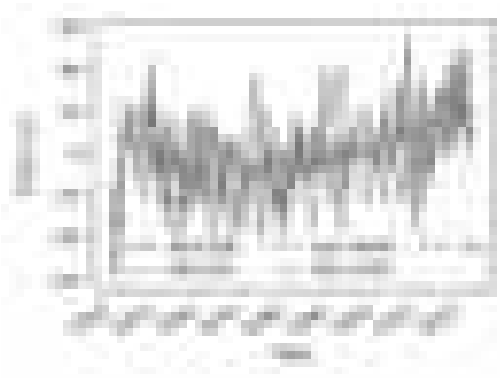

(a) Seasonal anomaly (annual means) and fit to the data

(b) Trend of annual mean anomaly and fit to the data

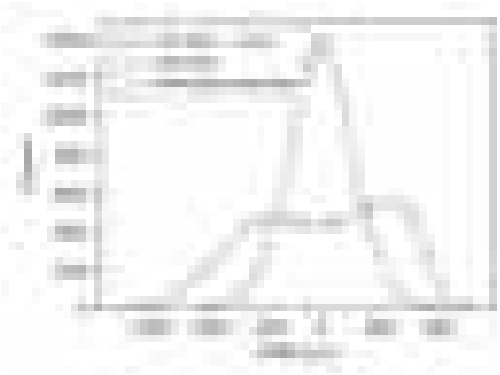

(c) Distribution of daily raw data (offset removed), anomaly, and detrended anomaly

(d) Mean detrended anomaly data by day of year (and season in color).

Figure 8.2: Same as Figure 3.2, but for the geopotential height at 500 hPa (Z500) instead of the 2 m temperature (T2m).

8.2 Blockings and zonal wavenumber parameter: anomaly-based method for blocking detection

In this section, we will show the same plots as in Section 6.2, i.e., the signatures of blockings in the wave spectra, except here we will apply the anomaly-based method for blocking detection as described in Chapter 3, instead of the absolute method.

Figure 8.3 shows the differences in amplitude of the Rossby waves between blocked days and all days of the specific season; it is analog to Figure 6.4, but here with the anomaly-based method for blocking identification.

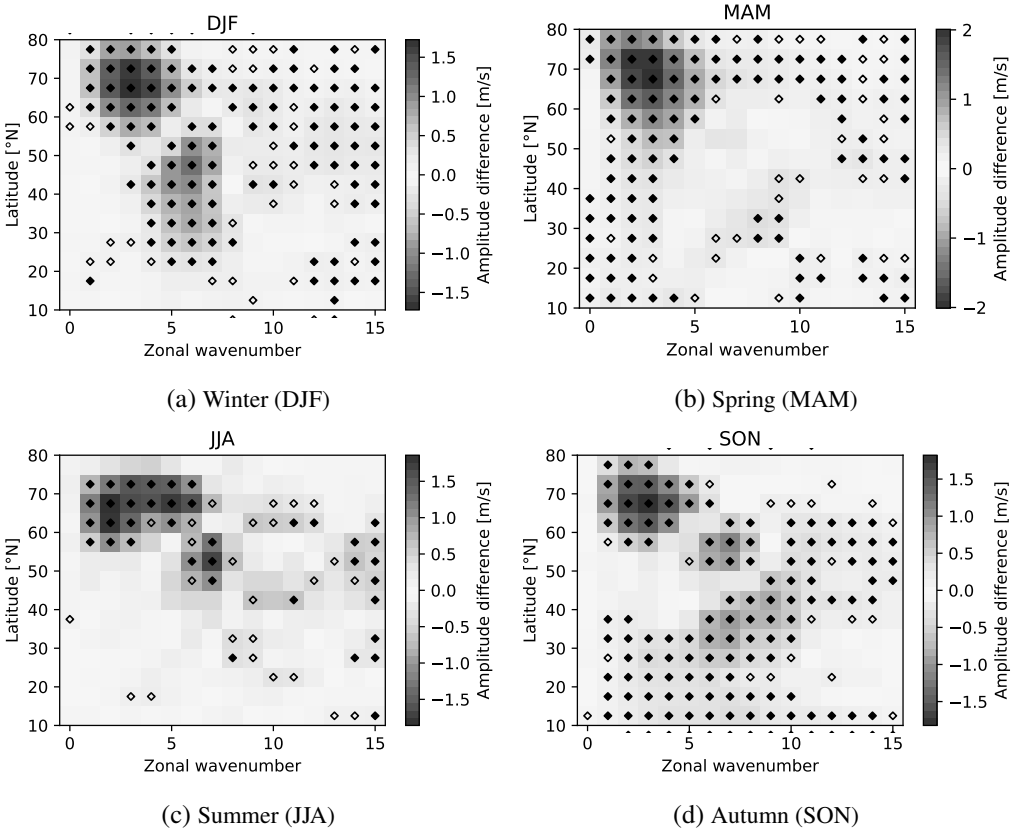

(a) Winter (DJF)

(b) Spring (MAM)

(c) Summer (JJA)

(d) Autumn (SON)

Figure 8.3: Same as Figure 6.4, but here using the anomaly-based method for blocking detection.

Figure 8.4 similarly shows the differences in phase velocity between blocked days and all days of the specific season for different wavenumbers and latitudes; again, analog to Figure 6.5, but using the anomaly-based method for blocking identification instead of the absolute method.

Last but not least, we will look at the differences in the number of days with slow-moving waves, i.e., transient waves where the magnitude of the phase velocity is below 2°lon/day. The differences in Figure 8.5 are, again, calculated by subtracting the seasonal average of the fraction of days with slow-moving waves from the fraction of days calculated only for days with an identified blocking, except here we are using the anomaly-based method, contrary to Figure 6.6 for the absolute method.

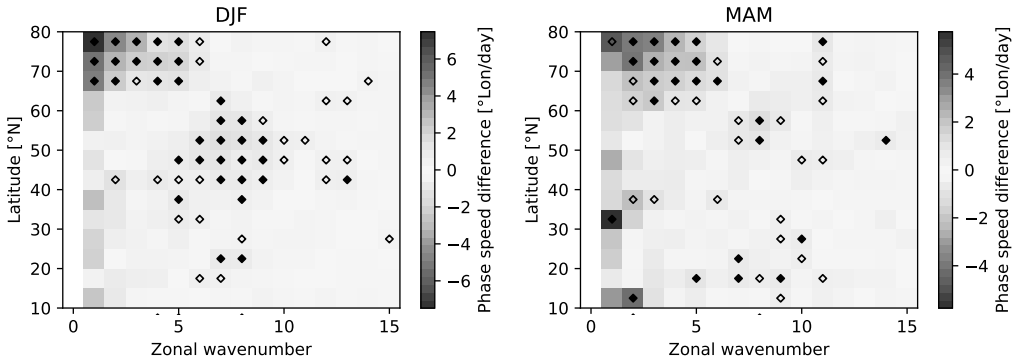

(a) Winter (DJF)

(b) Spring (MAM)

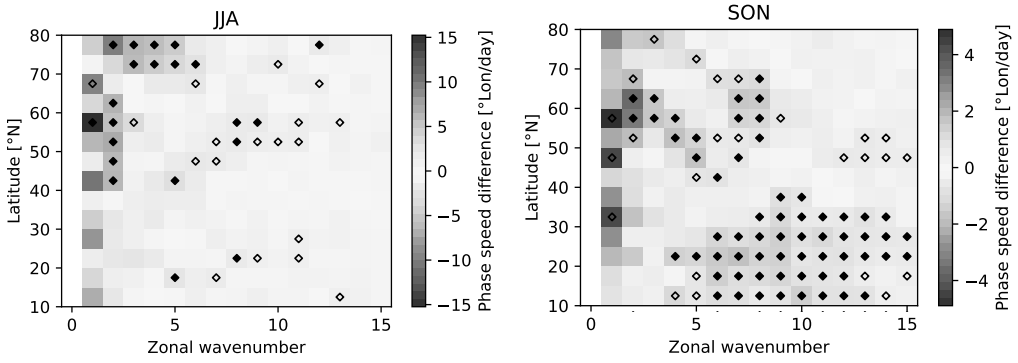

(c) Summer (JJA)

(d) Autumn (SON)

Figure 8.4: Same as Figure 6.5, but here using the anomaly-based method instead of the absolute method.

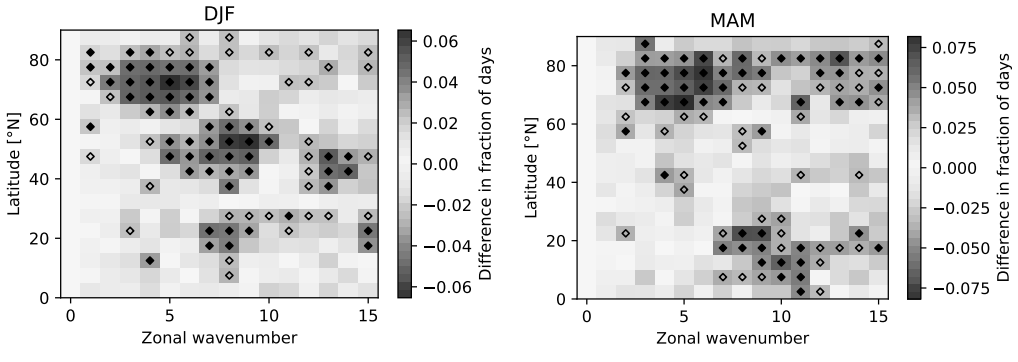

(a) Winter (DJF)

(b) Spring (MAM)

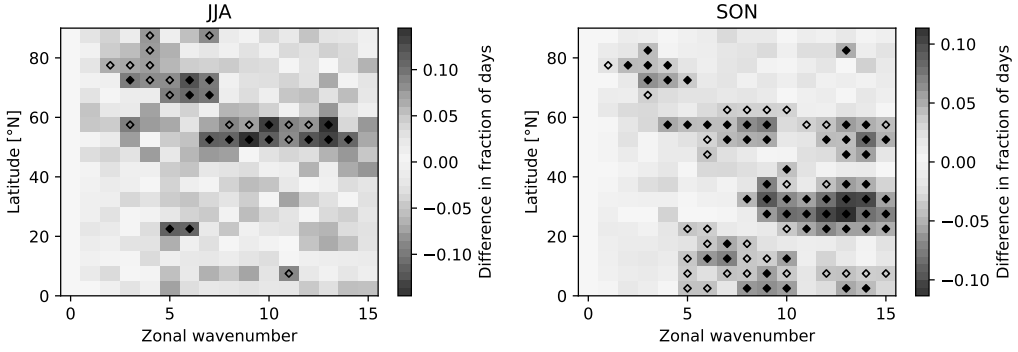

(c) Summer (JJA)

(d) Autumn (SON)

Figure 8.5: Same as Figure 6.6, but using the anomaly-based method instead of the absolute method here.

8.3 Detailed plots for the linear regression and trends in reanalysis data for the NAE sector

This section shows the details in the time evolution for the wavenumbers and latitudes where the strongest increasing or decreasing trends were observed in Section 4.2.2. Alongside, all the linear trends for the same wavenumber and latitudes are shown when varying the start and end date used for the linear regression. From this plot, it can be estimated how robust the trend is or whether multi-annual or multi-decadal oscillations dominate it. These oscillations would appear as patches of alternating signs (or very different magnitudes). Diagonally, towards the bottom right corner of the plot, the time extension of the period used for the regression increases. The minimal time extend shown in these plots is 30 years.

All the plots shown here, i.e., Figure 8.6 for zonal wavenumber 5 and 6 at 40—55°N for winter, Figure 8.7 for zonal wavenumber 5 and 6 at 50—55°N for spring, Figure 8.8 for zonal wavenumber 9 at 40—45°N for summer, and Figure 8.9 for zonal wavenumber 6 and 7 at 45—60°N for autumn, are discussed in Section 4.2.2.

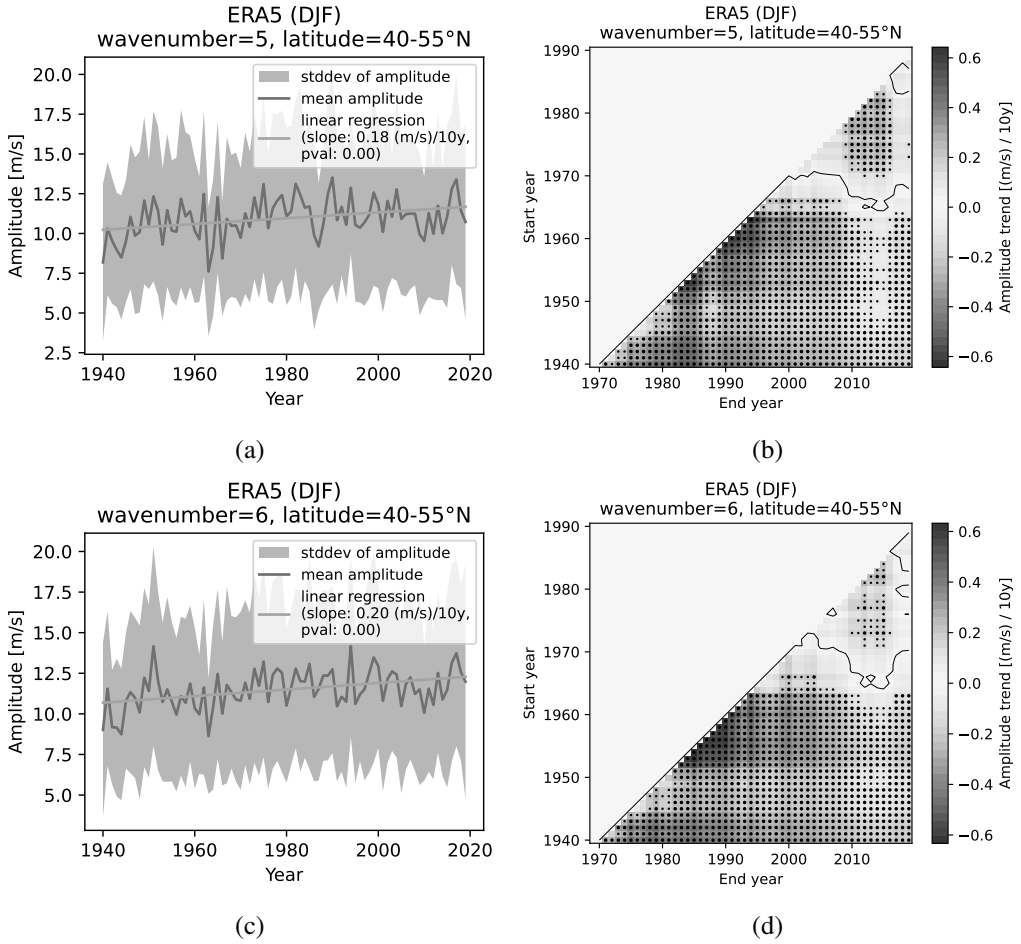

Figure 8.6: Linear trend of the amplitudes of zonal wavenumber decomposition of the meridional wind at 250 hPa (the transient part with a 21-day highpass filter) for winter (DJF) and zonal wavenumber 5 (top row) and 6 (bottom row) at 40–55°N. The plots in the left column show the time evolution of the yearly mean amplitude, its standard deviation, and the linear regression fit line. The plots in the right column show the linear regression slope for all combinations of selected start and end years with at least a 30-year extent. Results that are significant at the 95 % (99 %) confidence level are marked with a small (large) dot.

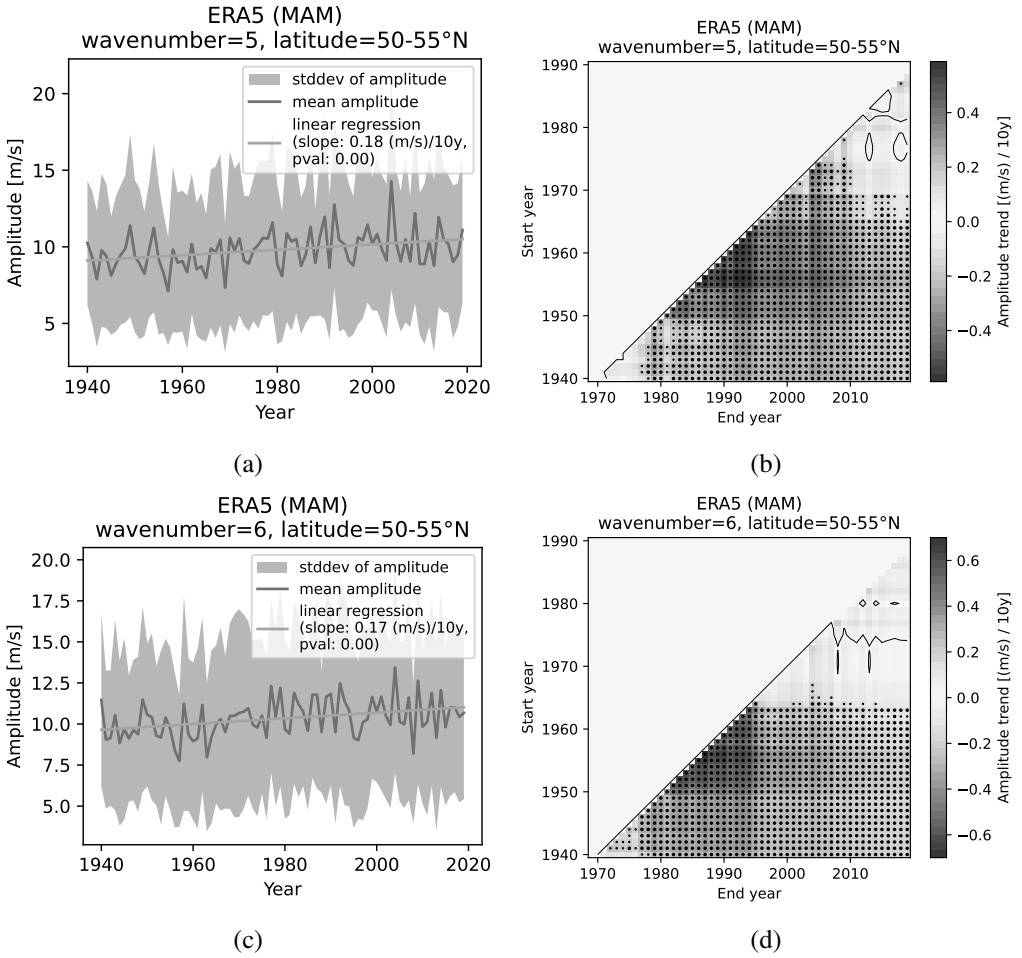

Figure 8.7: Linear trend of the amplitudes of zonal wavenumber decomposition of the meridional wind at 250 hPa (the transient part with a 21-day highpass filter) for spring (MAM) and zonal wavenumber 5 (top row) and 6 (bottom row) at 50–55°N. The plot in the left column shows the time evolution of the yearly mean amplitude, its standard deviation, and the linear regression fit line. The plot in the right column shows the linear regression slope for all combinations of selected start and end years with at least a 30-year extent. Results that are significant at the 95 % (99 %) confidence level are marked with a small (large) dot.

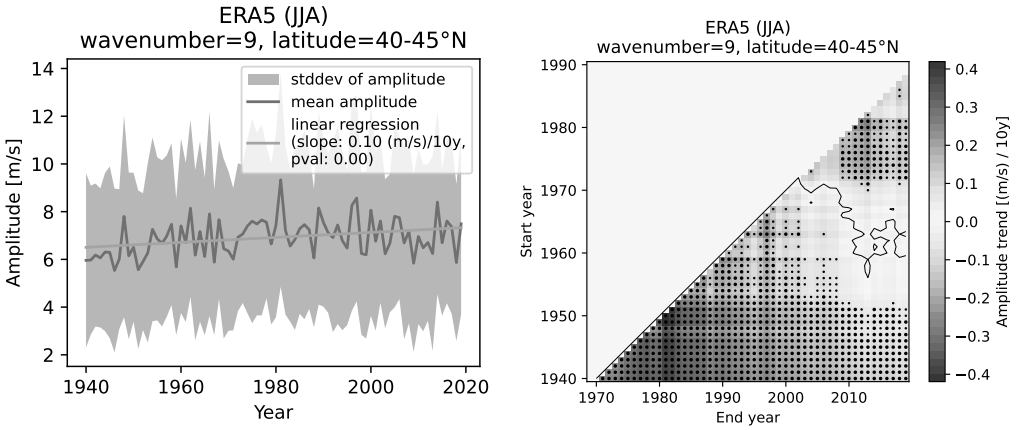

(a) (b)

Figure 8.8: Linear trend of the amplitudes of zonal wavenumber decomposition of the meridional wind at 250 hPa (the transient part with a 21-day highpass filter) for summer (JJA) and zonal wavenumber 9 at 40–45°N. The plots in the left column show the time evolution of the yearly mean amplitude, its standard deviation, and the linear regression fit line. The plots in the right column show the linear regression slope for all combinations of selected start and end years with at least a 30-year extent. Results that are significant at the 95 % (99 %) confidence level are marked with a small (large) dot.

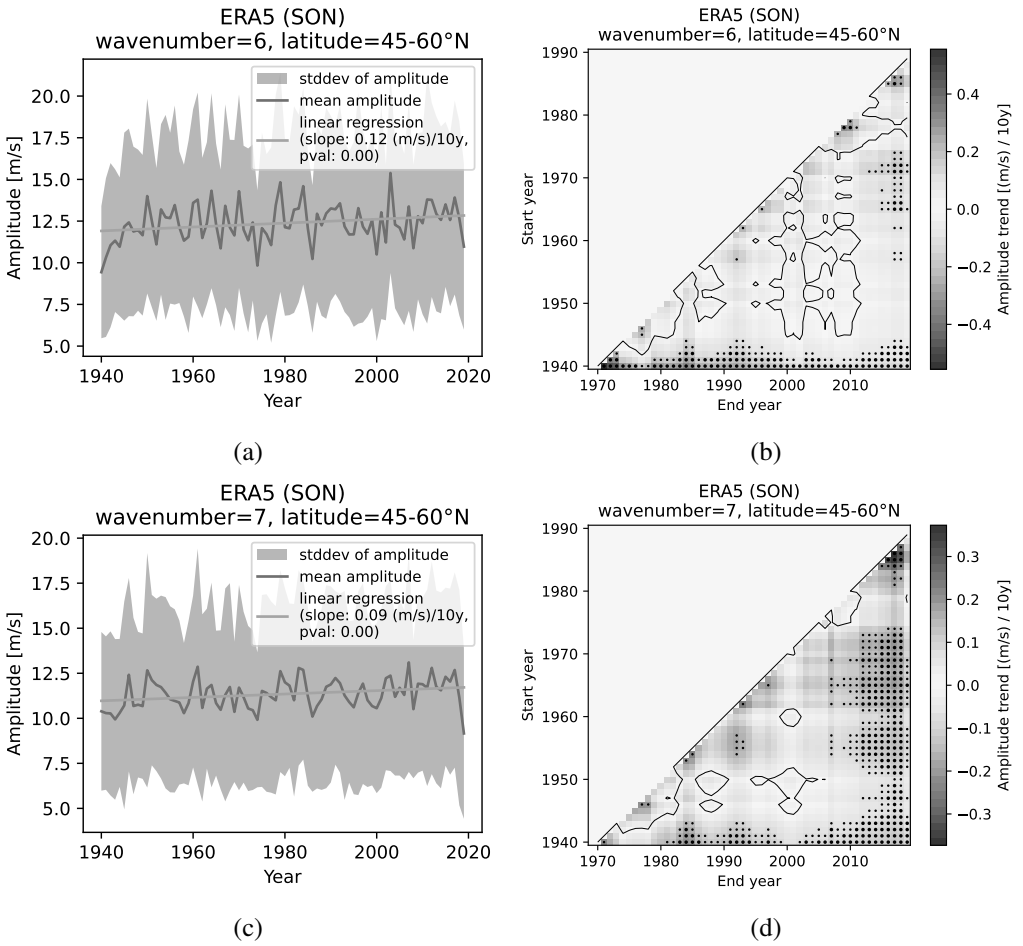

Figure 8.9: Linear trend of the amplitudes of zonal wavenumber decomposition of the meridional wind at 250 hPa (transient part with a 21-day highpass filter) for autumn (SON) and zonal wavenumber 6 (top row) and 7 (bottom row) at 45–60°N. The plot in the left column shows the time evolution of the yearly mean amplitude, its standard deviation, and the linear regression fit line. The plot in the right column shows the linear regression slope for all combinations of selected start and end years with at least a 30-year extent. Results that are significant at the 95 % (99 %) confidence level are marked with a small (large) dot.

8.4 ERA5 vs. climate models: standard deviations

This plot shows the comparison of the standard deviation of the transient part of the Rossby wave activity in AWI-CM with SSP370 scenario (mean over the years 2020–2030) and ICON timeslice experiments (for the baseyear 2000) to the ERA5 reanalysis data (mean over the years 2000-2020), as explained in Section 5.1.

Figure 8.10 shows the standard deviations while Figure 8.11 shows the differences of the corresponding model to the reanalysis data. The results are discussed in Section 5.1.

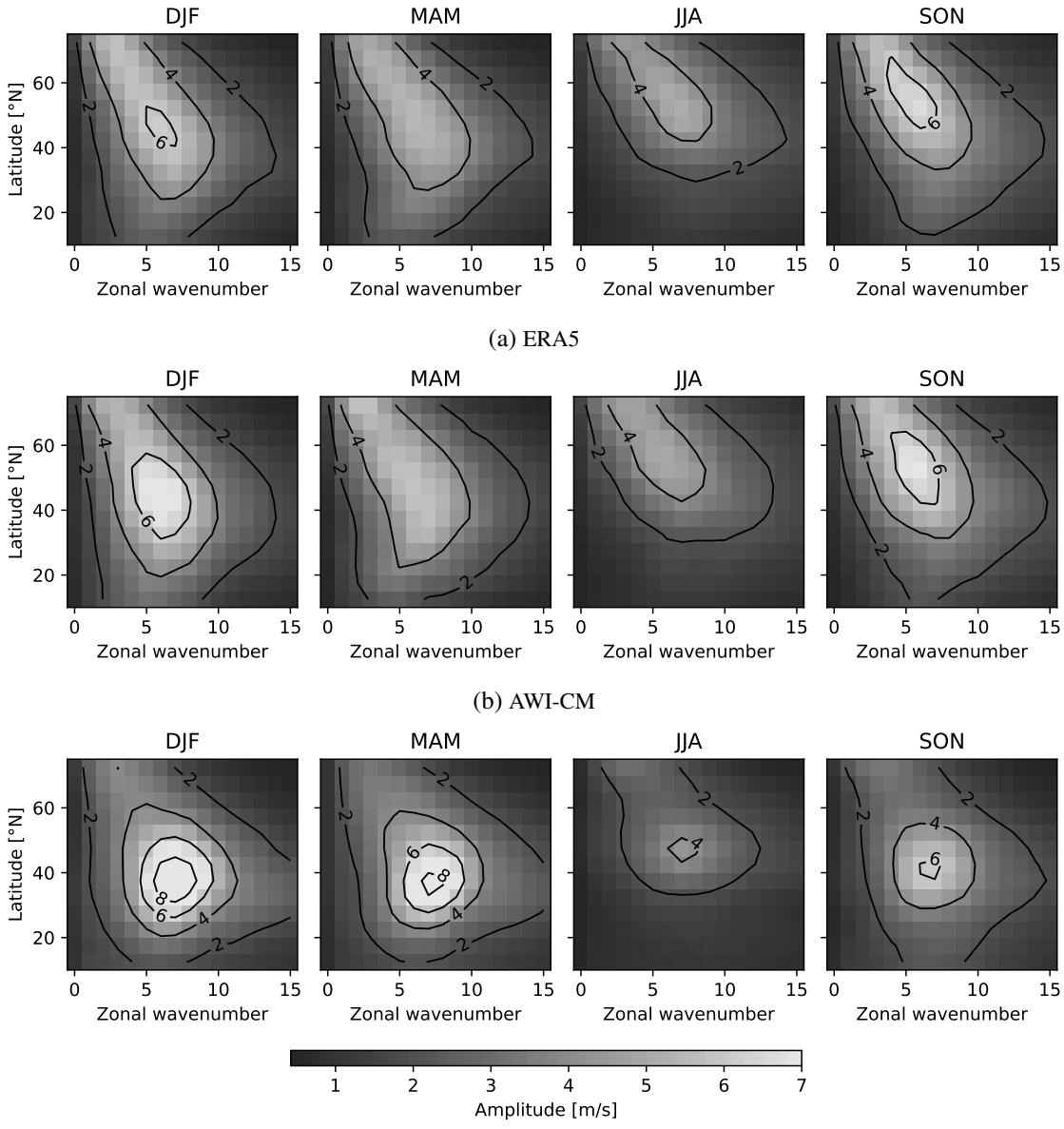

(a) ERA5

(b) AWI-CM

(c) ICON timeslice

Figure 8.10: Standard deviation of amplitudes of zonal wavenumber decomposition of the transient part with a 21-day highpass filter of the meridional wind at 250 hPa. Subplot (a) shows the result for the ERA5 data averaged from 2000 to 2020, subplot (b) for AWI-CM with SSP370 scenario averaged from 2020 to 2030, and (c) for ICON timeslice for baseyear 2000.

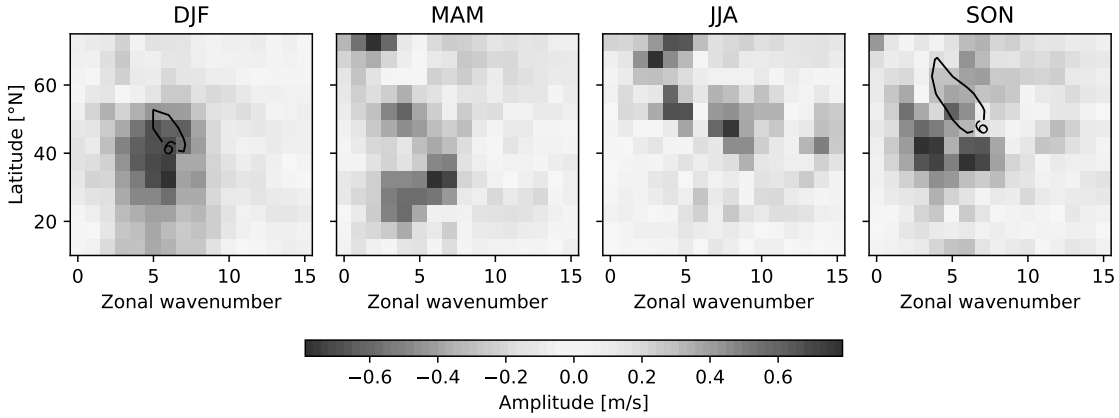

(a) AWI-CM – ERA5

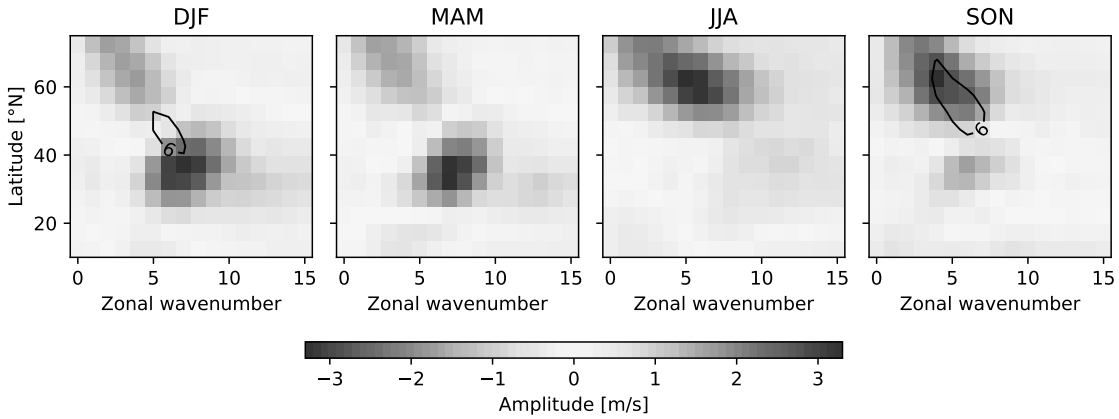

(b) ICON timeslice – ERA5

Figure 8.11: Difference in the standard deviation of amplitudes of zonal wavenumber decomposition of the transient part with a 21-day highpass filter of the meridional wind at 250 hPa. Subplot (a) shows the delta of AWI-CM (2020–2030) and (b) of ICON timeslice (2000), both with respect to ERA5 (2000-2020).

8.5 ICON timeslice: linear trend from 2000 to 2040

Figure 8.12 shows the linear trends of the amplitudes for the transient Rossby waves using the ICON timeslice experiments. In this case, we calculated the trend only using the baseyears 2000 and 2040, instead of over all three baseyears, i.e., 2000, 2040, and 2090 which was shown in Section 5.1 in Figure 5.7. So, this plot shows the changes in between about the first half of the entire period only. In comparison with Figure 5.7, which showed the trend for the entire period, we can see that the magnitudes of the trends between the first two baseyears are much higher than over the whole time. This implies that most of the changes happened between 2000 and 2040. The changes are much weaker after that, i.e., between 2040 and 2090. This is only briefly discussed in Section 5.1 because the performance of the ICON timeslice experiments in reproducing the essential characteristics was insufficient anyway.

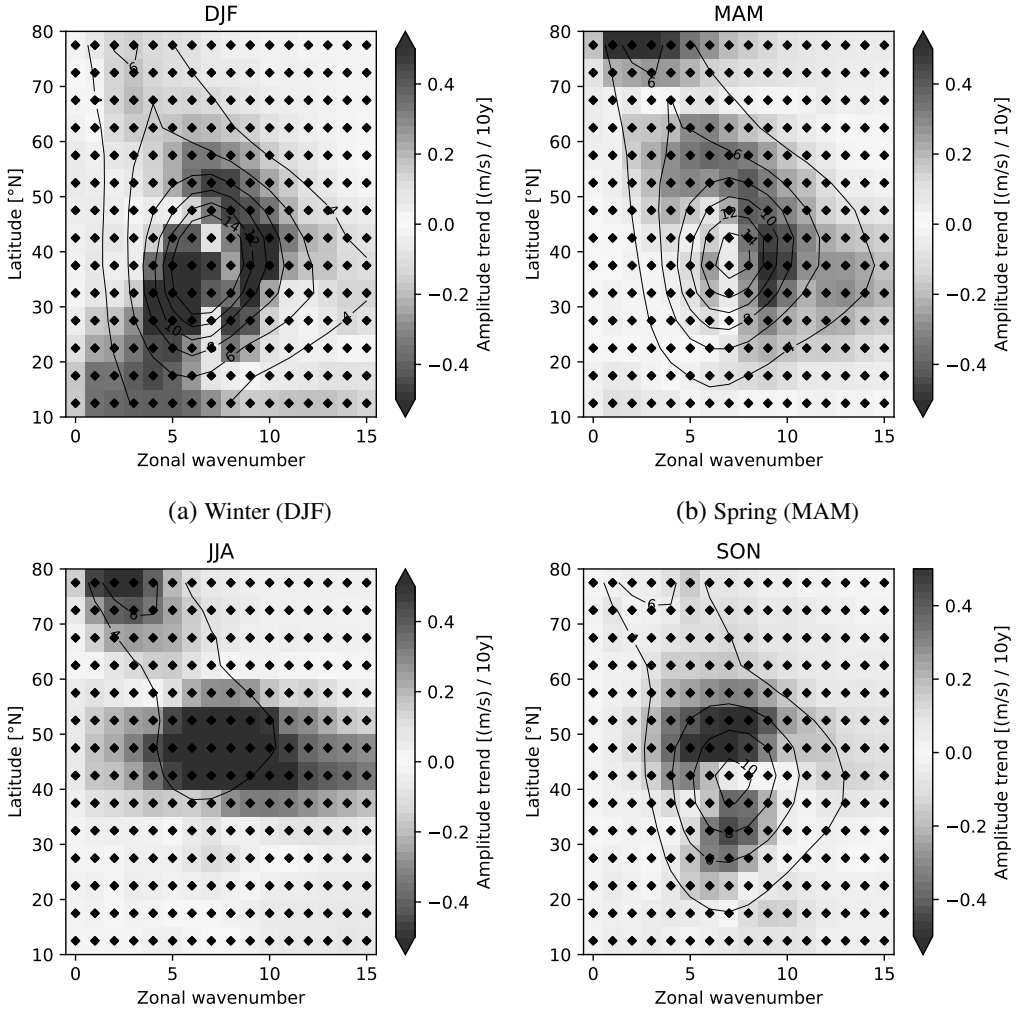

(a) Winter (DJF)

(b) Spring (MAM)

(c) Summer (JJA)

(d) Autumn (SON)

Figure 8.12: Same as in Figure 5.7 but fitted only for the baseyears 2000 and 2040 (instead of 2000, 2040 and 2090).

Abbreviations

AWI	Alfred-Wegener-Institut Helmholtz-Zentrum für Polar- und Meereisforschung
AWI-CM	AWI Climate Model: It consists of the atmospheric model ECHAM6, developed at the Max Planck Institute for Meteorology in Hamburg, and the Finite Element Sea ice-Ocean Model (FESOM), version 1.4. FESOM and ECHAM6 are coupled every via the OASIS3-MCT coupler.
C3S	Copernicus Climate Change Service
CMIP6	Coupled Model Intercomparison Project 6
DKRZ	Deutsche Klimarechenzentrum
ECHAM	ECMWF model branched by Hamburg: an atmospheric general circulation model
ECHAM6	ECHAM in its sixth generation: atmospheric component of the MPI-M Earth System Model
ECMWF	European Centre for Medium-Range Weather Forecasts
ERA5	ECMWF Reanalysis v5: ERA5 is the fifth generation ECMWF atmospheric reanalysis of the global climate covering the period from January 1940 to the present.
FESOM14	Finite Element Sea Ice-Ocean Model (FESOM) v.1.4
GHG	greenhouse gas
ICON	ICOsahedral Nonhydrostatic
ITCZ	Inter-Tropical Convergence Zone
NAE	North Atlantic and European sector: this is used to name the sector extending from about 90°W–60°E on the northern hemisphere
OASIS3-MCT	OASIS coupler interfaced with the Model Coupling Toolkit: OASIS was in its initial version the abbreviation for "Ocean Atmosphere Sea Ice Soil", but it has now advanced beyond these capabilities.

RCP8.5 Representative Concentration Pathway with an additional forcing of 8.5 W/m² in the year 2100

SIC Sea-ice concentration

SSP370 Shared Socioeconomic Pathway 3 with an additional forcing of 7 W/m² in the year 2100: This scenario is in the upper-middle part of the full range of scenarios. It was newly introduced after the RCP scenarios, closing the gap between RCP6.0 and RCP8.5.

SSP585 Shared Socioeconomic Pathway 5 with an additional forcing of 8.5 W/m² in the year 2100: This scenario represents the upper boundary of the range of scenarios described in the literature. It can be understood as an update of the CMIP5 scenario RCP8.5, now combined with socioeconomic reasons.

SST Sea Surface Temperature

Bibliography

Barnes, E. A., and J. A. Screen, 2015: The impact of arctic warming on the midlatitude jet-stream: Can it? has it? will it? *WIREs Climate Change*, **6 (3)**, 277–286, https://doi.org/10.1002/wcc.337.

Braun, M., 2021: Ozone hole impacts on surface temperatures under climate change. Dissertation, Karlsruher Institut für Technologie (KIT), Landau in der Pfalz.

Butler, A. H., D. W. J. Thompson, and R. Heikes, 2010: The steady-state atmospheric circulation response to climate change–like thermal forcings in a simple general circulation model. *Journal of Climate*, **23 (13)**, 3474–3496, https://doi.org/10.1175/2010JCLI3228.1.

C3S, 2024: Era5: data documentation. Accessed: 2024-04-22, https://confluence.ecmwf.int/display/CKB/ERA5%3A+data+documentation.

Craig, A., S. Valcke, and L. Coquart, 2017: Development and performance of a new version of the oasis coupler, oasis3-mct_3.0. *Geoscientific Model Development*, **10 (9)**, 3297–3308, https://doi.org/10.5194/gmd-10-3297-2017.

Crueger, T., and Coauthors, 2018: Icon-a, the atmosphere component of the icon earth system model: Ii. model evaluation. *Journal of Advances in Modeling Earth Systems*, **10 (7)**, 1638–1662, https://doi.org/10.1029/2017MS001233.

Davini, P., and F. D'Andrea, 2020: From cmip3 to cmip6: Northern hemisphere atmospheric blocking simulation in present and future climate. *Journal of Climate*, **33 (23)**, 10 021–10 038, https://doi.org/10.1175/JCLI-D-19-0862.1.

Dorrington, J., K. Strommen, F. Fabiano, and F. Molteni, 2022: Cmip6 models trend toward less persistent european blocking regimes in a warming climate. *Geophysical Research Letters*, **49 (24)**, https://doi.org/10.1029/2022GL100811, URL https://onlinelibrary.wiley.com/doi/10.1029/2022GL100811.

DWD, 2024: ICON. Accessed: 2024-04-22, https://www.icon-model.org/.

Etling, D., 2008: *Theoretische Meteorologie*. Springer Berlin Heidelberg, Berlin, Heidelberg, https://doi.org/10.1007/978-3-540-75979-9, URL http://link.springer.com/10.1007/978-3-540-75979-9.

FESOM team, 2020: The awi climate model (AWI-CM). Accessed: 2024-04-21, https://fesom.de/models/awi-cm/.

Forzieri, G., A. Cescatti, F. B. E Silva, and L. Feyen, 2017: Increasing risk over time of weather-related hazards to the european population: a data-driven prognostic study. *The Lancet Planetary Health*, **1 (5)**, e200–e208, https://doi.org/10.1016/S2542-5196(17)30082-7.

Fragkoulidis, G., and V. Wirth, 2020: Local rossby wave packet amplitude, phase speed, and group velocity: Seasonal variability and their role in temperature extremes. *Journal of Climate*, **33 (20)**, 8767–8787, https://doi.org/10.1175/JCLI-D-19-0377.1.

Fragkoulidis, G., V. Wirth, P. Bossmann, and A. H. Fink, 2018: Linking northern hemisphere temperature extremes to rossby wave packets. *Quarterly Journal of the Royal Meteorological Society*, **144 (711)**, 553–566, https://doi.org/10.1002/qj.3228.

Hersbach, H., and Coauthors, 2020: The era5 global reanalysis. *Quarterly Journal of the Royal Meteorological Society*, **146 (730)**, 1999–2049, https://doi.org/10.1002/qj.3803.

Holton, J. R., and G. J. Hakim, 2013: *An introduction to dynamic meteorology*. Fifth edition ed., Academic Press, Amsterdam, URL https://doi.org/10.1016/C2009-0-63394-8.

Horton, D. E., N. C. Johnson, D. Singh, D. L. Swain, B. Rajaratnam, and N. S. Diffenbaugh, 2015: Contribution of changes in atmospheric circulation patterns to extreme temperature trends. *Nature*, **522 (7557)**, 465–469, https://doi.org/10.1038/nature14550.

Kautz, L.-A., O. Martius, S. Pfahl, J. G. Pinto, A. M. Ramos, P. M. Sousa, and T. Woollings, 2022: Atmospheric blocking and weather extremes over the euro-atlantic sector – a review. *Weather and Climate Dynamics*, **3 (1)**, 305–336, https://doi.org/10.5194/wcd-3-305-2022.

Kornhuber, K., D. Coumou, E. Vogel, C. Lesk, J. F. Donges, J. Lehmann, and R. M. Horton, 2020: Amplified rossby waves enhance risk of concurrent heatwaves in major breadbasket regions. *Nature Climate Change*, **10 (1)**, 48–53, https://doi.org/10.1038/s41558-019-0637-z.

Kovats, R. S., and L. E. Kristie, 2006: Heatwaves and public health in europe. *European Journal of Public Health*, **16 (6)**, 592–599, https://doi.org/10.1093/eurpub/ckl049.

Lee, S. H., P. D. Williams, and T. H. A. Frame, 2019: Increased shear in the north atlantic upper-level jet stream over the past four decades. *Nature*, **572 (7771)**, 639–642, https://doi.org/10.1038/s41586-019-1465-z.

Mohleji, S., and R. Pielke, 2014: Reconciliation of trends in global and regional economic losses from weather events: 1980–2008. *Natural Hazards Review*, **15 (4)**, 04014 009, https://doi.org/10.1061/(ASCE)NH.1527-6996.0000141.

NOAA, 2023: Global atmospheric circulations. Accessed: 2024-04-22, https://www.noaa.gov/jetstream/global/global-atmospheric-circulations.

PCMDI, 2023: AMIP sea surface temperature and sea ice: Observational and boundary condition data sets. Accessed: 2024-04-22, https://pcmdi.llnl.gov/mips/amip/.

Prill, F., D. Reinert, D. Rieger, and G. Zängl, 2020: Icon tutorial 2020: Working with the icon model. https://doi.org/10.5676/DWD_PUB/NWV/ICON_TUTORIAL2020, URL https://www.dwd.de/DE/leistungen/nwv_icon_tutorial/pdf_einzelbaende/icon_tutorial2020.pdf?__blob=publicationFile&v=4.

Riboldi, J., F. Lott, F. D'Andrea, and G. Rivière, 2020: On the linkage between rossby wave phase speed, atmospheric blocking, and arctic amplification. *Geophysical Research Letters*, **47 (19)**, https://doi.org/10.1029/2020GL087796, URL https://onlinelibrary.wiley.com/doi/10.1029/2020GL087796.

Semmler, T., and Coauthors, 2020: Simulations for cmip6 with the awi climate model awi-cm-1-1. *Journal of Advances in Modeling Earth Systems*, **12 (9)**, e2019MS002 009, https://doi.org/10.1029/2019MS002009.

Shaw, T. A., and O. Miyawaki, 2024: Fast upper-level jet stream winds get faster under climate change. *Nature Climate Change*, **14 (1)**, 61–67, https://doi.org/10.1038/s41558-023-01884-1.

Shaw, T. A., and Coauthors, 2016: Storm track processes and the opposing influences of climate change. *Nature Geoscience*, **9 (9)**, 656–664, https://doi.org/10.1038/ngeo2783.

Shepherd, T. G., 2014: Atmospheric circulation as a source of uncertainty in climate change projections. *Nature Geoscience*, **7 (10)**, 703–708, https://doi.org/10.1038/ngeo2253.

Sousa, P. M., D. Barriopedro, R. García-Herrera, T. Woollings, and R. M. Trigo, 2021: A new combined detection algorithm for blocking and subtropical ridges. *Journal of Climate*, 1–64, https://doi.org/10.1175/JCLI-D-20-0658.1.

Stevens, B., and Coauthors, 2013: Atmospheric component of the mpi-m earth system model: Echam6. *Journal of Advances in Modeling Earth Systems*, **5 (2)**, 146–172, https://doi.org/10.1002/jame.20015.

Trevisiol, A., L. Gilli, and P. Faggian, 2022: Short and long-term projections of rossby wave packets and blocking events with particular attention to the northern hemisphere. *Global and Planetary Change*, **209**, 103 750, https://doi.org/10.1016/j.gloplacha.2022.103750.

Vallis, G. K., 2017: *Atmospheric and Oceanic Fluid Dynamics: Fundamentals and Large-Scale Circulation*. 2nd ed., Cambridge University Press, Cambridge, https://doi.org/10.1017/9781107588417, URL http://ebooks.cambridge.org/ref/id/CBO9781107588417.

Walther, G.-R., and Coauthors, 2002: Ecological responses to recent climate change. *Nature*, **416 (6879)**, 389–395, https://doi.org/10.1038/416389a.

Wang, Q., S. Danilov, D. Sidorenko, R. Timmermann, C. Wekerle, X. Wang, T. Jung, and J. Schröter, 2014: The finite element sea ice-ocean model (fesom) v.1.4: formulation of an ocean general circulation model. *Geoscientific Model Development*, **7 (2)**, 663–693, https://doi.org/10.5194/gmd-7-663-2014.

Woollings, T., 2022: What is the jet stream? Accessed: 2024-04-22, https://www.climate.gov/news-features/blogs/enso/what-jet-stream.

Woollings, T., M. Drouard, C. H. O'Reilly, D. M. H. Sexton, and C. McSweeney, 2023: Trends in the atmospheric jet streams are emerging in observations and could be linked to tropical warming. *Communications Earth & Environment*, **4 (1)**, 125, https://doi.org/10.1038/s43247-023-00792-8.

Woollings, T., and Coauthors, 2018: Blocking and its response to climate change. *Current Climate Change Reports*, **4 (3)**, 287–300, https://doi.org/10.1007/s40641-018-0108-z.

Acknowledgments

First and foremost, I would like to express my deepest gratitude to Joaquim Pinto, Andreas Fink, and Patrick Ludwig for their willingness to supervise my work and unwavering support throughout this journey. Your guidance has been invaluable.
Also, I thank Peter Braesicke for his insightful comments and feedback, which greatly enhanced this work.
I want to give exceptional thanks to Tatiana for her tireless dedication, hopeful spirit, and belief in my work. Your optimism has been a constant source of encouragement, and the joyful encounters with you and Lena were always refreshing and enriching.
I am also profoundly grateful to Khompat for sharing her scripts and code with me and her dedicated debugging assistance. Without you, parts of this work wouldn't have been possible.
My sincere thanks to my office mates, Juliane, Charlotte, and Tabea, for creating a pleasant and productive working environment.
Thanks also to the whole working group for providing a welcoming, friendly, and ever-supportive atmosphere and for the exciting—and often unconventional joyful—conversations during lunch.

Additionally, Siyu and InYoung, your conversations that extended far beyond meteorology have broadened my horizons, enriched my experience, and always recharged me. Siyu, bouldering with you has always been a great pleasure and source of joy.
Miri, thank you for the stimulating professional exchanges and the enriching moments, both humorous and serious, that we shared.
Janina, thank you for your loyal friendship and helpful and supportive conversations.
Adam and Torsten, your enduring deep friendship and the countless severe and joyful moments we shared gave me a strong sense of belonging.
Claudi, I'm enormously grateful for your always open ear, inexhaustible caring, and constant presence, especially during difficult times. You helped me to face the most challenging times. Gino, your calm, refreshing, and unique nature has often made my problems disappear and put a smile on my face. Hannes, thank you for your straightforward, always positive, supportive attitude and trust. Jenny, your distinctive wake-up routine and cuddle attacks often helped me to escape my thoughts and enjoy the present moment.

Alex, I am particularly grateful for your tremendous patience and leap of faith. You have enriched my life inexpressibly, helping me rediscover and experience its beautiful aspects in a much deeper way than I ever thought possible.

To the Kulturküche team and community, namely Sabine, Yannis, Galina, Vio, Anka, Karl, Janna, Julija, Sven, Maik, Sarah, Andrew, Julie, and many more: Thank you for the love, hugs, and a sense of home. Your meaningful conversations and emotional support have been a cornerstone of my life.

To my flatmates, Kirsten and Loky, thank you for the incredibly diverse conversations and encounters ranging from light-hearted to deeply sorrowful. Your honest, supportive, and caring involvement has meant the world.

I am deeply thankful to my parents, Dagmar and Jürgen, for their unwavering support and unconditional belief in me.
Sabine, thank you for sharing thoughts and memories, exchanging reflections and feedback, and being there through my worries. I'm looking forward to seeing Jaron grow and flourish.
Mario, Nicki, and, last but not least, Vitus, Line, and Aeni, for sharing precious moments and reminding me what matters in life.

Erklärung

Ich versichere wahrheitsgemäß, die Arbeit selbstständig verfasst, alle benutzten Hilfsmittel vollständig und genau angegeben und alles kenntlich gemacht zu haben, was aus Arbeiten anderer unverändert oder mit Abänderungen entnommen wurde sowie die Satzung des KIT zur Sicherung guter wissenschaftlicher Praxis in der jeweils gültigen Fassung beachtet zu haben.

Karlsruhe, den 21.05.2024

(Christian Schröder)